EXPERIMENTAL AND SIMULATION STUDY OF STACK EMISSION AND CONTAMINANT DISPERSION AROUND TYPICAL BUILDING CONFIGURATIONS AND ARRAYS IN HONG KONG

LEE KAI YIP

PhD

The Hong Kong Polytechnic University

2022

The Hong Kong Polytechnic University

Department of Building Environment and Energy Engineering

Experimental and Simulation Study of Stack Emission and Contaminant Dispersion Around Typical Building Configurations and Arrays in Hong Kong

Lee Kai Yip

A thesis submitted in partial fulfilment of the requirements for the degree of Doctor of Philosophy

September 2021

CERTIFICATE OF ORIGINALITY

I hereby declare that this thesis is of my own work and that, to the best of my knowledge and belief, it reproduces no material previously published or written, nor material that has been accepted for the award of any other degree or diploma, except where due acknowledgement has been made in the text.

____________________(Signed)

Lee Kai-yip (Name of student)

ABSTRACT

Abstract of thesis entitled	:	Experimental and simulation study of stack emissions and contaminant dispersion around typical building configurations and arrays in Hong Kong
Submitted by	:	Lee Kai-yip
For the degree of	:	Doctor of Philosophy

at The Hong Kong Polytechnic University, November 2021

Wind velocity and outdoor ventilation play an essential role in diluting air pollutants and improving air quality in urban localities; however, the benefits of sufficient airflow could be significantly offset by the blockage effects from building structures. Ample research has been performed on wind flow around cubical buildings, but little has been conducted on the airflow in the wakes of buildings with configurations and arrays commonly found but considerably unique in Hong Kong.

This thesis assessed the health impacts of exhaust stack emissions on the local community, and investigated the effects of wind direction, building configuration, and array design on airflow patterns and pollutant dispersion in the areas surrounding the point source. To this end, three individual studies were conducted, assessing: (1) The impacts of stack emissions on air quality in a small urban setting, (2) The effects of incident wind angles and building configurations on airflow patterns of building wakes and leeward walls, and (3) The effects of building arrays on airflow and contaminant distributions in the central space of buildings.

Based on the release concentration and the potential hazards to human health, fifteen

chemicals that were possibly emitted from a research building were selected for one year-long air monitoring. A tracer gas study was also performed to identify the dilution factor of the environment, and validate two turbulence models, renormalized group (RNG) and realizable (RLZ) k-ε. Statistical tests demonstrated that RNG outperformed RLZ k-ε for the prediction of pollutant dispersion and concentration distribution in the emissions study.

In the assessment of wind direction and building configurations, it was found that when the wind approached lateral movement (90°), the downwind length and maximum bilateral width of the low-wind-velocity (LWV) zone in the wake of "T"-shaped buildings decreased. When the incident wind was oblique (45°), the length and width of the LWV zone in the wake of "+"-shaped buildings also decreased. Furthermore, it was found that air pressure on the leeward walls of the "T"- and "+"-shaped buildings gradually decreased with building height.

Two common building arrays, i.e., 'L'- and 'U'-shaped, in Hong Kong were studied, revealing that the former maintained a stronger performance by forming a smaller LWV zone in the central space between buildings. The L-shaped array performed best at an incident wind angle of 225°; whereas a 90° incident angle produced the largest LWV zone for the U-shaped array. Although generally, the L-shaped array better distributed pollutants, the U-shaped array with a 180° wind angle had a smaller high pollutant concentration area than the L-array with a wind angle of 225°. Further, the worst vertical dispersion corresponded to a 135° wind angle for the 'L'-shaped array.

To conclude, appropriate selection of building configurations and arrays, as well as their orientations, will allow for the most effective use of wind flow to enhance ventilation and pollutant dispersion.

PUBLICATIONS ARISING FROM THIS THESIS

Journal Papers

2019 **Lee KY** and Mak CM. A comprehensive approach to study stack emissions from a research building in a small urban setting. *Sustainable Cities and Society* 2019; 51: 101710.

2021 **Lee KY** and Mak CM. Effects of different wind directions on ventilation of surrounding areas of two generic building configurations in Hong Kong. *Indoor and Built Environment* 2021: 1420326X211016040. DOI: 10.1177/1420326X211016040.

2021 **Lee KY** and Mak CM. Effects of wind direction and building array arrangement on airflow and contaminant distributions in the central space of buildings. *Building and Environment* 2021; 205: 108234.

Conference Paper

2019 **Lee KY** and Mak CM. A comprehensive approach to study stack emissions from a research building in a small urban setting. 16th Conference of the International Society of Indoor Air Quality and Climate: Creative and Smart Solutions for Better Built Environments, Indoor Air 2020, 1 November 2020, Seoul, Korea.

ACKNOWLEDGEMENTS

I would like to dedicate this thesis to my late parents. It is my deepest regret that I was not able to complete my research when they were still with me, and that they could not witness my graduation; however, I would not have been able to complete this thesis without their love and support. They will be dearly missed.

My deepest appreciation goes to my supervisor, Prof. Cheuk-ming Mak, for his tireless support, valuable suggestions, and continuous guidance throughout my PhD studies. He has set a wonderful model for me in my future career by being modest, dedicated, earnest, and passionate.

Last but not least, I would like to acknowledge the great efforts put forth by the independent Hong Kong Laboratory Accreditation Scheme (HOKLAS) accredited laboratory, the ALS Technichem (HK) Pty Ltd. for providing dependable laboratory support with the chemical analysis of air samples, and the Health, Safety, and Environment Office of the Hong Kong Polytechnic University for their funding support, technical advice, and logistical arrangements of air sampling across various locations for the emission study.

TABLE OF CONTENTS

LIST OF FIGURES

LIST OF PICTURES

LIST OF TABLES

NOMENCLATURE

Abbreviations

ABL	Atmospheric boundary layer
ACN	Acetonitrile
APCO	Air pollution control ordinance
CFD	Computational fluid dynamics
CFL	Courant-Friedrichs-Lewy number
DES	Detached eddy simulation
FAC2	Factor of two of observations
Gr	Grashof number
H	Building height
HKEPD	Hong Kong Environmental Protection Department
IAQ	Indoor air quality
LES	Large-eddy simulation
LWV	Low-wind-velocity
MG	Geometric mean bias
MVAC	Mechanical ventilation and air conditioning system

NO_2	Nitrogen dioxide
ppb	Parts per billion
ppm	Parts per million
R^2	Correlation coefficient
RANS	Reynolds-averaged Navier-Stokes
Re	Reynolds number
Ri	Richardson number
RLZ	Realizable
RNG	Renormalization group
SF_6	Sulphur hexafluoride
TVOC	Total volatile organic compounds

Greeks Symbols

α	Empirical coefficient
$\acute{\alpha}$	Power law
β	Empirical constant, 0.012
ε	Turbulent viscous dissipation rate ($m^2 \cdot s^{-3}$)
η_0	Model constant
κ	von Karman constant, 0.4187
ρ	Air density ($kg \cdot m^{-3}$)

Parameters

C_1	Empirical constant, 0.025
C_2	Empirical constant, 0.41
C_S	Roughness constant
C_μ	Model constant, 0.069
C	Concentration at the receptor
C_o	Concentration at emission source
C_e	Tracer gas concentration at exhaust outlet

C_{measured}	Measured concentration (ppm)
C_p	Pressure coefficient
C_{source}	Source concentration (ppm)
d	Offset height
H	Building height (m)
H_{ref}	Reference height
I	Turbulence intensity ratio
k	Turbulent kinetic energy ($m^2 \cdot s^{-2}$)
K_c	Non-dimensional concentration
L	Turbulence length
p	Pressure (Pa)
Q	Flow rate ($m^3 \cdot s^{-1}$)
Q_{source}	Flow rate of the source emission ($m^3 \cdot s^{-1}$)
R_{ε}	Strain-dependent term
Sc_t	Turbulent Schmidt number
u	Wind velocity ($m \cdot s^{-1}$)
$u*$	Frictional velocity
U_{ref}	Reference wind speed ($m \cdot s^{-1}$)
v	Wind velocity ($m \cdot s^{-1}$)

w	Wind velocity (m·s^{-1})
y_+	Dimensionless wall distance
y_P	Distance from point P to the wall
z_0	Roughness length (m)

CHAPTER 1 Introduction

1.1 Background and motivation

Similar to other megacities in developed countries, Hong Kong is densely populated, with > 7.4 million people inhabiting 1,106.34 km^2 (Census and Statistics Department of Hong Kong, 2018). Mixes of building types serving different purposes within relatively small urban environments are common, and perhaps even inevitable. Given the high density of buildings, road networks, and land-use types, the emissions from vehicles, and the exhaust stacks of industries and research facilities are likely to adversely affect the health of local inhabitants.

Microclimatic elements, such as wind-speed, wind direction, airflow pattern, and air temperature are also influenced by inter-building proximity and road widths (Ai and Mak, 2016). Lower wind speeds can hinder the dispersion of air contaminants in urban environments, an effect further exacerbated by densely-packed buildings (Du and Mak, 2018; Du et al., 2019). Thus, the resulting distribution and dilution of air pollutants in urban localities are heavily affected by building pattern-controlled airflow (Dai et al., 2018a), and are a primary determinant of local overall air quality of the area (Borrego et al., 2006; Yuan et al., 2014). To best dilute urban air pollutants, wind penetration should be increased through careful planning of the urban setting geometry (Ai et al., 2016; Fang et al., 2019).

Accordingly, external environmental factors, such as wind velocity and airflow sufficiency play an essential role in enhancing humanity's thermal comfort and improving air quality, as do the blockage effects from buildings and other urban structures. To speed up the construction process and maximise ultilisation of limited land space, many developers in Hong Kong tend to construct buildings in particular shapes, and arrange them a common arrays. Numerous studies of wind flow around cubical buildings have been conducted, but its impacts on the natural ventilation and thermal comfort at the ground level have not been adequately investigated, nor have the directionality of wind effects on flow in the wakes of buildings with the configurations and arrays commonly found and unique in Hong Kong.

Unlike industrial or traffic emissions, gaseous emissions from research facilities are difficult to characterize owing to their diverse origin processes, changing nature of research, irregular patterns, and the variability of chemicals with time (Ballinger and Larson, 2014). Lateb et al. (2011) evaluated the effects of stack height and exhaust velocity on the dispersion of air pollutants in the wakes of buildings using a computational fluid dynamics (CFD) model validated with a wind tunnel study.

Similarly, Yassin (2013) investigated the wind flow and pollutant dispersion from rooftop stacks near the wakes of buildings via a wind tunnel experiment; however, stack emissions of research facilities or laboratories, and their corresponding impact on air quality within an actual small and complex urban setting, have not been investigated separately, or assessed completely.

1.2 Aim and objectives

To address the limited number of field measurement-validated CFD studies on complex urban settings (Dadioti and Rees, 2017), in addition to the impacts of research facility emissions within a small urban setting, and the ground level effects for representative configurations and arrays found in Hong Kong, the present study analysed the emissions from a research building of a local university in Hong Kong, and evaluated the correlated nearby impacts. The effects of approaching wind velocities on pollutant dispersion were also identified. The urban setting included an area of a few hundred meters around the studied building, where the interactions of plumes and flow fields were perturbed by the building structures according to Tominaga and Stathopoulos (2013). To this end, building air emissions were monitored for selected chemicals for one year, and a tracer gas study was conducted to identify dilution factors in the environment, and subsequently validate the CFD models. Data from air sampling and tracer gas analyses were compared with the simulated results from the renormalization group (RNG) and realizable (RLZ) k-ε models for pollution dispersion patterns and changes in wind-speed within the building arrays of the selected environment.

As it is not often feasible or economically viable for engineers to carry out full, year-long evaluations of air monitoring, tracer gasses, and CFD simulations for every urban setting and development, it would be preferable to avoid known unfavourable environmental conditions, and make use of the shapes and array arrangements of buildings that optimize outdoor ventilation. Accordingly, this thesis also examined the effects of wind direction on the wind velocity distributions of wakes, and pressure distributions on the leeward walls of two buildings with representative configurations of Hong Kong via CFD simulations. The ultimate objective here was to guide the principles of window position and orientation design optimizing natural ventilation through the tested conditions of building shapes, array arrangements, and orientations to incident wind.

Two residential building designs/configurations, "T"-shape and the "+"-shape, are very common in the urban areas of Hong Kong. In this study, comparisons of the wind velocities at the pedestrian level in the wakes of these two building shapes (under different wind directions) with the normal, “-”-shaped building model configurations, and the distribution of air pressures on their leeward walls were conducted. The turbulence model and computational settings were validated using wind flow data from the wind tunnel test results of the “compilation of experimental data for validation purposes” (CEDVAL) project developed by the Meteorological Institute at the University of Hamburg (Leitl and Schatzmann, 1998). The validated model and numerical settings were then used to simulate the two building shapes, together with the normal building configuration, under different wind directions. As wind flow patterns are closely related to the incident wind direction, three typical wind directions—direct opposing (θ = 0° and θ = 180°), oblique (θ = 45° and θ = 135°), and lateral approaching (θ = 90°)—were selected and simulated via CFD models. The resulting wind flow patterns and wind velocity distributions in two locations—(i) near the leeward wall, and (ii) the building wakes at the pedestrian level—for each of the two building configurations will be discussed in this thesis.

To maximise land utilisation, ‘T’-shaped buildings arranged in‘U’- and ‘L’-shaped building arrays are common inHong Kong. This study further conducted comparisons of airflow patterns and wind velocities at the pedestrian level inside the central spaces of two types of building arrays (with different orientations) to reveal the optimal characteristics for natural ventilation and wind flow to favour pedestrian activities. The pollutant dispersion patterns inside the central space of the building arrays, and on building surfaces were also studied to identify the effects of the array arrangements and wind directions. The turbulence model and computational settings were validated using wind flow data from the wind tunnel test results of the CEDVAL project. The validated model and numerical settings were then used to simulate ‘U’- and ‘L’-shaped building arrays for five different wind directions via the validated CFD model, as the wind flow pattern is closely related to the incident wind direction. Airflow patterns, wind velocity, and contaminant distributions inside of the central space at the pedestrian level of the two building arrays were thus investigated here.

1.3 Thesis outline

The current chapter presents the background and motivation for the research, providing the objectives and significance of the study as well. The remaining chapters of the thesis are organized as follows:

Chapter 2 offers a comprehensive literature review, including experimental details of: air monitoring and tracer gasses; airflow and pressure distributions on building surfaces, and their impact on indoor ventilation; and airflow sufficiency on pollutant dispersion.

Chapter 3 describes an emissions investigation from a research building of a local university in Hong Kong, and the correlated impacts on the nearby area. This chapter further highlights the details of the tracer gas study and CFD simulations.

Chapter 4 investigates the effects of wind directionality on the correlated velocity distributions in the wakes and pressure distributions on the leeward walls of two representative buildings for configurations commonly found in Hong Kong, with an objective to provide insights on the principle of designing window positions and building orientations to optimize natural ventilation.

Chapter 5 evaluates the impacts of building arrays and incident wind directions on the distribution and dispersion of air contaminants within the central space between buildings. Airflow patterns inside these central spaces under different incident wind directions are also elaborated upon.

Chapter 6 summarizes the main contributions and the work conducted for this doctorate, and provides recommendations for future research on the subject concerned.

CHAPTER 2 Literature Review

2.1 Natural ventilation and building design

Since the energy crisis of the 1970s, there is ever-growing concern on the imminent need for energy conservation and tackling the environmental problems of air pollution and climate change. Absolute reliance on mechanical ventilation, such as air-conditioning systems, is not environmentally sustainable, possibly further contributing to the warming effects in urban areas. Presently, naturally-ventilated buildings are common worldwide, and advocated as a significant piece of sustainable and resilient infrastructure development (King et al., 2017), in addition to serving as one of the most effective and economical means of improving indoor air quality and thermal comfort (Sakiyama et al., 2021; Wang and Malkawi, 2019) through the addition of fresh air from the outdoor space (Aflaki et al., 2015). Additionally, natural ventilation can help dilute air pollutants in the external urban space as well, improving the overall air quality in the urban locality (Borrego et al., 2006; Dai et al., 2018a; Lee and Mak, 2019; Yuan et al., 2014).

Natural (i.e., passive) ventilation can be achieved through the exchange of indoor and outdoor air without mechanical assistance, such as fans or air conditioning systems

(Omrani et al., 2017). Air movement and temperature in an indoor environment are caused by the pressure differences on either side of the building surface, and can be severely affected by the outdoor airflow velocity (Aflaki et al., 2015). The air pressure generated crosses building openings through air movement (Etheridge, 2015), helping bring fresh air into the indoors, and discharge aged air on the leeward side (Aflaki et al., 2015). Accordingly, the performance of natural ventilation is reliant upon the position of building openings (e.g., windows), as well as the orientation of the building and its doors (Gao and Lee, 2011). As such, the proper design of building openings in the initial stages of is building development is pivotal for creating the desired passive air movement and thermal comfort (Aflaki et al., 2015).

The overall effectiveness of natural ventilation in urban areas, however, can still be affected by other factors. Firstly, the morphological and meteorological features of urban areas can remarkably alter its benefits (Peng et al., 2020). Building layouts and densities can lead to the occurrence of local air vortices and small-scale air advection, adversely affecting urban air quality, significantly reducing the wind velocity in the middle of the city or street canyon. Secondly, prediction processes of natural ventilation are complicated by the sophisticated physics involved (Omrani et al., 2017). The complexity of geometry, density, and building aspect ratios, as well as the intricacies of the meteorological conditions involved, all complicate wind flow behaviour prediction within an urban setting. Third, there is no consensus on quick and accurate assessment criteria for natural ventilation (e.g., ventilation rates), in the early building design stages (Cheng et al., 2018; Wang and Malkawi, 2019). As such, an optimal evaluation method for assessment must be identified.

With the technological and computational advancements over recent decades, computational fluid dynamics (CFD) simulations have become a powerful tool in the research and design of natural ventilation (Etheridge, 2015). The effects brought by different building envelope designs, in addition to airflow rates and patterns around the building can be modelled by CFD simulations at the design stage. To ensure model sensitivity and accuracy, Omrani et al. (2017) suggested that CFD, in conjunction with experimental data, could be incorporated into the predictions and evaluations of natural ventilation performances. Once validated with experimental results, the CFD model can produce reliable, detailed, and accurate analyses, to be discussed further in Section 2.3 (Omrani et al., 2017).

2.2 Stack emissions from research facilities or laboratory buildings

Air quality and its associated health impacts brought by the air pollutants remain atop of the environmental and public health issues (Kobza et al., 2018). Particulate and gaseous pollutant emissions from industries and auto-exhaust are responsible for rising discomfort, increasing airway disease, decreasing productivity, and the deterioration of artistic and cultural histories in urban centres (Puliafito et al., 2003). Much focus has been placed on the emissions from road vehicles and other industrial sources. For example, in Hong Kong, the Air Pollution Control Ordinance (APCO), enforced by the Environmental Protection Department (EPD), sets out the maximum allowable concentrations for typical air pollutants and emissions, such as nitrogen dioxide (NO_2) and carbon monoxide (CO; (Lee and Mak, 2019); however, unlike these industrial or traffic emissions that are closely monitored and regulated by the EPD, gaseous emissions from research facilities around the world remain insufficiently studied and difficult to characterize owing to their diverse processes, shifting nature of research, and variable chemical use over time (Ballinger and Larson, 2014). The nature of air pollutants and their emission patterns are irregular, relying heavily on research of laboratory activities at any given time; yet, the emissions of toxic chemicals from these facilities can adversely affect human health in the surrounding areas. Lateb et al. (2011) evaluated the effects of stack height and exhaust velocity on the dispersion of air pollutants in a building wake via a CFD model validated through a wind tunnel study, and Yassin (2013) similarly investigated the wind flow and pollutant dispersion from rooftop stacks through a wind tunnel experiment; however, stack emissions of research facilities or laboratory buildings, and their correlated impacts on air quality within an actual small and complex urban setting, have not been thoroughly investigated.

To assess the urban impacts of gas emissions, full-scale air quality field measurements are a straightforward method to identify local concentrations and dispersion patterns within a defined environment; however, such approaches involve high installation- and laboratory-analysis-costs, nor is it always logistically feasible to perform continuous air sampling for extended periods across an large numbers of sampling points (Lee and Mak, 2019). Accuracy of the results is also subject to the placement and density of sampling locations. Furthermore, it is near-impossible to reproduce experimental data in full-scale air monitoring models because of chaotic wind and weather conditions, shifting wind directions, variable pollutant source emissions, and their correlated dispersion patterns (Cremades, 2000; Dai et al., 2018a). Accordingly, numerical methods and CFD techniques have been increasingly used for this purpose, though structured studies addressing effects of gaseous emission from laboratory buildings in urban areas remain lacking. As such, there is a need for more studies of CFD modelling of airflow and contaminant dispersion around building arrays (Liu et al., 2019a). Due to the complex relationship with urban, high building densities, further experimental research on the distribution of airflow and dispersion of air contaminants, particularly from research buildings, within street canyons and building arrays is needed.

2.3 Computational fluid dynamics (CFD) modelling

CFD can generate reproducible results of airflow and dispersion patterns around buildings, a crucial component of assessing air quality, comfort, and the health of nearby inhabitants (Lateb et al., 2013). Moreover, CFD models are significantly less expensive than field measurements and wind-tunnel experiments, and they remain unaffected by the uncontrollable and diverse nature of meteorological conditions (Blocken et al., 2008); however, CFD simulation accuracies are affected by grid resolution, boundary conditions, geometrical representations, computational parameters, and, most importantly, the selection of turbulence models (Lateb et al., 2013; Tominaga and Stathopoulos, 2013).

The Reynolds-averaged Navier-Stokes (RANS) equations are commonly used to resolve turbulence issues and examine the wind flow around buildings, as they focus on the mean flow properties of turbulence, and are less computationally expensive (Blocken, 2015; Xia et al., 2014); however, RANS tends to over-predict the turbulent kinetic energy on the windward side of buildings, and overestimate the reattachment lengths along the roof and wake regions of a building (Lübcke et al., 2001; Mochida and Lun, 2008). Despite these limitations, as well as the tendency to overestimate turbulence formation on the frontal area of buildings (Burman and Jonsson, 2015), RANS can still be modified to calculate microscale wind flow in urban settings (Li et al., 2006), and remains popular for its low computational resource requirements, computing times, and hardware costs.

While the distributions of mean airflow can be obtained by RANS models, various turbulence model families have been developed for them to replicate airflow fluctuations as well (Shirzadi et al., 2020). Among different RANS approaches, k-ε turbulence models are frequently used, and include the standard k-ε model (SKE), renormalization group (RNG) k-ε model, and the realizable (RLZ) k-ε model. Tominaga and Stathopoulos (2013) found that the over-prediction of turbulence kinetic energy in the frontal areas of buildings contributes to the poor performance of SKE models in their description of separation flow. In addition, SKE performance depends on the turbulent Schmidt number to solve the dispersion equation (Gousseau et al., 2011). Compared to transient models, SKE is significantly less accurate when predicting air pollutant concentrations (Gousseau et al., 2011); thus, SKE was not selected for the present study due to its poor performance over complex flows.

The RLZ k-ε model is a more recent development of the SKE model, and it contains a new formulation for the turbulent viscosity and a new transport equation for the dissipation rate derived from an exact equation for the transport of the mean-square vorticity fluctuation (Ansys Fluent v. 14.5, 2012). The RLZ *k*-ε model can provide a more accurate concentration distribution trends for the lower region between two buildings; however, it tends to underestimate the lateral dispersion of pollutants, and overestimate the reattachment lengths of building roofs and wake regions (Lateb et al., 2013). Comparatively, the RNG *k*-ε model provides a more accurate description of complex processes than the other *k*-ε models (Canepa, 2004) because it introduces additional strain-dependent term (R_{ε}) into the calculation of the turbulent dissipation rate (ε; Du et al., 2019). RNG theory provides an analytically-derived differential formula for effective viscosity that accounts for low-Reynolds-number effects, therefore, it could provide effective predictions of performance in regard to the flow of low Reynolds number and near-wall region (Liu et al., 2017), and it produces more realistic results, especially for rapidly strained and swirling flows according to Ai et al. (2013). Accordingly, it provides more accurate and reliable results across a wider class of flows (Lateb et al., 2013), including strained, swirling (Ai and Mak, 2013), and turbulence flows, as well as concentration diffusion in building wakes (Liu and Niu, 2016). The RNG *k*-ε model also measurements provides more consistent results with wind-tunnel experiments (Lateb et al., 2013; Tominaga and Stathopoulos, 2009), in addition to its consideration of turbulence flow and recirculation within street canyons and urban areas (Chan et al., 2002; Koutsourakis et al., 2012). The additional term, R_ε, introduced by RNG in the transport equation for ε is calculated according to Equation (2.1):

$$R_\varepsilon = \frac{C_\mu \rho \eta^3 (1 - \frac{\eta}{\eta_0})}{1 + \beta \eta^3} \cdot \frac{\varepsilon^2}{k} \tag{2.1}$$

where, C_μ, η_0, and β are constants, ρ is the fluid density, k is the turbulent kinetic energy, ε is the turbulent viscous dissipation rate, $\eta \equiv Sk/\varepsilon$, where S is the strain rate scale.

A limited number of CFD studies in complex urban settings have been validated by field measurements (Dadioti and Rees, 2017), particularly with regards to examining emissions research facilities; thus, the thesis here analysed the emissions from a research building of a local university in Hong Kong, and evaluated the related impacts on the nearby area. The effects of approaching wind velocities on pollutant dispersion within an urban neighbourhood and among different building arrays were also identified. The proximate urban area of the present study included an area of a few hundred meters surrounding the studied building, where the interaction of plume and flow field were perturbed by the building structures (Tominaga and Stathopoulos, 2013).

2.4 Airflow characteristics in small urban settings

Outdoor environmental factors play an essential role in air comfort and quality in the urban localities (Borrego et al., 2006; Dai et al., 2018a; Lee and Mak, 2019; Yuan et al., 2014), and studies have found that the urban heat island effect (and associated thermal discomfort) is real issue, as evidenced by the comparatively lower air temperatures observed in rural areas (Yola et al., 2021). Although, low wind speeds promote the accumulation of air contaminants inside of street canyons, adversely affecting outdoor air quality (Ai and Mak, 2017; Chew and Norford, 2018), too strong winds around a building may cause discomfort, or even endanger pedestrians (Du et al., 2017a). Thus, a balance is essential to optimizing wind-based comfort and promoting self-ventilation within urban areas, but achieving this goal is challenging (Du et al., 2017b). The problem is particularly significant in subtropical metropolitan areas like Hong Kong. Hence, the Government of the Hong Kong Special Administrative Region (SAR) proposed the air ventilation assessment (AVA) scheme to improve pedestrian-level air movement by effectively maximizing wind benefits, thus enhancing ventilation and breathability within the urban environment (Ng, 2009).

The benefits of sufficient airflow in outdoor urban environments can be significantly offset or complicated by blockage effects from nearby buildings or other urban structures (Chen and Norford, 2017; Chew and Norford, 2018; Huang et al., 2009; Yim et al., 2009). Increased urban building densities reduces wind flow velocities on the ground surface (Niu et al., 2015), with these effects particularly apparent in the building wakes and along their leeward sides; however, the air quality impacts of reduced flow rates in the building wakes have not been sufficiently investigated. As building shapes, orientations, and layouts influence environmental wind conditions, their proper design can help improve both the perceived wind comfort at pedestrian-level (Mittal et al., 2019), and the surface pressure distribution (Zhao and He, 2017). Numerous studies have proposed additional correlated evaluation parameters, including the air change rate, air age, and ventilation efficiency to assess a building's ability to enhance city ventilation (Bady et al., 2008; Hang et al., 2011; Hang et al., 2009). These parameters can be addressed by careful city planning, and sufficient assessments of urban setting geometry (Ai et al., 2016; Fang et al., 2019).

Sufficient ventilation enhances the thermal comfort of those engaged in urban, outdoor activities (Ai and Mak, 2015; Du and Mak, 2018; Du et al., 2017a; Fang et al., 2019). Research has shown that a mean wind speed of 1.5 $m \cdot s^{-1}$ at pedestrian level ($\leq$ 1.75 m) for 50% of the time, provides the most comfortable summer environment in Hong Kong for pedestrians walking in the shade (i.e., without additional thermal stress from solar radiation; Cheng and Ng, 2006; Ng et al., 2005); thus, areas with mean wind speeds < 1.5 m·s^{-1} at the pedestrian level are low-wind velocity zones, that are considered uncomfortable and unfavourable for pedestrian activity (Du et al., 2017a).

Furthermore, the urban building blockage effects on wind velocity and ventilation subsequently influence the local distribution of air contaminants, whose ultimate dispersal depends on the complex relationships between the flows from the atmosphere and around physical obstacles (Huang et al., 2009). Several studies have found that the higher the wind speed, the lower the pollutant concentrations due to enhanced dispersion (Gao et al., 2008; Tsai and Chen, 2004; Wang et al., 2006). Wind flow patterns are also greatly affected by the incident wind directions (Du et al., 2019).

Airflow velocity can influence indoor, as well as outdoor ventilation. Atmospheric airflow can enhance and control the pressure distributions on building surfaces in a naturally ventilated building, as the inward and outward airflows are driven by the pressure differences produced by wind or buoyancy effects (Jiang et al., 2003; Padilla-Marcos et al., 2017; Wang et al., 2018). Wind generates pressure differences along openings, thus promoting airflow through an internal space (Jiang et al., 2003) and helping dilute interior air contaminants to improve indoor air quality (Dai et al., 2017; Yin et al., 2019; Man et al., 2019) . As such, the effectiveness of natural indoor ventilation is sensitive to changes in window position and building orientation (Aflaki et al., 2015; Deng and Tan, 2019), and it is critical to study the relationships among different shapes of obstacles, buildings, and incident wind angles to characterize their effects on the distributions of wind velocities in the wakes, as well as the air pressure on the leeward surfaces of buildings.

As the effects of wind speed are particularly apparent in building wakes or within the central space of building groups, atmospheric airflow can impact the distribution of air pollutants near building surfaces (Jiang et al., 2003; Padilla-Marcos et al., 2017). Accordingly, building shapes, array arrangement, and incident wind angles influence environmental wind conditions, and thus pollutant distributions in both external and internal urban environments. Many residential buildings in Hong Kong are arranged in different shapes around a central space that includes recreational amenities (e.g., swimming pools, tennis courts, and playgrounds; Lee and Mak, 2019). Therefore, airflow penetration and pollutant dispersion at the pedestrian level in the central space or inner gardens of buildings can significantly affect the health of those engaged in outdoor activities.

2.5 Summary and research gaps

This chapter has reviewed pertinent previous research related to the investigation of airflow and pollutant dispersion in urban environments, and identified the following gaps in research and scientific understanding:

(1) Stack emissions of research facilities, laboratory buildings, and their corresponding impact on air quality within an actual complex urban setting have neither been separately investigated nor fully studied. Real-time air monitoring, together with CFD simulations should thus be conducted to evaluate the impact on local air quality from stack emissions.

(2) Limited research has been conducted regarding the directionality of wind effects on the flow of building wakes for configurations commonly found in Hong Kong. Accordingly, a comprehensive review of the effects on airflow distribution in building wakes and leeward walls based on the incident wind directions and building configurations are needed.

(3) Evaluations of the dispersion of air contaminants in the inner garden areas located in the central spaces of building groups are lacking, indicating the need to investigate the effects of building arrays and incident wind angles on airflow and

contaminant distributions in these areas.

The present research aimed to provide investigations of: (a) emissions from the exhaust stacks of a research building, and the corresponding distribution of contaminants in the nearby, urban locality; (b) effects of wind direction and building configuration on the leeward wall distributions of air pressure, and airflow velocities of building wakes; and (c) effects of incident wind angles and building arrays on the distribution of air contaminants in the inner gardens and central spaces of building arrays.

CHAPTER 3 A Comprehensive Investigation of Stack Emissions from a Research Building in a Small Urban Setting

This chapter describes the impacts of stack emissions from a research building in Hong Kong on nearby urban areas. Fifteen chemicals emitted from the building's laboratories were selected for one year-long air monitoring. Among them, the levels of nitrogen dioxide (NO_2), acetonitrile, and total volatile organic compounds (TVOC) exceeded the predetermined exposure levels suggested by international health authorities. A tracer gas analysis was performed to identify the dilution factor of the environment, and validate the two turbulence models used: renormalized group (RNG) and realizable (RLZ) k-ε models. Statistical tests, including fractional bias (FB), geometric mean bias (MG), and factor of two (FAC2), demonstrated that the RNG (FB, -0.1–0.4; MG, 0.9–1.5; FAC2, 0.7–1.1) was superior to the RLZ k-ε model (FB, -1.2–-0.38; MG, 0.26–0.68; FAC2, 1.47–3.80) for the prediction of pollutant dispersion and concentration distributions. The RNG k-ε model is a popular and economical choice in numerical simulations, although it displayed a mild lapse in the simulated results on the building roof when challenged by MG. As such, a cautious interpretation of the data is required that should be used only in conjunction with air monitoring and tracer gas assessments for a comprehensive approach when examining the impacts of stack emissions in an urban setting.

3.1 Methods

3.1.1 Site descriptions

The ZS Building is a research centre of a university in the urban area of the Kowloon peninsula (near Homantin) in Hong Kong providing approximately 46,000 square-metres construction floor area of teaching and research spaces (Figure 3.1). There are 19 emission stacks installed on the roof of the building, each connected to a laboratory with a chemical fume hood that discharges chemical fumes or vapours into the atmosphere. The Inno Tower (IT) is a 15-story academic building in the same university located ~100 m southeast of the ZS Building (Figure 3.1). Though IT does not house any chemical laboratories, the building is ventilated mechanically via an air-conditioning (MVAC) system, and the fresh air intake is located on its roof, facing the ZS Building.

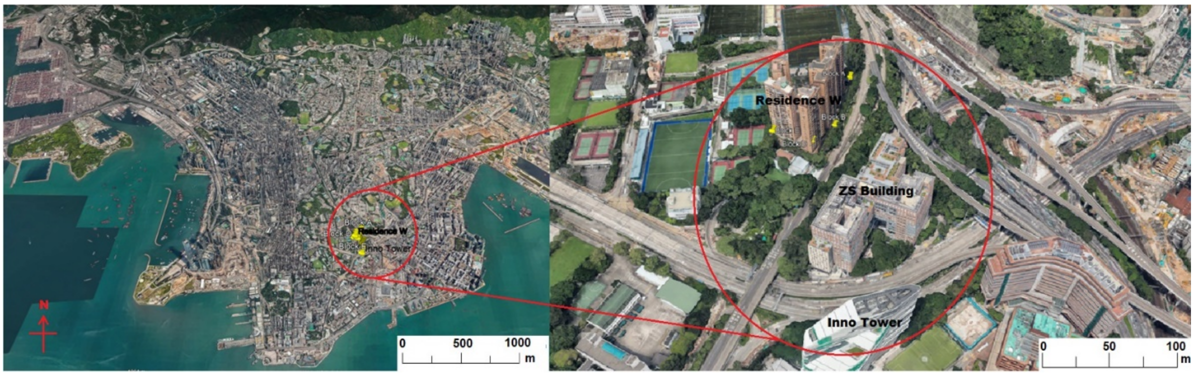

Figure 3.1. Study location in Kowloon of Hong Kong

Private Residence W is located ~100 m northwest of the ZS Building, and comprises five 12-story residential buildings arranged in a 'U'-shape around a central space containing recreational amenities, including a swimming pool and playgrounds. Every building in the complex is separated from the adjacent building by a ~5 m gap, except Blocks A and B, which are abutting without any gap. Gao et al. (2008) observed that source location and wind direction can affect air pollutant dispersion patterns; thus, as Blocks B, D, and E are located closer to the ZS Building, and they are more likely to be affected by the gaseous emissions. Figure 3.2 shows a wind rose diagram illustrating that the prevailing winds in the study area are ~40% southeasterlies (Hong Kong Observatory, 2017); thus Residence W is situated in the wake region of the ZS Building, and more susceptible to the impact of stack emissions for ~40% of the year.

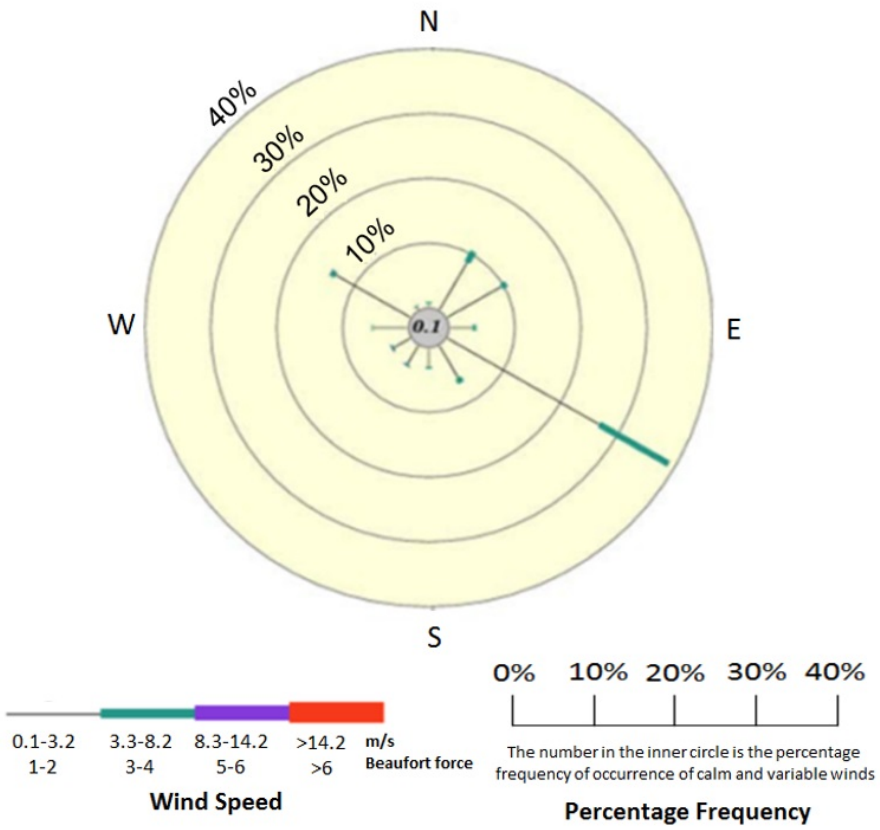

Figure 3.2. Wind rose diagram of 2016 for areas near the ZS Building (Hong Kong Observatory, 2017)

To identify the possible chemical emissions from the laboratories, interviews with all laboratory in-charge persons were conducted. Fifteen chemicals that can create toxic fumes or vapours during reactions or upon exposure to air under normal room temperature conditions, were selected for year-long air quality monitoring.

In Hong Kong, the Air Pollution Control Ordinance (APCO) enforced by the Hong Kong Environmental Protection Department (HKEPD) is the lone regulator of outdoor air pollution, and defines statutory Air Quality Objectives stipulating the maximum allowable concentrations for typical air pollutants, of which nitrogen dioxide (NO_2) and carbon monoxide (CO) are the most relevant to the present study. The exposure limit of formaldehyde is based on the Indoor Air Quality (IAQ) objectives set by the Indoor Air Quality Management Group (IAQMG) of HKEPD in 2003 (Indoor Air Quality Management Group, 2003). For air pollutants not mentioned directly by the APCO or the IAQ objectives, recognized international standards from governing bodies, such as ATSDR and USEPA, were used here. Although varied, acute and chronic exposure parameters were ultimately determined and analysed based on the guidelines of international authorities. Table 3.1 lists the 15 monitored chemicals, their corresponding exposure standards, and the data sources.

Table 3.1 List of 15 monitored chemicals and their exposure limits

Pollutant	**Parameter(s)**	**Exposure Limits**		**Reference**
		(μg·m^{-3})	**(ppb)**	
Acetone	Acute	66,500	26,000	(ATSDR, 1994)
	Chronic	33,200	13,000	(ATSDR, 1994)
Acetonitrile	1-hour	21,294	13,000	(USEPA, 2014)
	Chronic	60	36	(USEPA - Integrated Risk Information System (IRIS), 1999)
Carbon monoxide	1-hour	30,000	26,200	(HKEPD, 2015)
	8-hour	10,000	8,700	(HKEPD, 2015)
Chloroform	Acute	490	100	(ATSDR, 1997)
	Chronic	98	20	(ATSDR, 1997)
Dichloromethane	24-hour	3,000	860	(World Health Organisation, 2000)

	Chronic	600	170	(USEPA - Integrated Risk Information System (IRIS), 2011)
Formaldehyde	Acute	100	81	(Indoor Air Quality Management Group, 2003)
	Chronic	100	81	(World Health Organisation, 2000)
Hydrochloric acid	Acute	2,100	1,410	(OEHHA, 2016)
	Chronic	20	13	(USEPA-Integrated Risk Information System (IRIS), 1995)
Methanol	Acute	28,000	21,370	(OEHHA, 2016)
	Chronic	20,000	15,260	(USEPA- Integrated Risk Information System (IRIS), 2013)
n-hexane	Acute	Not available	Not available	Not available
	Chronic	700	20	(USEPA-Integrated Risk Information System (IRIS), 2005)
Nitric acid	Acute	86	33	(OEHHA, 2016)
	Chronic	Not available	Not available	Not available
Nitrogen dioxide	Acute	200	110	(HKEPD, 2015)
	Chronic	40	21	(HKEPD, 2015)
Tetrahydrofuran	Acute	Not available	Not available	Not available
	Chronic	2,000	680	(USEPA-Integrated Risk Information System (IRIS), 2012)
Toluene	Acute	7,540	2,000	(ATSDR, 2017)
	Chronic	5,000	1,330	(USEPA - Integrated Risk Information System (IRIS), 2005)

Trichloroethane	Acute	10,910	2,000	(ATSDR, 2006)
	Chronic	3,820	700	(ATSDR, 2006)
TVOC	Acute/Chronic	1,000	435	(Nathanson, 1995)
	8-hour (mean)	600	261	(Indoor Air Quality Management Group, 2003)

3.1.2 Air sampling

To identify the impacts from the emissions, air quality samples were obtained from the fresh air intake on the roof of IT, and in different locations and levels of Blocks B, D, and E at Residence W (Figure 3.3). Sample heights at Residence W were obtained on the roof-, mid- (10^{th} floor), and podium-levels; however, due to limited accessibility, mid-level sampling of Blocks B, D, and E were restricted to the back stairwells located in the wake of Residence W. There is an increased risk of contamination near the leeward façades correlated with the fluctuating air stream and reverse flow creating an accumulation of gaseous pollutants in these areas (Mu et al., 2016). The sampling points located in the wake of Residence W could help verify this phenomenon.

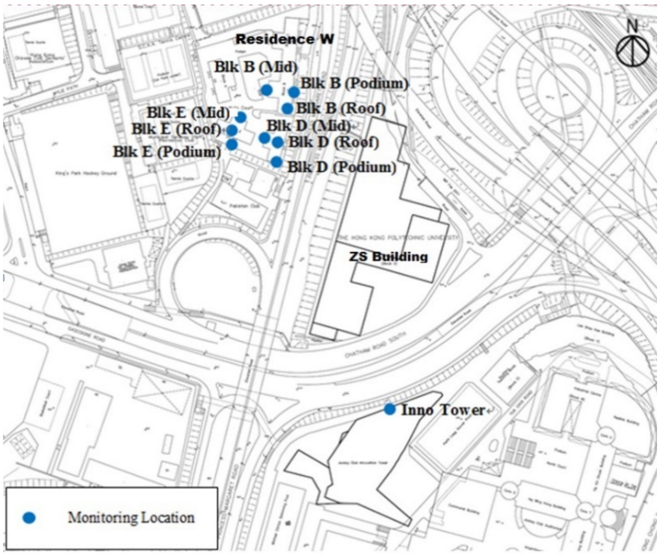

(a)

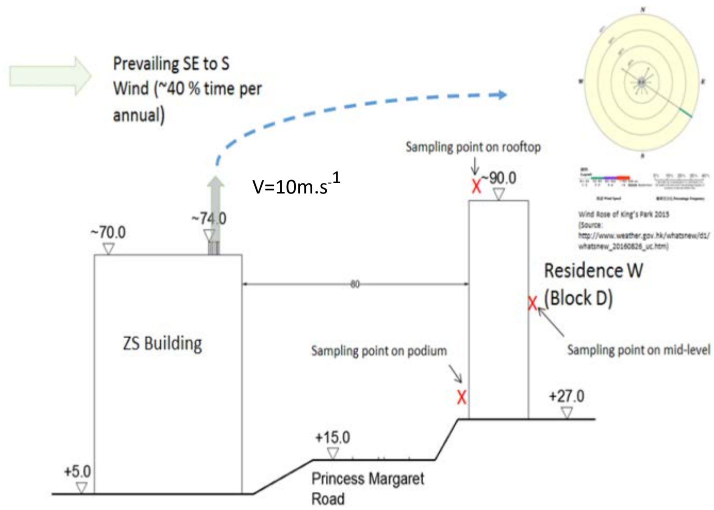

(b)

Figure 3.3 Air monitoring locations: (a) top-view of sampling locations in Residence W and IT, (b) side-view of ZS Building and Block D sampling points in Residence W

Air samples were collected using Nalophan^{TM} bags, stainless steel canisters, and solid sorbent tubes in accordance with the nature of sorted chemicals. During air sampling, ambient weather conditions, including air temperature, wind speed, wind direction, relative humidity, etc., were recorded along with the precise sampling location, equipment used, and sampling time. To minimize any variations introduced by the rainfall, samplings were not collected during rainy days. Following sample collection, the Nalophan™ bags, canister valves, and solid sorbent tubes were tagged with serial numbers, the assigned sample numbers, locations, and dates.

The testing of all chemical parameters was carried out by an independent laboratory, ALS Technichem (HK) Pty Ltd., accredited by local authority to ensure that comprehensive quality assurance and control procedures were in place, and the quality and consistency of laboratory results were certified. All sampling equipment and canisters were thoroughly cleaned before sampling and after use. Food-grade Nalophan™ sampling bags were used for sampling inorganic gases (CO and NO_2), and disposed of after each use. Sampling equipment design at different sampling locations can be seen in Pictures 3.1–3.10.

Pic. 3.1 Resident W - Block D Roof (A1-Roof)

Pic. 3.2 Resident W - Block D Mid (A1-Mid)

Pic. 3.3 Resident W - Block D Podium (A1-Podium)

Pic. 3.4 Resident W - Block B Roof (A2-Roof)

Pic. 3.5 Resident W - Block B Mid (A2-Mid)

Pic. 3.6 Resident W - Block B Podium (A2-Podium)

	
Pic. 3.7 Resident W - Block E Roof (A3-Roof)	**Pic. 3.8** Resident W - Block E Mid (A3-Mid)
	
Pic. 3.9 Resident W - Block E Podium (A3 Podium)	**Pic. 3.10** Inno Tower (IT) Roof

The effects of seasonal changes in wind direction and meteorological conditions were determined based on the changes in ambient concentrations of the selected chemicals while considering the operations inside of the chemical fume hoods under the different weather conditions and seasons of the year. Baseline air quality monitoring analyses were taken when the fume hoods were not in operation, and operational air quality monitoring when all of them were in use. Results were then checked against the exposure criteria shown in Table 3.1 to determine the extent of the pollution. Air samples were collected according to the reference methods and nature of the chemicals listed in Table 3.2.

Table 3.2 Analytical methods and reporting limits for monitoring of the selected chemicals

Chemical	Reference Method	Sampling Time	Reporting Limit
Acetone	USEPA Method TO-15	1 hour	100 ppb (20 ppb*)
Acetonitrile	USEPA Method TO-15	1 hour	100 ppb (20 ppb*)
Carbon monoxide	NDIR Analyzer	1 hour	0.4 ppm
Chloroform	USEPA Method TO-15	1 hour	1 ppb
Dichloromethane	USEPA Method TO-15	1 hour	1 ppb
Formaldehyde	USEPA Method TO-11A	1 hour	20 ppb
Hydrochloric acid	NIOSH Method 7903	2 hours	$0.05\ mg \cdot m^{-3}$ at $0.5\ L \cdot min^{-1}$ for 120 mins ($0.037\ mg \cdot m^{-3}$*)
Methanol	USEPA Method TO-15	1 hour	100 ppb (20 ppb*)
n-hexane	USEPA Method TO-15	1 hour	1 ppb
Nitric acid	NIOSH Method 7903	2 hours	$0.05\ mg \cdot m^{-3}$ at $0.5\ L \cdot min^{-1}$ for 120 mins ($0.037\ mg \cdot m^{-3}$*)
Nitrogen dioxide	Chemiluminescence Analyzer	1 hour	10 ppb
Tetrahydrofuran	USEPA Method TO-15	1 hour	100 ppb (20 ppb*)
Toluene	USEPA Method TO-15	1 hour	1 ppb
Trichloroethane	USEPA Method TO-15	1 hour	1 ppb

Chemical	Reference Method	Sampling Time	Reporting Limit
TVOC	Photo-Ionization Detection	1 hour	1 ppb

*Parenthetical values refer to the lowest unaccredited reporting limit of the laboratory testing instrument. Concentrations reported below the accredited reporting limit were for reference only.

There were 12 baseline and 37 operational air quality monitoring events conducted throughout the year, with no two monitoring events conducted on the same day, so as to decrease the likelihood of any residual effects. Before baseline monitoring, stacks were purged with air; thereafter, the main power supply of all chemical fume hoods within the ZS Building was shut down for ≥ 2 hrs before baseline sampling. Prior to operational air quality monitoring, all laboratories in the ZS Building were visited, and all chemicals in use were identified in order to link sampled pollutants with 3.2 Analytical the respective types and levels of chemicals emitted inside of the fume hoods.

As it could not be assumed that the presence of the more typical urban air pollutants, such as NO_2, CO, and VOCs in the samples were derived solely from the stack emissions, a tracer gas was used to identify the fume hood pollution source and dilution factors in the environment. To this end, sulphur hexafluoride (SF_6), a synthetic gas not normally found in the atmosphere, was used. To achieve a 10,000 ppm (i.e., 1.0% v/v) concentration of SF_6 at the stack discharge, a constant discharge rate inside of the fume hood was maintained at ≥ 78 $L \cdot min^{-1}$ for 30 minutes.hood Table 3.3 and Figure 3.4 present further details of the sampling locations for the tracer gas study.

Table 3.3 Tracer gas monitoring and sampling locations

Monitoring Locations		Sampling Points
A	Inside the laboratory fume hood in the ZS Building	The exhaust duct inlet of the fume hood
B	Inside the stack linked to the fume hood, on the ZS Building roof	At the stack, after the extraction fan
C	ZS Building	Roof (downstream)
D1	Block D of Residence W	Podium level (windward)
D2		Mid-level (leeward)
D3		Roof (windward)

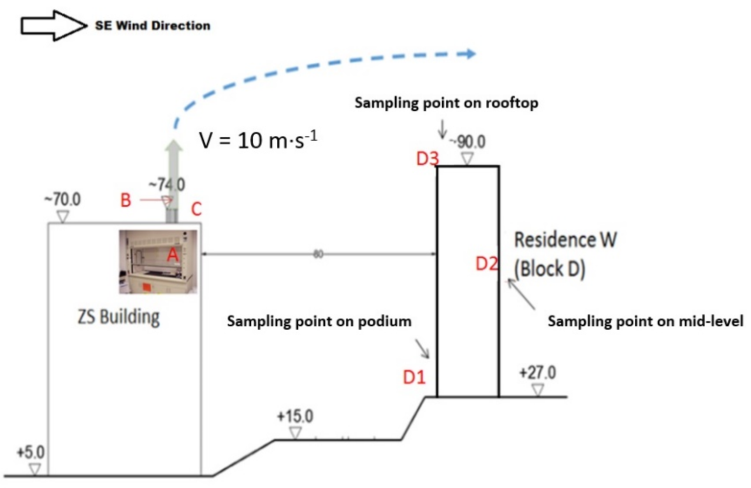

Figure 3.4 Tracer gas monitoring and sampling locations

As SF_6 is a potent greenhouse gas with a high global warming potential (Dervos and Vassiliou, 2000), its use and environmental release in full-scale, tracer gas studies must be carefully planned and performed in an environmentally responsible manner. Constraints on the workforce and sampling equipment dictated the limited number of sampling stations (i.e., A, B, C and Ds) established in this study.

Pic. 3.11 Experimental design of tracer gas monitoring at the ZS Building laboratory fume hood by the author

Eight consecutive 5-minute air samples were collected at the roof of the ZS Building (Point C), and at the podium (D1), mid-level (D2), and roof (D3) of Block D when southeast winds were dominant and Residence W was downstream (see Pic. 3.11). Ambient and the in-stack flue gas temperatures were recorded every 5 minutes throughout the experimental period, and the temperature differences between their averages were used to determine if the thermal and buoyancy effects in CFD simulations were needed. To obtain more reliable results in a stabilized environment, the initial two 5-minute air samples were discarded, and the results from the remaining six samples were used to provide the 30-minute averages of SF_6 concentrations. From the ZS Building, one sample was collected at the exhaust air duct of the fume hood (Point A) for 30 minutes, and the other from inside the emission stack on the roof (Point B) for 40 minutes to permit the tracer gas time to fill up the space inside of the exhaust duct and the stack. The dilution factor (*D*) was calculated at a particular location according to Equation 3.2:

$$D = Ce/C \tag{3.1}$$

where *Ce* is the tracer gas concentration at the exhaust outlet, and *C* is its concentration at the receptor.

3.1.3 Computational fluid dynamics (CFD) modelling

The study location was an urban area where the wind flow is greatly affected by the surrounding buildings; therefore, to capture representative wind conditions of the surrounding area, all buildings in a radius of 8H from the study area, where *H* is the height of the tallest building (85 m) in the study area, were included in the domain. Furthermore, to ensure that the study area was not affected by the domain boundaries, the domain size was determined in accordance with the COST Action 732 (Franke et al., 2007), and the area of interest was extended from the boundary of the study area in the four cardinal directions to a distance of ≥ 15H. The domain height was set to 780 m (8H) in order to cover the inlet wind profile of the study area according to the Planning Department of Hong Kong (Figure 3.5), and provide enough space for the flow development. The wind profile (Figure 3.5) to the southeast of the study area in Hunghom was selected as the model inlet. For areas outside the building group of the study, only the terrain profile was adopted to minimize the blockage effect (Ai and Mak, 2014a). Figure 3.6 illustrates the study domain in the ANSYS Fluent *v*.18.2 environment, along with an aerial photo of the urban area. According to Blocken et al. (2007), horizontal homogeneity can be achieved when the profiles of inlet, approaching, and incident flow are the same. In this context, the wind speed and turbulence intensity profiles provided by the Planning Department of Hong Kong, and the turbulence parameters of adjacent areas, including Tsim Sha Tsui and Hunghom, were nearly the same; thus, the horizontal homogeneity of the flow field was deemed satisfactory, and there was no indication of artificial acceleration within the flow field.

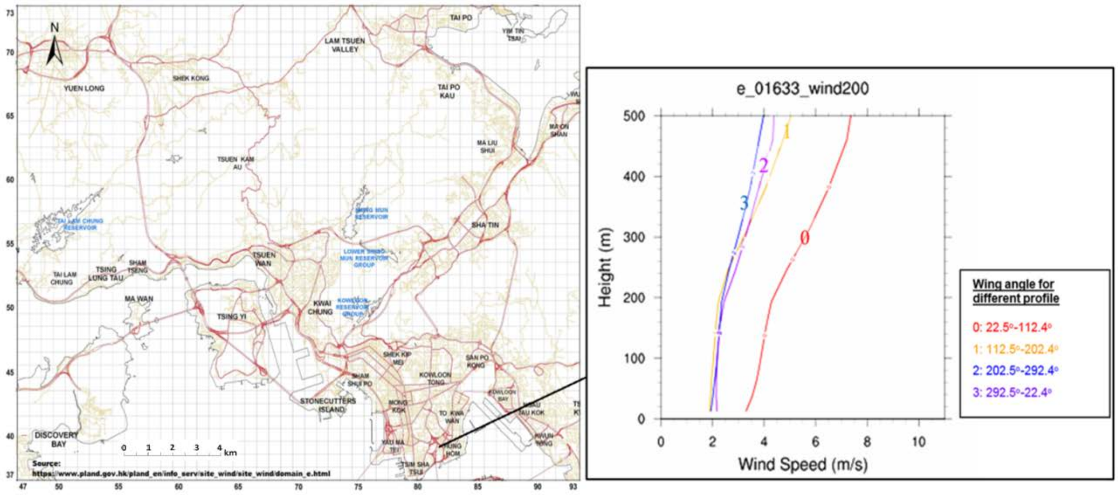

Figure 3.5 Wind profile of the study area, Hunghom, by the Planning Department of Hong Kong

Figure 3.6 Study area domain

ANSYS Fluent *v*.18.2 was used to generate the mesh covers for modelling and simulations. Mesh sizes ranged from 0.02–32.9 m, where finer-scales (0.02–1.66 m) were used for buildings and areas adjacent to the emissions stacks to accurately capture the change of turbulence intensity and viscosity in these areas. The fine meshes also helped predict the flow and pressure distribution (Mirzaei and Rad (2013). In contrast, coarser meshes (0.9–32.9 m) were generated for terrains with a maximum growth ratio of 1.2 in adjacent cells. In the RANS simulations, prediction results did not change significantly with finer grid scales (Tominaga & Stathopoulos, 2012); thus, a standard grid with 17,367,799 tetrahedral cells was adopted instead of a finer scale, which would have necessitated significantly longer computing times. Moreover, a prism layer 2 m above the ground across the entire CFD domain (four layers of 0.5 m thickness) was incorporated in the mesh to better capture the approaching wind at the pedestrian-level. According to Celik et al. (2008), for each equation solved, an iterative convergence with a reduction of ≥ 3 orders of magnitude in the normalized residuals should be ensured before estimating the discretization error. In the present study, converged solutions were assumed when the scaled residuals reached 10^{-3} for continuity, and 10^{-4} for mass conservation, *u, v, w*, *k*, and ε. Under Relaxation Factors (pressure: 0.3; density: 1; body force: 1; momentum: 0.7; turbulent kinetic energy: 0.8; turbulent dissipation rate: 0.8; and turbulent viscosity: 1) in Fluent were used and convergence in the calculation went well. According to Ansys Fluent v. 14.5 (2012) due to the additional non-linearities in the RNG model, lower under-relaxation factors and (for the density-based solvers) a lower Courant number would be necessary. For the RNG k-ε model, > 12,000 iterations were required for all variables to equilibrate or oscillate around a constant value. Despite the residuals for several variables being unable to reach ≤ 10^{-5}, the simulated concentration of SF_6 was essentially constant, oscillating around 3.0×10^{-5}; whereas the residual continuity and k stabilized around 1.25×10^{-4} and 4.8×10^{-5}, respectively, after> 2,000 iterations. For the RLZ k-ε model, all residuals, including the concentration of SF_6, stabilized around the 9,000th iteration, and remained constant for following > 6,000 iterations. As convergence down to very small criteria would result in massively increased computing times, practical convergence criteria were selected to balance the highest quality results with the least amount computing time.

The estimated pollutant concentrations by both RANS simulation approaches were compared to the results from the tracer gas study performed when southeasterly winds were dominant, and Residence W was downstream and in the wake of the ZS Building. To simulate the conditions of dominant southeasterly winds, wind angle 1 (Figure 3.5) was imposed. No-slip conditions and standard wall functions were assumed for the building surfaces and terrain in the computational domain. The updated Davenport roughness classification suggested by Wieringa (1992), and study conducted by Blocken et al. (2012) were used to determine the appropriate roughness length (z_0) of the surrounding study area. Parameters such as roughness height (k_s) and roughness constant (C_s) were found to satisfy the relationship derived by Blocken et al. (2007) Equation 3.2):

$$k_S = 9.793\ z_0/C_s \tag{3.2}$$

In the present study, the z_0 of the terrain was 0.03 according to the Davenport roughness classification proposed by Wieringa (1992), and uniform sand-grain roughness of façades and roofs was employed for building surfaces. A C_s of 0.5, and k_s of 0.1 were used, deriving a z_0 of 0.005 from Equation (3.2). To maintain CFD simulation accuracy, Blocken et al. (2007) also suggested the distance from point P to the wall (y_P) should be larger than k_S, since it is not physically meaningful to have a mesh size with wall-adjacent cells smaller than the roughness height.

The wind direction were southeasterly, and wind speeds were as shown in Figure 3.5; accordingly, the inflows were over the eastern and southern boundaries, and the western and northern boundaries were modelled as the pressure outlets. The sky of the domain was modelled as a mirror plane or symmetrical surface, and the emissions stack (C9) was modelled with a velocity inlet of 2.7 $m \cdot s^{-1}$, according to onsite measurements. The mixture of SF_6 and air, with an SF_6 species mass fraction = 0.002823, was input as the material emitted from C9.

SKE fails to predict the reverse flow on the roofs of buildings due to the over-prediction of turbulence kinetic energy at the impingement region of the windward wall (Liu et al. (2018); moreover, SKE is insufficient to calculate the local pressure distribution in urban environments (Shirzadi et al., 2018). Accordingly, RNG and RLZ *k*-ε models were adopted to investigate windward tracer gas concentrations. Simulated SF_6 concentrations on the building roof, as well as the wake recirculation and vortex shredding behind Residence W, were compared with the tracer gas results to identify the optimum models for this urban setting. Simulations were conducted with the commercial CFD program ANSYS Fluent *v*.18.2. A commonly adopted turbulent Schmidt number (S_{Ct}) of 0.7 in most CFD studies for turbulent mass diffusion was used here (Tominaga and Stathopoulos, 2007), and the corresponding results from simulating the far downwind positions of a rectangular building agreed well with experimental data using *k*–*ε* models (Li and Stathopoulos, 1997).

The Semi-Implicit Method for Pressure-Linked Equations (SIMPLE) pressure-velocity coupling and second-order discretization scheme were used to enhance precision. Thermal and buoyancy effects were not actively considered in the study for the following reasons: First, the turbulence of a high wind-speed in the study area (> 0.9 $m \cdot s^{-1}$) overwhelmed the influence of thermal forces (Niu and Tung, 2008). Second, the emissions stacks are connected to a chemical fume hood directly exhausting fumes and vapours without heating. Third, the measured ambient air and internal emissions stack temperatures were roughly equal (the temperature difference was 0.1 °C or 0.1 K). A non-dimensional parameter, Richardson number (*Ri*), was used to represent the effect of buoyancy on flow shear (Bradshaw, 1969), and defined according to Equation 3.3:

$$Ri = Gr/Re^2 \tag{3.3}$$

where Gr is the Grashof number, and Re is the Reynolds number (5.99×10^5). In the present study, Gr for a case with a small temperature difference of < 3 °C was 3.05×10^{10} (Garbrecht, 2017), leading to a calculated Ri of 0.085 (notably < 0.1). Since natural convection (buoyancy) is negligible when Ri < 1, it was not necessary to consider thermal or buoyancy effects in the simulation.

Validation of numerical results from the tracer gas study is essential to assigning confidence to the predictions; thus, the fractional bias (FB), geometric mean bias (MG), and the fraction of predictions within a factor of two of observations (FAC2) were used in this study (Kumar et al. (1993) Tewari et al. (2010). These statistical indices were selected because: FB has been frequently used for validating CFD models (Chang and Hanna, 2004; Chowdhury et al., 2018; Efthimiou et al., 2018; Kumar et al., 1993); MG is also considered appropriate for dispersion models where the concentrations can vary by multiple orders of magnitude (Chang and Hanna, 2004); and FAC2 robustness is superior since it is insensitive to the distribution of variables under evaluation. The acceptable ranges of FB (-0.5–0.5; Kumar et al. (1993); MG (0.7–1.3), and FAC2 (0.5–2.0; Tewari et al. (2010) were adopted here.

3.2 Results

The comparison between air quality measurements and the predetermined exposure limits (Table 1) revealed that the measured concentrations of all selected chemicals were generally within the permissible exposure limits, with the following exceptions:

i. NO_2 levels measured at all sampling locations, for both baseline and operational air monitoring events, exceeded the chronic exposure criteria.

ii. Occasional measurements above the acute exposure criteria for TVOC were recorded at the mid-level of Block D, and all levels of Blocks B and E in Residence W.

iii. Occasional measurements above the chronic exposure criteria for acetonitrile were recorded at all sampling locations in Residence W, and on three distinct episodes in IT.

Since the predetermined exposure levels for the remaining chemicals were not exceeded at any point, the following discussion focuses solely on NO_2, TVOC, and acetonitrile.

3.2.1 Air monitoring results

3.2.1.1 Nitrogen dioxide (NO_2)

The operational air monitoring results revealed that mean NO_2 levels across all sampling locations ranged between 23.8–25.2 ppb, exceeding the chronic criterion (21 ppb) set by the HKEPD (2015); whereas baseline NO_2 levels similarly measured 23.8–24.9 ppb, also exceeding the chronic criterion. According to the site measurement data, it was observed that the mean NO_2 levels exceeded the chronic threshold regardless of the wind direction (obtained from the Hong Kong Observatory) in the adjacent areas during monitoring.

Comparing the monitoring results with the average annual background NO_2 levels of 29 ppb recorded in 2016 by the nearest Air Quality Monitoring Station (AQMS; HKEPD, n.d.), the average monitored NO_2 levels in the present study were similar. Therefore, it was concluded that the exceeding NO_2 pollution in Residence W and IT possibly resulted from background contributions of the affected area, and not single emission sources from the ZS Building.

3.2.1.2 Total volatile organic compounds (TVOCs)

The TVOC concentrations are presented for the baseline (Figure 3.7a), operational air monitoring for IT (Figure 3.7b), and Blocks B (Figure 3.7c), D (Figure 3.7d), and E (Figure 3.7e) of Residence W. Figure 3.7f displays all results of TVOC levels on a single graph, revealing a similar, shared trend amongst them. Both baseline and operational levels peaked > 400 ppb in the late summer and early autumn. These results also indicated that environmental TVOC concentrations were relatively uniform and constant across the research area period. Pre-existing TVOC concentrations could be a key contributing factor to the TVOC levels observed; however, a gap between the operational and the baseline air monitoring levels was observed in June and July (Figure 3.7f). As laboratory activities were ongoing during the period of operational air monitoring, a correlation between the activities in the ZS Building and higher TVOC readings in Residence W and IT during that period is possible.

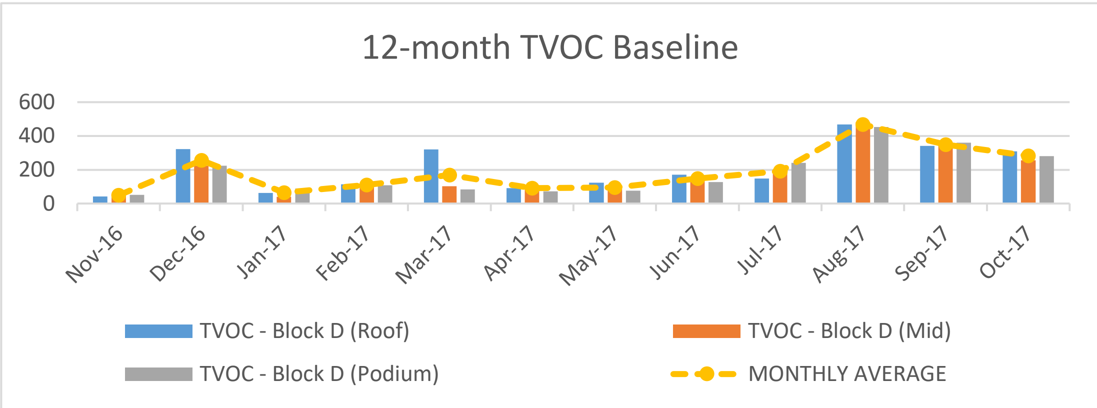

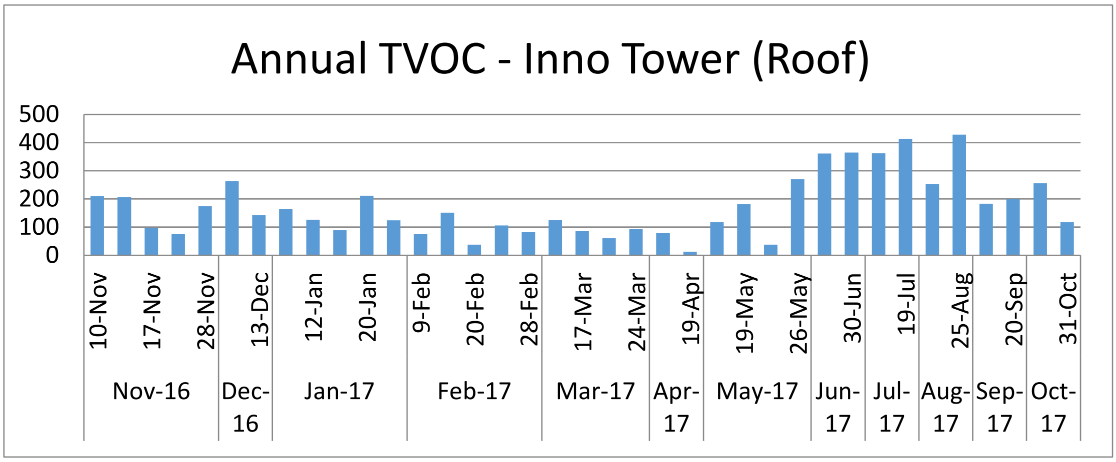
Annual TVOC - Inno Tower (Roof)
500
400
300
200
100
0
10-Nov
17-Nov
28-Nov
13-Dec
12-Jan
20-Jan
9-Feb
20-Feb
28-Feb
17-Mar
24-Mar
19-Apr
19-May
26-May
30-Jun
19-Jul
25-Aug
20-Sep
31-Oct
Nov-16
Dec-16
Jan-17
Feb-17
Mar-17
Apr-17
May-17
Jun-17
Jul-17
Aug-17
Sep-17
Oct-17

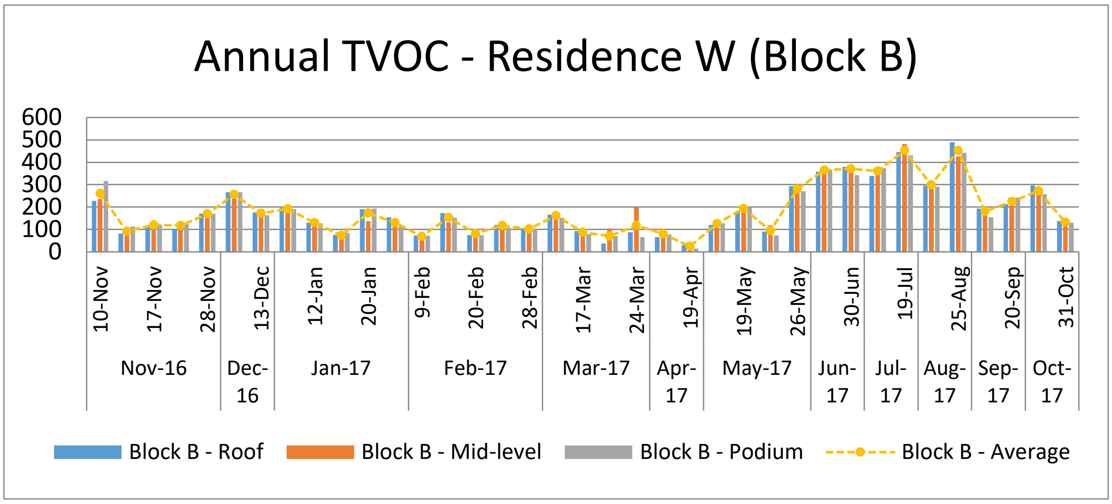
Annual TVOC - Residence W (Block B)
600
500
400
300
200
100
0
10-Nov
17-Nov
28-Nov
13-Dec
12-Jan
20-Jan
9-Feb
20-Feb
28-Feb
17-Mar
24-Mar
19-Apr
19-May
26-May
30-Jun
19-Jul
25-Aug
20-Sep
31-Oct
Nov-16
Dec-16
Jan-17
Feb-17
Mar-17
Apr-17
May-17
Jun-17
Jul-17
Aug-17
Sep-17
Oct-17
Block B - Roof
Block B - Mid-level
Block B - Podium
Block B - Average

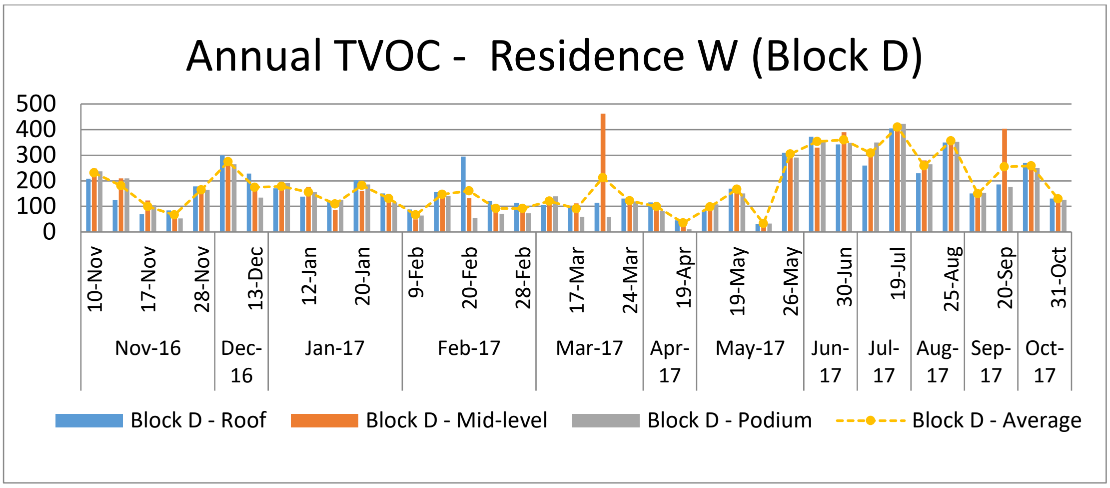
Annual TVOC - Residence W (Block D)
500
400
300
200
100
0
10-Nov
17-Nov
28-Nov
13-Dec
12-Jan
20-Jan
9-Feb
20-Feb
28-Feb
17-Mar
24-Mar
19-Apr
19-May
26-May
30-Jun
19-Jul
25-Aug
20-Sep
31-Oct
Nov-16
Dec-16
Jan-17
Feb-17
Mar-17
Apr-17
May-17
Jun-17
Jul-17
Aug-17
Sep-17
Oct-17
Block D - Roof
Block D - Mid-level
Block D - Podium
Block D - Average

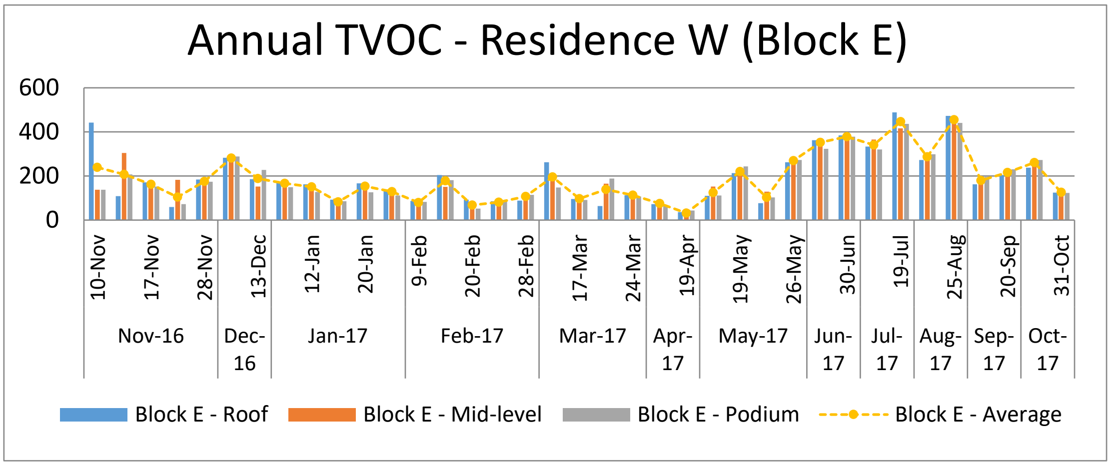

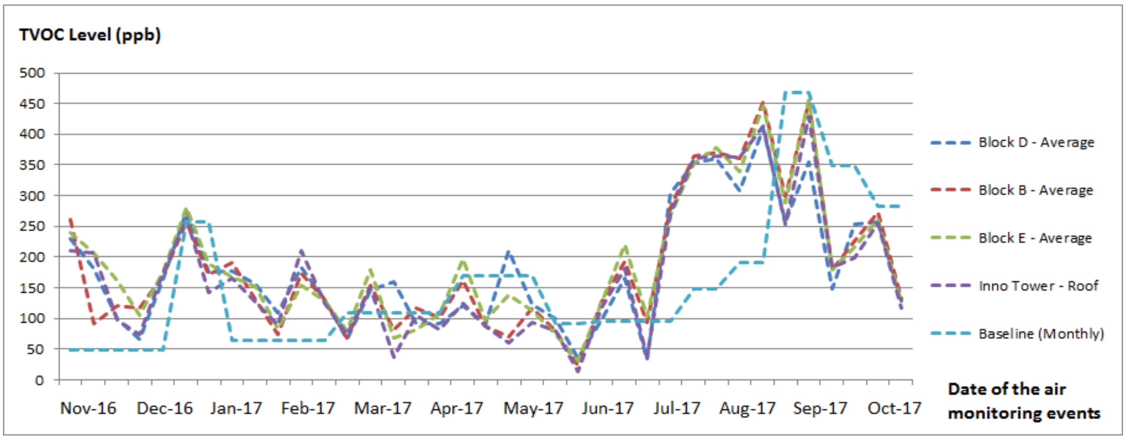

Figure 3.7. (a) Baseline of twelve-month total volatile organic compounds (TVOC); monthly-levels of TVOC for (b) IT; (c) Residence W (Block B); (d) Residence W (Block D); (e) Residence W (Block E); and (f) Comparison of average monthly TVOC levels between baseline and operational air monitoring events.

Baseline monitoring results revealed that the TVOC levels in Residence W ranged from 40 to 485 ppb, surpassing acute levels (> 435 ppb) across all monitoring locations during mid-summer. When compared with the Good Class Indoor Air Quality (IAQ) levels of TVOC (261 ppb) suggested by Indoor Air Quality Management Group (2003), this limit was repeatedly exceeded in Block D: four times on the roof, two times at the mid-level, and three times on the podium level. Baseline measurements of ambient

TVOC levels also frequently exceeded 261 ppb. Figure 3.7f shows that similar patterns and peaks of TVOC levels were observed in both baseline and operational (four buildings, ten sampling points) air monitoring events throughout the year.

It is worth noting that renovation activities were carried out on the 20th floor of Block B; 5th, 12th, 13th, and 14th floors of Block D; and 8th, 10th, and 20th floors of Block E, and elevated TVOC (> 435 ppb) levels were recorded near these locations. Therefore, it was concluded that the construction/renovation activities in Residence W led to a substantial increase in the TVOC results of the field study.

3.2.1.3 Acetonitrile (ACN)

The trends of acetonitrile (ACN) levels are presented for the baseline (Figure 3.8a), and operational air monitoring measurements of IT (Figure 3.8b), Blocks B (Figure 3.8c), D (Figure 3.8d), and E (Figure 3.8e) of Residence; whereas Figure 3.8f combines the results obtained from both baseline and operational air monitoring measurements. The field data revealed that ACN levels mostly fell below the defined hazardous thresholds, with occasional peaks at different locations and times unrelated to wind direction or ZS building laboratory activities. Relatively high ACN values surpassed chronic exposure levels (> 36 ppb) at Residence W in crosswind, downwind, and upwind conditions. Accordingly, no direct evidence could support that the ZS Building activities contributed to the sporadic peaks recorded throughout the year; thus, it is likely that other nearby sources contributed heavily to the observed ACN levels.

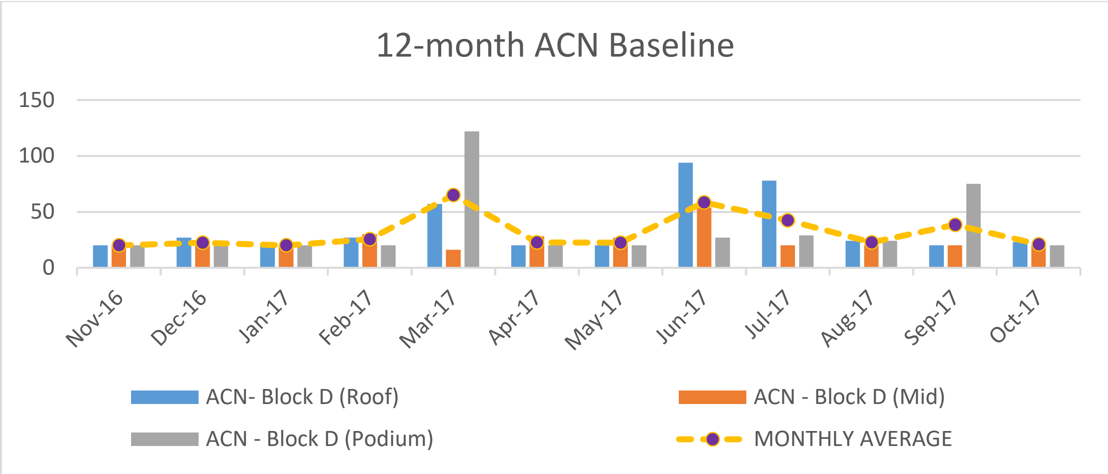

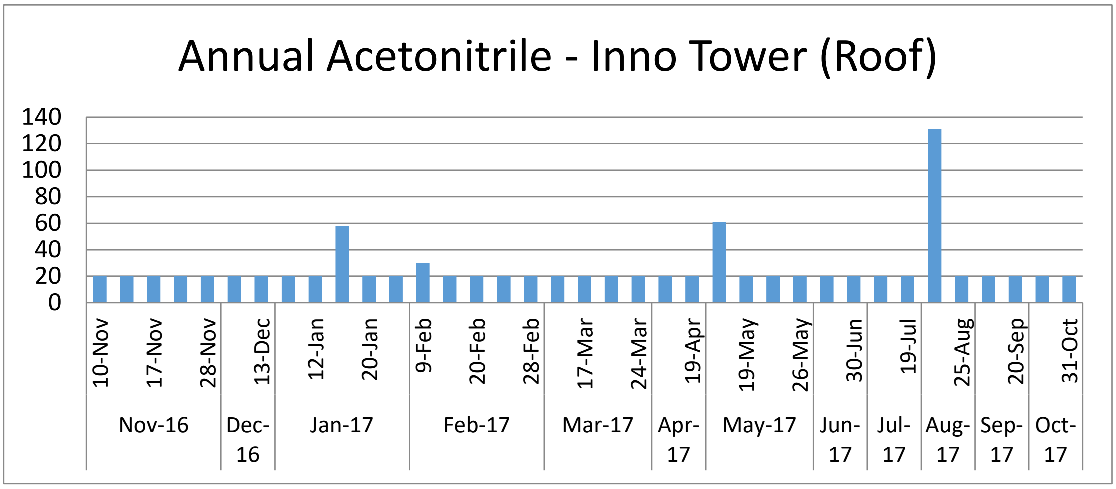

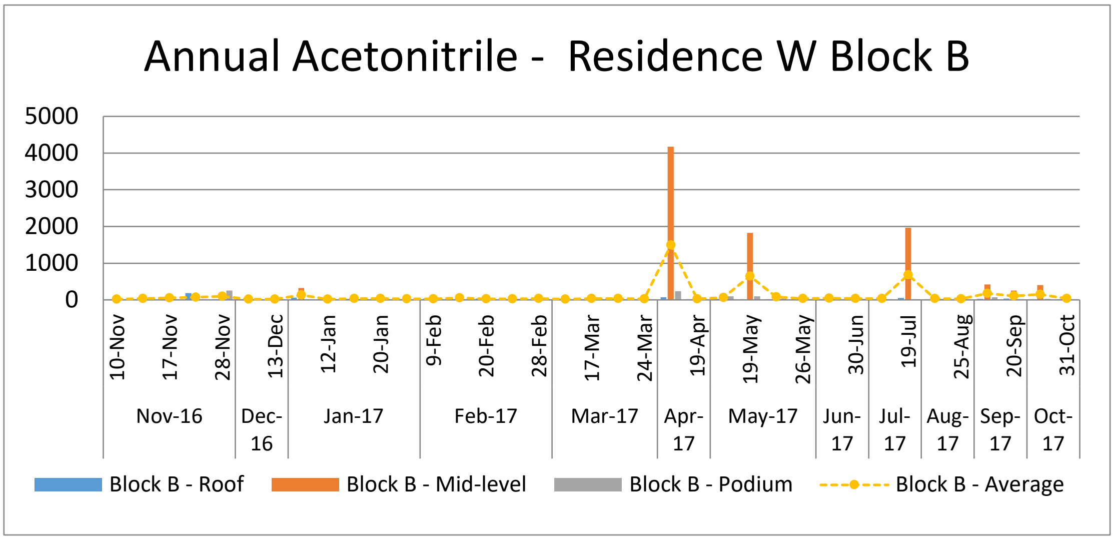
Annual Acetonitrile - Residence W Block B
5000
4000
3000
2000
1000
0
10-Nov
17-Nov
28-Nov
13-Dec
12-Jan
20-Jan
9-Feb
20-Feb
28-Feb
17-Mar
24-Mar
19-Apr
19-May
26-May
30-Jun
19-Jul
25-Aug
20-Sep
31-Oct
Nov-16
Dec-16
Jan-17
Feb-17
Mar-17
Apr-17
May-17
Jun-17
Jul-17
Aug-17
Sep-17
Oct-17
Block B - Roof
Block B - Mid-level
Block B - Podium
Block B - Average

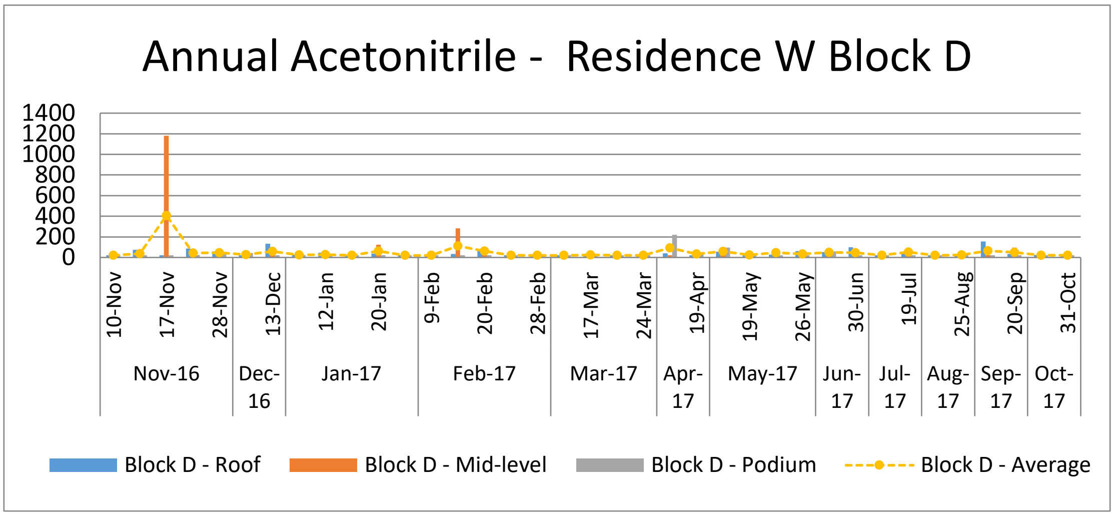
Annual Acetonitrile - Residence W Block D
1400
1200
1000
800
600
400
200
0
10-Nov
17-Nov
28-Nov
13-Dec
12-Jan
20-Jan
9-Feb
20-Feb
28-Feb
17-Mar
24-Mar
19-Apr
19-May
26-May
30-Jun
19-Jul
25-Aug
20-Sep
31-Oct
Nov-16
Dec-16
Jan-17
Feb-17
Mar-17
Apr-17
May-17
Jun-17
Jul-17
Aug-17
Sep-17
Oct-17
Block D - Roof
Block D - Mid-level
Block D - Podium
Block D - Average

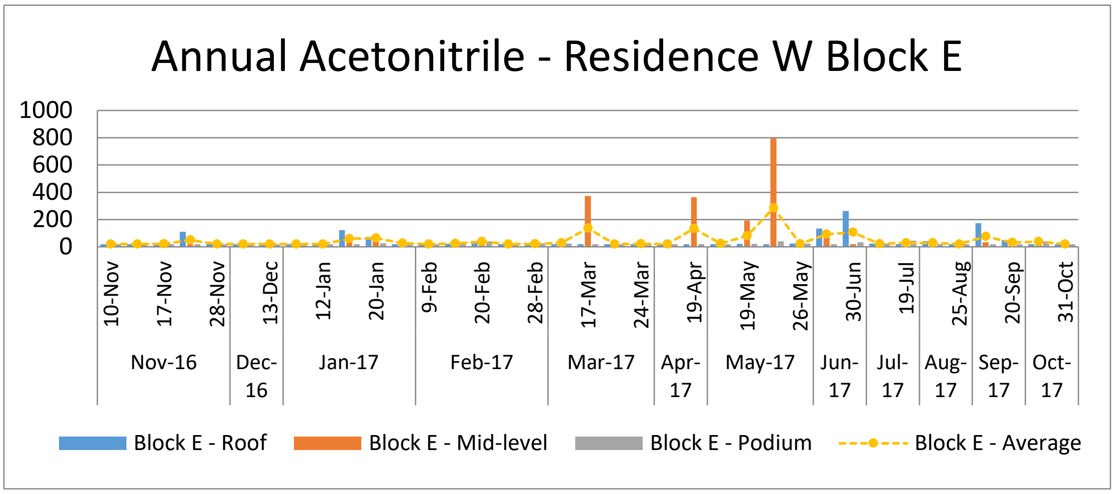
Annual Acetonitrile - Residence W Block E
1000
800
600
400
200
0
10-Nov
17-Nov
28-Nov
13-Dec
12-Jan
20-Jan
9-Feb
20-Feb
28-Feb
17-Mar
24-Mar
19-Apr
19-May
26-May
30-Jun
19-Jul
25-Aug
20-Sep
31-Oct
Nov-16
Dec-16
Jan-17
Feb-17
Mar-17
Apr-17
May-17
Jun-17
Jul-17
Aug-17
Sep-17
Oct-17
Block E - Roof
Block E - Mid-level
Block E - Podium
Block E - Average

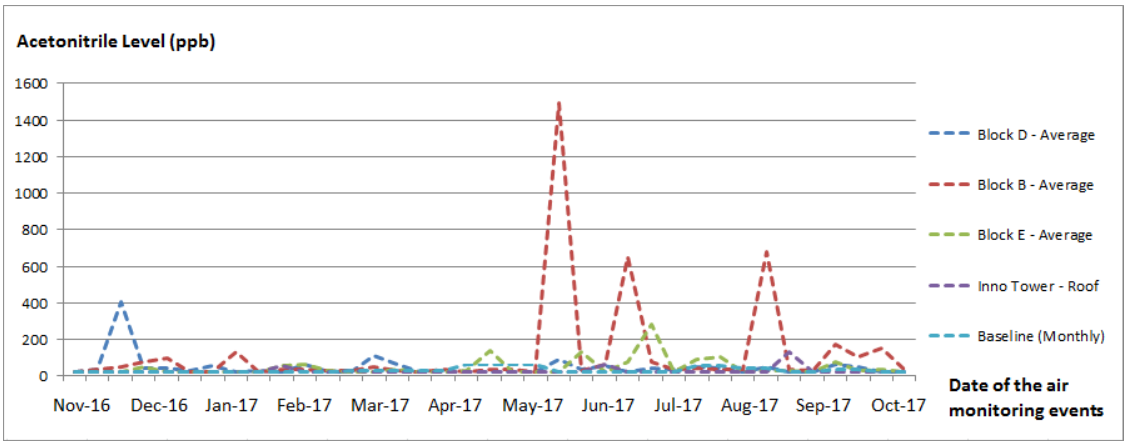

Figure 3.8. (a) Baseline of twelve-month acetonitrile (CAN measurements); monthly levels of ACN for (b) IT; (c) Residence W (Block B); (d) Residence W (Block D); (e) Residence W (Block E); and (f) Comparison of average monthly ACN levels between baseline and operational air monitoring events.

3.2.2 Tracer gas study

A full-scale tracer gas study was used to rule out the effects of environmental factors, such as cigarette smoke, burning of materials, and nearby renovation work, in addition to quantifying the urban environment's dilution effects on the gaseous stack emissions. Further, the environmental dilution factor identified help inform and validate the simulated results of the CFD model.

Stack information and the measurement results are summarized in Tables 3.4 and 3.5, respectively.

Table 3.4 Characteristics of the tracer gas emissions

Experimental setup	
Average flue gas velocity ($m \cdot s^{-1}$)	2.7
Flue gas temperature (°C)	28.1*
SF_6 concentration inside stack (ppb)	2.823×10^6
Wind direction at source (°)	Southeast (143)
Wind-speed at source ($m \cdot s^{-1}$)	4
Ambient temperature (°C)	28*
Tracer gas emission rate ($g \cdot s^{-1}$)	0.085

Average temperature over the 30-minute tracer gas sampling

Table 3.5 Results of SF_6 monitoring (ppb) at each measurement location

Sampling time	SF_6 Concentrations (ppb)					
	Inside fume hood	In-stack (Source) ***Ce***	Roof of ZS Building ***C***	Block D (Podium) ***C***	Block D (Mid) ***C***	Block D (Roof) ***C***
14:30–15:00	2.4396×10^7	2.823×10^6	1–95 (15.8)	1–18 (4.3)	4–16 (10)	1–17 (4)
Dilution factors (*D*)			178,671	656,512	282,300	705,750

Arithmetic means of 30-minute samplings, comprising six five-minute samplings, are given in brackets ( ).

The emitted tracer gas was highly diluted by the environment before reaching the monitoring devices in Residence W (Table 3.5), with the dilution factor (*D*) ranging from 178,671 to 705,750. Notably, the concentration of the tracer gas at the mid-level was more than twice those on the podium or roof levels of the same building in Residence W. As previously mentioned, the mod-level sampling locations was on the leeward side of the building, demonstrating that the tracer gas was significantly diluted upon reaching the roof and podium along the windward side, but managed to accumulate in the mid-level wake region of Residence W.

3.2.3 CFD model results

The RNG and RLZ k-ε turbulence models generated simulation results for comparison with the tracer gas study observations. The limited spatiotemporal coverage of the tracer gas study in the residential buildings and the urban environment, meant few experimental data could be included in the comparison. Table 3.6(a) and (b) summarize the comparisons among the data generated by the RNG and RLZ k-ε models, as well as the tracer gas sampling.

Table 3.6 Comparison between the tracer gas sampling results and the simulated results from the: (a) RNG k-ε, and (b) RLZ k-ε models

Location		**Concentration of Tracer Gas (ppb)**		**Statistical Tests**		
		Tracer Gas Sampling	*RNG k-ε Estimates*	*FB*	*MG*	*FAC2*
Residence W	Block D (Roof)	4.00	2.66 (-33.5%)	0.4	1.5	0.7

	Block D (Pod.)	4.30	4.91 (+12.4%)	-0.1	0.9	1.1
	Block D (Mid)	10.00	7.49 (-25.1%)	0.3	1.3	0.8
ZS Building	Roof	15.80	12.80 (-19.0%)	0.2	1.2	0.8

Acceptable ranges for FB: -0.5–0.5 (Kumar et al., 1993); MG: 0.7–1.3; FAC2: 0.5–2 (Tewari et al., 2010)

Location		**Concentration of Tracer Gas (ppb)**		**Statistical Tests**		
		Tracer Gas Sampling	*RLZ k-ε Estimates*	*FB*	*MG*	*FAC2*
Residence W	Block D (Roof)	4.00	5.86 (+46.5%)	-0.4	0.7	1.5
	Block D (Pod.)	4.30	12.8 (+197.7%)	-1.0	0.3	3.0
	Block D (Mid)	10.00	24.7 (+147%)	-0.9	0.4	2.5
ZS Building	Roof	15.80	60.0 (+279.7%)	-1.2	0.3	3.8

Acceptable ranges for FB: -0.5–0.5 (Kumar et al., 1993); MG: 0.7–1.3; FAC2: 0.5–2.0 (Tewari et al., 2010)

There were significant differences between the simulated data from the RLZ *k*-ε model and sampled results (Table 3.6b). The FB for the RNG *k*-*ε* results ranged from -0.1 to 0.4 (acceptable range: -0.5–0.5), notably better than the results of the RLZ *k*-*ε* model (-1.2–ˉ0.4).The MG for the RNG *k*-*ε* results ranged from 0.9 to 1.5 (acceptable range: 0.7–1.3), also superior to the RLZ *k*-*ε* model results (0.3–0.7). The FAC2 for the RNG *k*-*ε* model ranged from 0.7 to 1.1 (acceptable range: 0.5–2.0), while that for the RLZ *k*-*ε* model ranged between 1.5 and 3.8.

Overall, the RLZ *k*-*ε* model was less accurate compared to the RNG *k*-*ε* model. In general, the RLZ k-ε model overestimated tracer gas concentrations across all sampling locations, particularly for the building wake region and near the emission source (estimated tracer gas concentrations on the ZS Building roof were nearly 280% of the observed concentration). In contrast, the RNG k-ε model provided more accurate results within narrower ranges of variation (-33.5–12.4%). Generally, the results from the RNG k-ε model agreed well with the tracer gas data for downstream (ZS Building roof) and windward side (Block D-Podium) measurements, save for a relatively small deviation on the roof of Block D where the MG (1.5) exceeded the upper acceptable limit; although, these estimates still remained within the tolerable limits of FB and FAC2.

Figure 3.9 illustrates the distribution and dispersion pattern of the tracer gas within the research area. The RLZ k-ε model produced a narrower lateral spread of tracer gas (Figure 3.9a) compared to the RNG k-ε model, which demonstrated the recirculation of tracer gas in the wake regions of IT and the ZS Building, as well as along the windward side of the latter building. The RNG k-ε model simulation highlights the dominance of the concentration transport along the upwind direction by advection, and captured the upwind concentrations between the ZS Building and IT (Fig. 9b). In such cases, the air pollutants from the stack would be trapped and accumulate in the recirculation zone (central space of the buildings) in Residence W, and along the leeward side of IT.

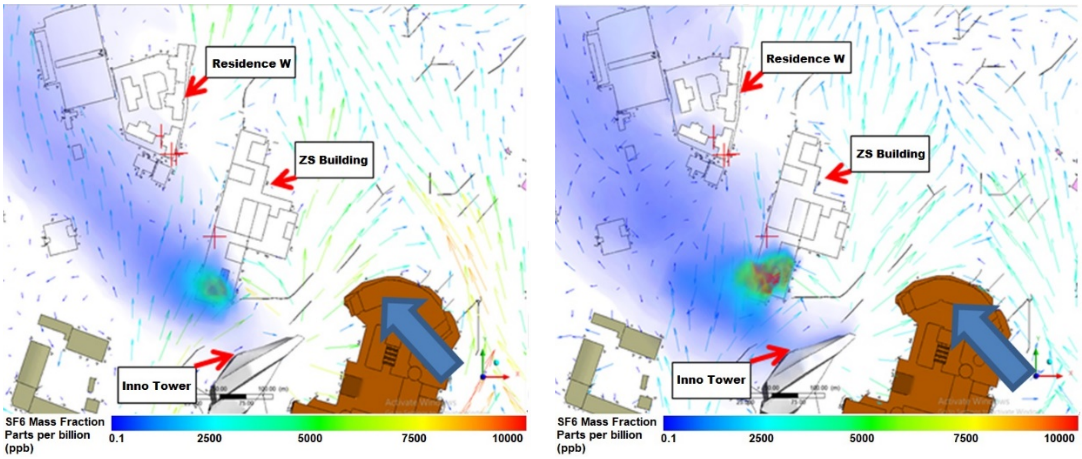

(a) (b)

Figure 3.9 Dispersion pattern of SF_6 simulated by the: (a) RLZ k-ε model and (b) RNG k-ε model. + denotes the locations of tracer gas sampling, and denotes the wind direction

Figure 3.10 shows the ratio of mean SF_6 concentrations (C) by measuring site compared to the emission source concentrations (C_0), and a remarkable difference between the mean concentration distributions for both RANS simulations can be seen. The RLZ *k*-ε model overestimated tracer gas concentrations along the windward wall (Figure 3.10a) and central space (Figure 3.10c) of Residence W, but underestimated upstream concentration distributions on the leeward wall of IT (Figure 3.10b). In Figure 3.10a, the concentration distribution on the windward wall of Residence W was relatively stable in the lower- and mid-levels (z = 30–50 m), and decreased gradually after z = 50 m. Similarly, Figure 3.10c shows that the concentration distribution within the central space of Residence W was comparatively higher in the low- and mid-levels, and weakened from z ≥ 50 m; however, Figure 3.10b shows a gradually increasing concentration distributions from at z = 20 m on upward along the leeward wall of IT, peaking at z = 70 m in RNG *k*-ε, and z = 50 m in RLZ *k*-ε. These patterns of tracer gas with height may derive from the weakening effluent momentum of contaminants and flow velocities, as predicted by the models.

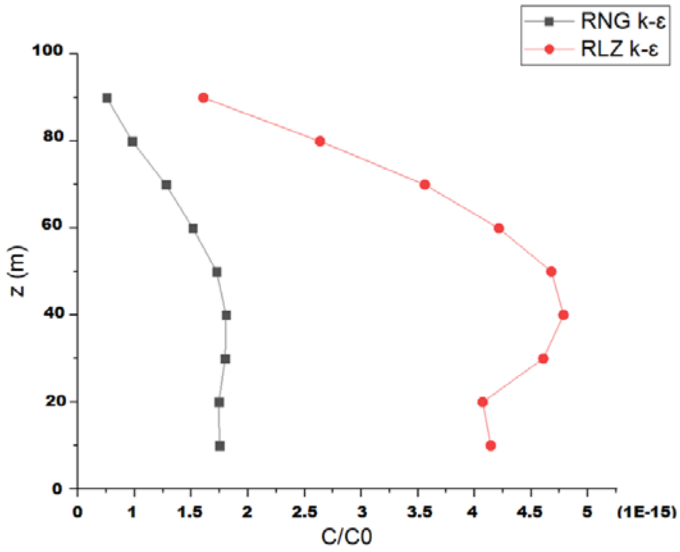

(a)

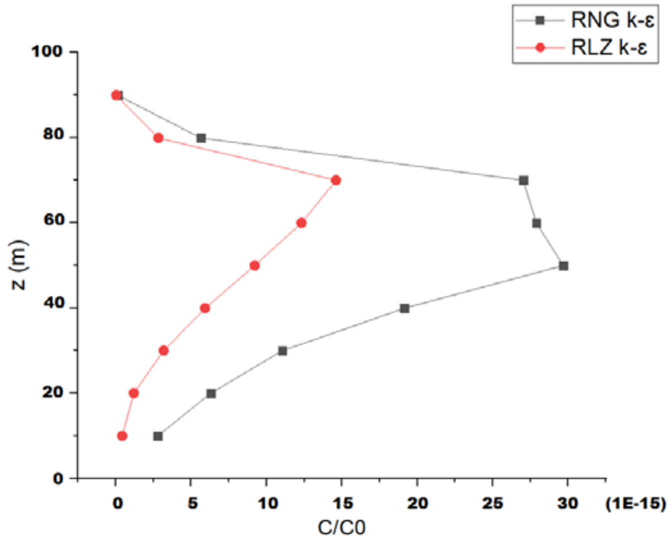

(b)

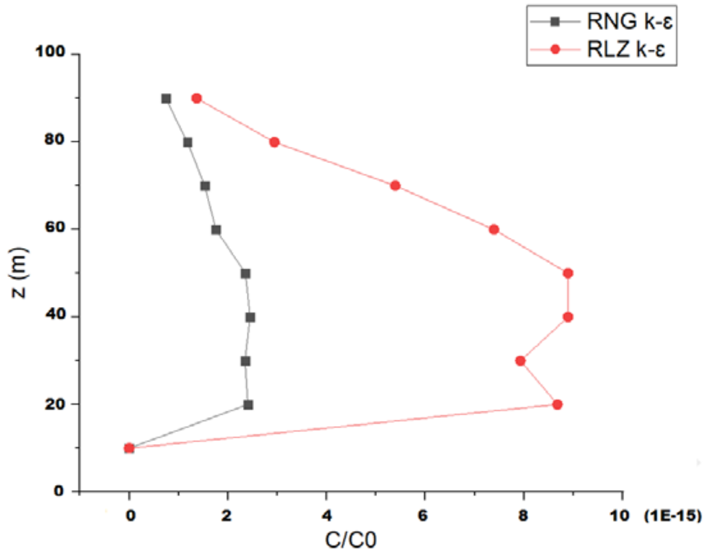

(c)

Figure 3.10 Mean concentration distribution of SF_6 at the: (a) windward wall of Block D in Residence W, (b) leeward of IT, and (c) central space of Residence W

Figure 3.11 illustrates the vertical flow patterns across the urban settings generated by the (a) RNG *k*-ε and (b) RLZ *k*-ε models. The recirculation flow predicted by the

RNG k-ε model was stronger than that predicted by the RLZ k-ε. Fig. 3.11a also demonstrates that vortices were fully developed in the wake regions of the IT, ZS, and Residence W buildings. Figure 3.11b shows that the turbulence vortex of the RLZ k-ε model at the wake region of IT was poorly developed, and the reattachment length of turbulence was significantly longer. The modelled lower wind speeds in the recirculating enclosure could explain the SF_6 accumulation in these areas.

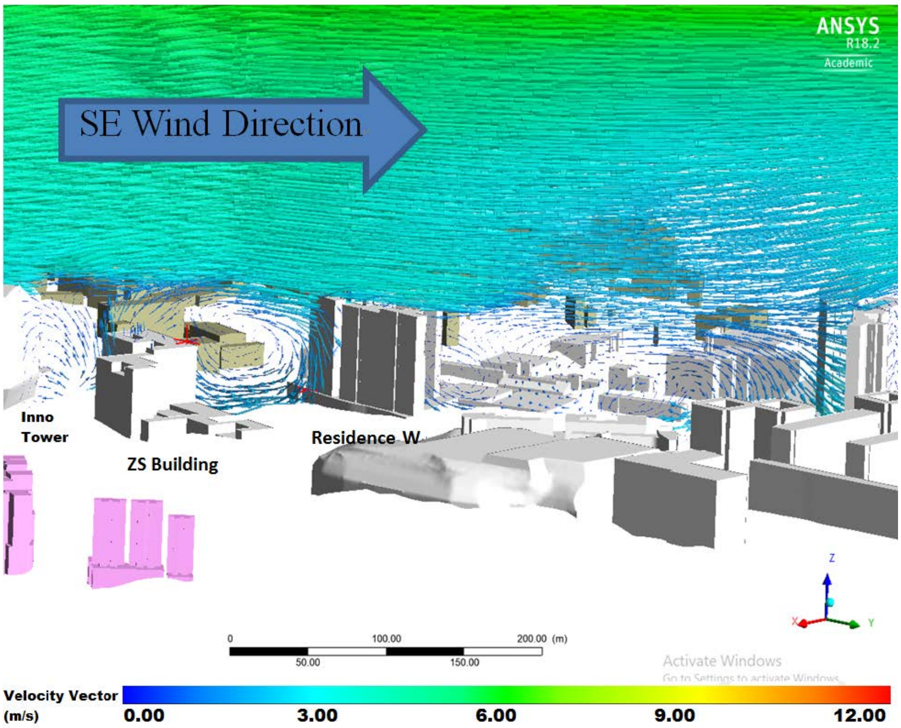

(a)

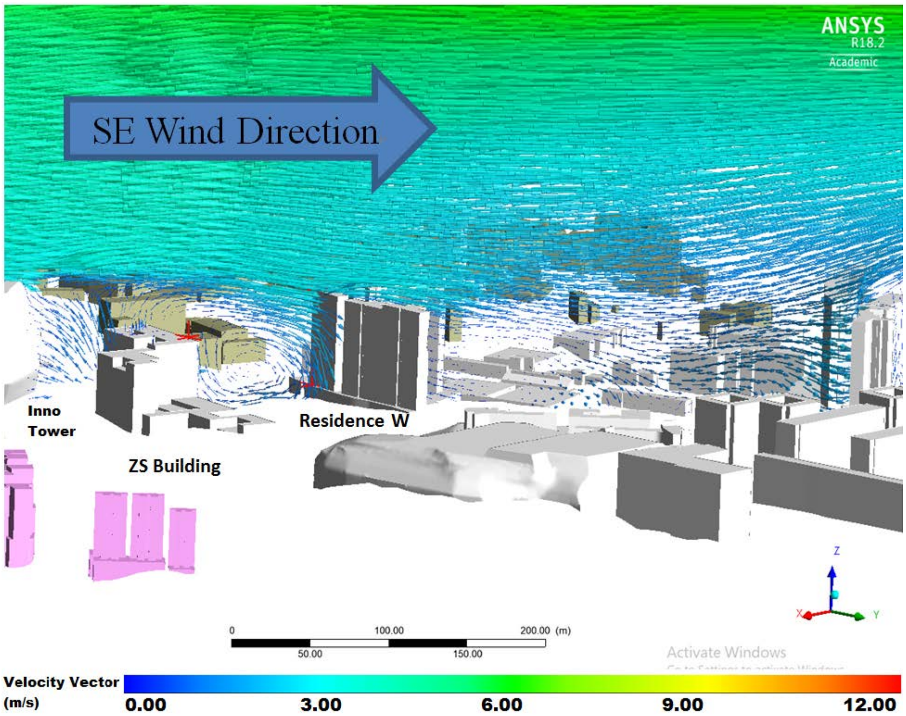

(b)

Figure 3.11 Flow patterns within the building groups by: (a) RNG k-ε and (b) RLZ k-ε models

Figure 3.12 shows the horizontal planes, and demonstrates that the air inside the central space of the Residence W building group was relatively stagnant. For most areas along the leeward wall facing the central space, airspeeds were ≤ ~0.5 $m \cdot s^{-1}$. Figure 3.12 also demonstrates that the RNG *k*-ε model had a wider horizontal range, with higher wind speeds in the wake region of Residence W facilitating the clearance of air contaminants from this region. The velocity contours also show that the RNG *k*-ε model described the changes in flow velocities of the central space and on the leeward side of the buildings in more detail. The RLZ *k*-ε model showed a longer trail of low speeds and reattachment length behind the building.

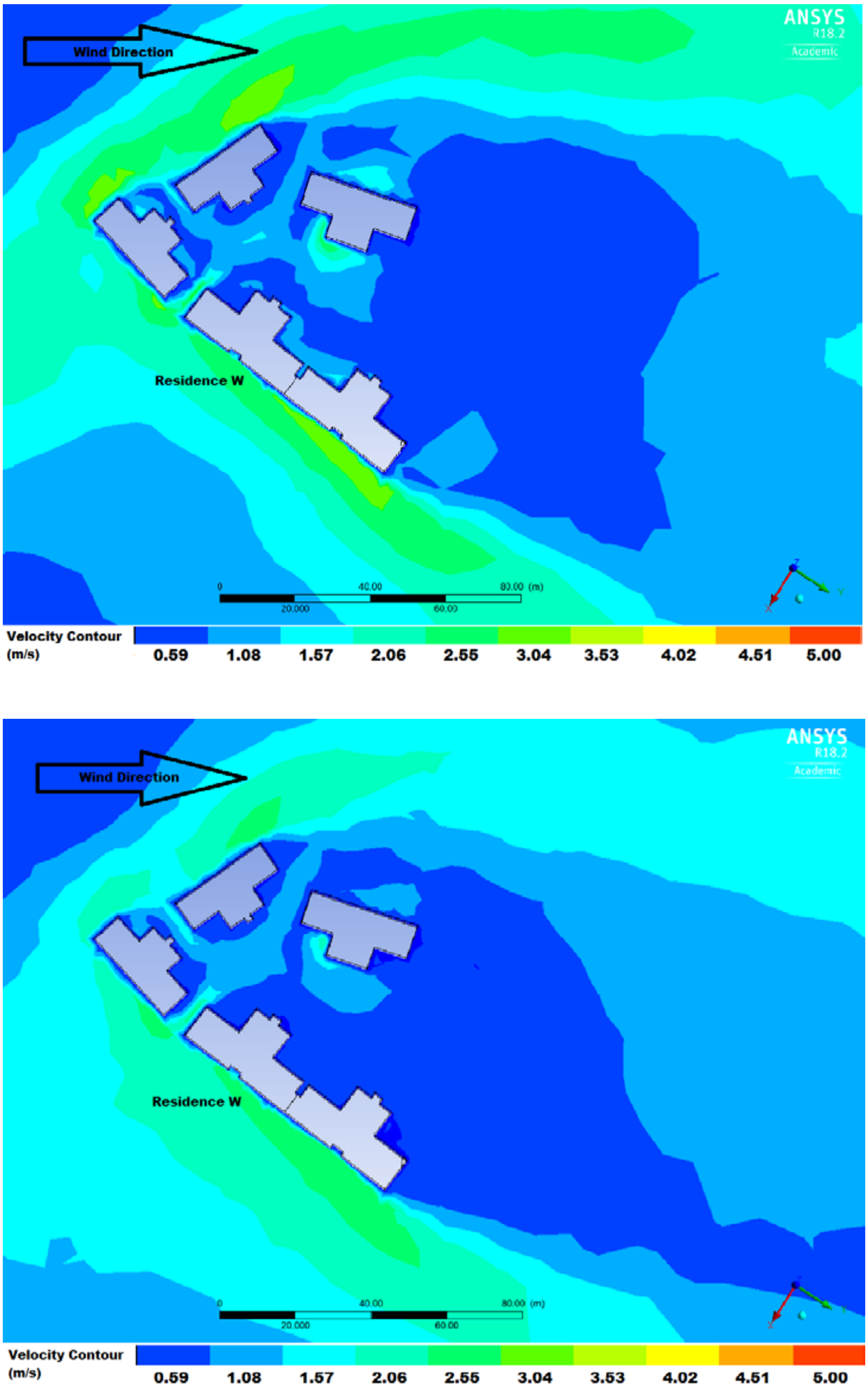

Figure 3.12 Horizontal flow patterns and wind velocities at the mid-level of Residence W by the (a) RNG, and (b) RLZ k-ε models

In terms of the mean velocities (U/U_o), Figure 3.13a shows that flow velocities on the windward wall of Block D increased from the podium level up to z = 40 m. The RLZ *k*-ε model showed a negative value in the lower vertical level, indicating the development of a reverse flow. The value gradually increased and peaked on the roof of the building. In contrast, the RNG *k*-ε model showed a slight decrease in velocity from z = 40–70 m. The velocity increased again at z = 80 m, and similarly reached its maximum on the roof. Notably, the predicted velocity ratio on the roof of the building was higher for the RNG than the RLZ *k*-ε model, and the velocity ratios obtained by the two models accounted for the differences in predicted tracer gas concentrations.

The negative values in the mid- to upper-levels of IT (Figure 3.13b), and the central space of Residence W (Figure 3.13c) indicate that there are reverse flows in the area and the accumulation of turbulence. Both models displayed similar results along the leeward walls of IT, where either prevailing wind direction placed IT upstream of the ZS Building, but the reverse flow indicated that IT could be affected by ZS Building emissions regardless of the wind direction. Both models showed similar reverse flow patterns in the central space of Residence W, favouring the accumulation of air pollutants.

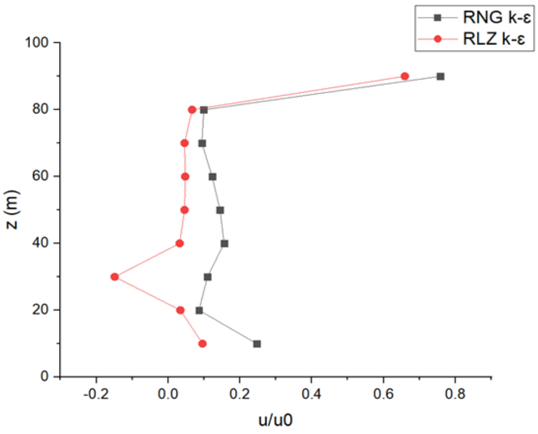
RNG k-ε
RLZ k-ε
100
80
60
40
20
0
z (m)
-0.2
0.0
0.2
0.4
0.6
0.8
u/u0

(a)

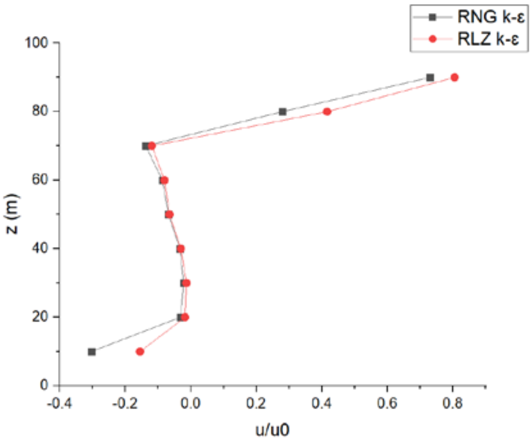
RNG k-ε
RLZ k-ε
100
80
60
40
20
0
z (m)
-0.4
-0.2
0.0
0.2
0.4
0.6
0.8
u/u0

(b)

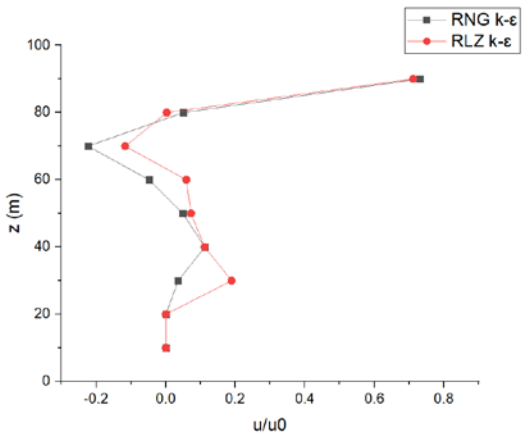
RNG k-ε
RLZ k-ε
100
80
60
40
20
0
z (m)
-0.2
0.0
0.2
0.4
0.6
0.8
u/u0

(c)

Figure 3.13 Mean wind-speed ratios on the: (a) windward wall of Block D in Residence W, (b) leeward side of IT, and (c) central space of Residence W; u refers to the mean wind-speed at specified vertical locations, and u_0 refers to the inflow velocity at the boundary.

3.3 Discussion

Some chemical parameters, namely NO_2, TVOC, and acetonitrile, exceeded the preestablished exposure levels in both operational and baseline air monitoring. From the results of annual NO_2 levels in urban areas of Hong Kong, such as Central/Western and Eastern districts, Sham Shui Po, Kwai Chung, and Tsuen Wan, it was observed that NO_2 pollution was widespread throughout the region, affecting the entire district across the year. Accordingly, excessive levels of NO_2 at Residence W and IT were likely caused by background contributions, and not stack emissions from the ZS Building.

Levels of TVOC exceeding the acute concentration criterion were also recorded on the roof of Block E when northeasterly winds were dominant. Therefore, it was suggested that these exceeding values were likely due to upstream background concentrations, rather than ZS Building emissions; however, the exceeding levels recorded on the podium-levels of Block B and E, as well as the Block E roof under southeasterly winds may have derived from the stack emissions. According to a

Korean study, VOC concentrations near laboratory buildings can be significantly higher than the background concentrations observed elsewhere (Park et al., 2014). Such results may be attributable to the large quantity of chemicals used during the normal laboratory operation, and the absence of air-purification devices in the exhaust systems of these buildings.

Only 7 (1.9%) high TVOC episodes (> 435 ppb) were recorded out of the 370 monitoring events. These occurred on the roof and mid-level of Block B; the mid-level of Block D; and on the roof, mid-level, and podium of Block E during predominantly southeasterly winds; however, four of these seven events occurred on the same day as high TVOC concentrations observed at IT, despite its upwind position. The flow pattern simulated by the RNG k-ε model showed recirculation and backflow at the wake regions of both IT and Residence W. This may have contributed to the elevated background TVOC levels observed across the whole district, particularly in the sampling locations of IT and building wakes in Residence W, regardless of wind direction.

For acetonitrile, the baseline monitoring results revealed that the average hourly concentrations ranging from 20 to 122 ppb for Residence W, and from 20 to 297 ppb for IT. Concentrations surpassing chronic exposure levels (> 36 ppb) were observed at Residence W under different wind directions. Among the 93 monitoring events with high acetonitrile levels, 34 (36.6%) were recorded under downwind conditions (i.e., SE, SSE, and S); of these, only four episodes coincided with the use of acetonitrile in the ZS Building laboratories, ultimately accounting for 4.3% of the excessive acetonitrile occurrences. The highest acetonitrile level (4,170 ppb) was recorded in the mid-level of Block B under northeasterly winds; thus, it is unlikely that this elevated level derived from the ZS building stack emissions. For IT, the exceedances occurred in the upwind and crosswind directions, maintaining no apparent association with the ZS Building gaseous emissions; although, the recirculation and backflow captured by the RNG k-ε model may explain the elevated readings. Elsewhere, it was observed that second hand cigarette smoke may also contribute significantly to increased atmospheric acetonitrile concentrations. Typical concentrations in a single puff of smoke ranges from 17 to 126 ppb (Abbott et al., 2003), and can reach up to 200 ppb (Jordan et al., 1995). Hence, nearby cigarette smoking to the sampling locations may have affected the overall sampling results.

The comparison between the results from the tracer gas study and the CFD simulations showed that the RNG k-ε model was more statistically accurate than the RLZ k-ε model, particularly for the sites nearest to the source, and along the windward side of the recipient building. This is consistent with findings from previous studies, which found that the RNG k-ε model could accurately predict the flow field in the street canyon (Ai and Mak, 2017); whereas the RLZ k-ε model underestimated turbulent fluctuations around buildings, and failed to fully capture the unsteady vortex-shedding motion in the wake regions (Tominaga and Stathopoulos, 2007). In the RNG k-ε model simulation (Figure 3.9b), the concentration transport along the upwind direction by advection was dominant, and well represented by the concentrations in the upwind region between the ZS Building and IT. In this case, the air pollutants from the stack would become trapped and accumulate in the recirculation zone (i.e., the central space of the buildings) of Residence W, and along the leeward of IT. This was also consistent with the findings from Lateb et al. (2013) and Tominaga and Stathopoulos (2013). The RNG k-ε model also accounted for the excursions of TVOC and acetonitrile in the air sampled from IT, even under predominantly southeasterly conditions, when IT was upwind of the stack emissions. In this case, the emissions may also impact the overall IAQ in IT since the fresh air intake of the MVAC system is located on the leeward wall facing the ZS Building.

From the simulation of tracer gas dispersion, it was found that the gradual increase of concentrations along the leeward wall of IT and Residence W could be attributed to the weakening of effluent momentum for contaminants and flow velocities. The wind speeds in these regions were generally lower, and the flow recirculation was favourable for the backflow and accumulation of air pollutants, thus explaining the measured SF_6 accumulation in these areas; however, to ascertain the effect of flow turbulence on the distribution of the tracer gas and air pollutants, scenarios with variable wind speeds and incident angles should be modelled.

3.4 Summary

The gaseous emissions from stacks connected to the fume hoods of chemical laboratories may have detrimental health effects on the local populace. In a densely populated city such as Hong Kong, exposure to various air pollutants of anthropogenic sources is inevitable, although point sources are difficult to identify. This chapter summarized the results of an emissions study using a comprehensive approach to identify the effects of gaseous emissions from a laboratory building situated within a short distance from a residential building group in Kowloon City, Hong Kong. Amongst the 15 chemicals analysed, only NO_2, acetonitrile, and TVOC exceeded the preestablished exposure levels. Upon examination of the test results, wind directions, and baseline monitoring concentrations, it was concluded that pre-existing environmental sources, such as building renovations in close proximity of air sampling locations, may have contributed to the excessive ait monitoring concentrations observed; however, the stack emissions from the ZS Building may have also been accountable, particularly for the elevated results observed at IT and mid-level locations in Residence

W. The tracer gas study results and CFD modelling further indicated that the gaseous emissions were heavily diluted above the roof of the ZS Building.

The flow simulation by the RNG k-ε model demonstrated that the recirculation vortices formed within the wake region or leeward side of the building further reduced airflow velocities, subsequently enhancing pollutant accumulation and deleteriously impacting air quality. Though IT is located upwind of the emission source, the simulated results from the RNG k-ε model also revealed the transport along the upwind direction by advection and recirculation still affecting his region. This could potentially account for the observed elevated concentrations of TVOC and acetonitrile at IT, regardless of wind direction. Accordingly, the installation of the fresh air intake on the leeward IT wall should be avoided due to the potential for elevated pollutant concentrations caused by the reverse flow in the building-wake region.

The validation process showed that the RNG k-ε model achieved relatively accurate predictions of pollutant dispersion in this actual urban environment compared with the RLZ k-ε model. Indeed, the RNG k-ε model yielded statistically acceptable results with respect to all tracer gas sampling data according to the FB (-0.5–0.5) and FAC2 (0.7–1.1) values. When the MG was explored, the model showed a relatively mild statistical deviation (1.5) from the experimental results, and tended to slightly over-estimate pollutant dilution on the rooftop.

Although RANS simulations are an economical approach to CFD simulations, the results from the present study showed that they may be insufficient to achieve statistically sound results with respect to the field measurement data collected across an actual urban environment; thus, a careful interpretation of data generated by RANS approaches is needed, and should be used and interpreted in conjunction with air monitoring and tracer gas assessment data as a comprehensive approach to investigating the impacts of stack emissions on urban settings. Other transient models, such as large eddy simulation (LES) and detached eddy simulation (DES), could also be employed to yield more accurate results; however, much higher computational costs would be incurred.

CHAPTER 4 Variable Wind Directions and the Ventilation of Surrounding Areas for Two Generic Building Configurations in Hong Kong

This chapter investigates the effects of incident wind angles on wind velocity distributions in the wakes of two generic building configurations in Hong Kong, namely, "T”- and "+"-shaped, as well as the air pressure distributions along their leeward walls via computational fluid dynamics (CFD) simulations. Results showed that when the wind approached laterally (90°, versus direct wind—0°), the downwind length and maximum bilateral width of the low-wind velocity zone in the wake of “T”-shaped building decreased by 11.5% and 37.9%, respectively. When the incident wind was oblique (45°, versus direct), the length and width of this low-wind velocity zone in the wake of “+”-shaped building decreased by 15.0% and 30.9%, respectively. Furthermore, results showed that the air pressure on the leeward walls of the “T”- and “+”-shaped buildings gradually decreased with building height. The resulting low-wind conditions on the upper floors of the buildings reduced the fresh air intake of their leeward units utilizing natural ventilation, particularly with direct approaching winds. Thus, the appropriate selection of building configurations and their orientations allows for optimizing wind use to enhance natural ventilation in indoor and urban environments.

4.1 Methodology

4.1.1 CFD turbulence models

In situ measurements of air quality are a straightforward method for identifying the pollutant concentrations and dispersion across a defined environment; however, perform such analyses can be expensive over longer periods, and are thus not always feasible (Lee and Mak, 2019). Numerical CFD methods, which provide complete field data without limitations on the similarity requirements, offer an alternative way to examine air pollutant dispersion around a building (Dai et al., 2018b). Research has shown that CFD methods can accurately predict air velocities around single, double, and multiple building configurations in a detailed quantitative fashion (An et al., 2013). Furthermore, experimental data, such as that from certain wind tunnel studies on pollutant dispersion, can be used as an efficient method of model verification.

Xia et al. (2014) and Blocken (2015) stated that Reynolds-averaged Navier-Stokes (RANS) approaches, commonly used for solving turbulence problems, are less computationally expensive than other transient state methods because they focus on the mean flow properties of turbulence. Among different RANS approaches, the realizable

(RLZ) k-ε, and renormalization group (RNG) k-ε models are suitable for simulating urban wind flow (Lee and Mak, 2019; Liu and Niu, 2016). An et al. (2013) found that the RLZ k-ε model predicts wind velocities in high-wind regions well, but tends to underestimate airflow in the low-wind areas. Alternatively, the RNG k-ε model consistently provides more accurate results when compared with wind tunnel and pollutant concentration field data (Lateb et al., 2013; Tien and Calautit, 2019; Tominaga and Stathopoulos, 2009). It provides satisfactory results when used to study wind-driven, single-sided natural ventilation (Ai and Mak, 2014b), and performs better when resolving rapid strain and streamline curvatures. Its flexibility stems from the inclusion of an additional strain-dependent term (R_ε; Du et al., 2019), as shown in Equation (4.1):

$$R_\varepsilon = \frac{C_\mu \rho \eta^3 (1 - \frac{\eta}{\eta_0})}{1 + \beta \eta^3} \cdot \frac{\varepsilon^2}{k} \tag{4.1}$$

where C_μ, η_0, and β are constants (C_μ = 0.09, η_0 = 4.38, β = 0.012), ρ is the fluid density, k is the turbulent kinetic energy, ε is the turbulent viscous dissipation rate, and $\eta \equiv Sk/\varepsilon$ where S is the strain rate scale. According to ANSYS (ANSYS FLUENT 14.5, 2012), this revised feature of the RNG k-ε model allows it to effectively predict flows with low Reynolds (Re) numbers in near-wall regions. In view of their availability, consistency, and suitability, both RLZ and RNG k-ε models were selected for analysis here, and validated using CEDVAL wind tunnel data.

4.1.2 Wind tunnel experiment

The wind tunnel tests from the CEDVAL project, employed for model validation here, were developed by the Meteorological Institute at the University of Hamburg Environmental Wind Tunnel Laboratory (Figure 4.1; Leitl and Schatzmann, 1998). In the present study, models on a 1:200 scale (unit volume with side H = 0.125 m) were constructed for direct comparison with the CEDVAL wind tunnel project (test parameters are listed in Table 4.1). The similarity requirements between the wind tunnel and CFD models were strictly tested. The Re number was > 3.7×10^4, satisfying the minimum requirement of 1.5×10^4 (i.e., Re number independence was attained, and the similarity requirements were fulfilled; van Hooff et al., 2017).

Table 4.1 Parameters of the scaled model (A1-4; Leitl and Schatzmann, 1998)

Parameter	Symbol	Value
Building height	H	0.125 m
Reynolds number	Re	37,250
Power law	$\acute{\alpha}$	0.22
Reference velocity	U_{ref}	6 m·s^{-1}
Reference height	H_{ref}	0.5 m

Friction velocity	$u*$	$0.35\ m \cdot s^{-1}$
Roughness length	z_0	0.0004 m
Offset height	d	0.00 m
Turbulence length	L	0.32 m

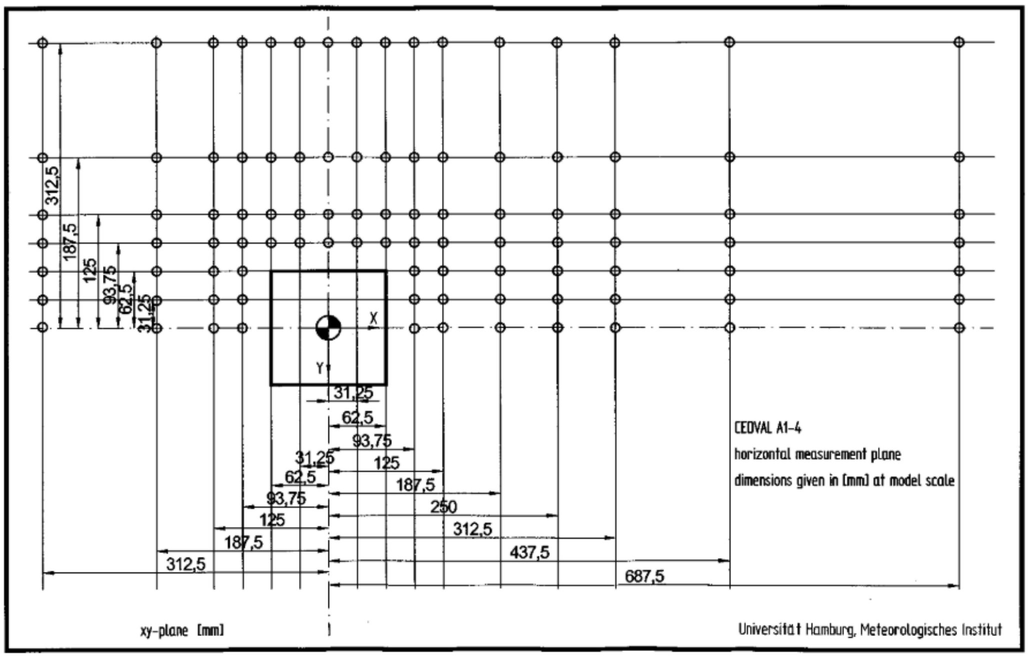

Figure 4.1. Experimental design sketch of the wind tunnel with measurement points (Leitl and Schatzmann, 1998).

4.1.3 Boundary conditions

An inhomogeneous atmospheric boundary layer (ABL), and near-wall treatments can significantly affect the simulated results of atmospheric flow and pollutant dispersion (Ai and Mak, 2013). Accordingly, it was essential to develop a homogeneous ABL before conducting numerical studies.

Richards and Hoxey (1993) suggested the following inlet boundary condition for a fully developed, horizontally homogeneous, two-dimensional ABL flow (Richards and Hoxey, 1993):

$$U = \frac{u^*}{K} ln\left(\frac{z + z_0}{z_0}\right) \tag{4.2}$$

To rectify the impracticality of the constant inlet profile for turbulence kinetic energy suggested by the above research, and improve upon the consistency of the horizontal boundary layer, turbulent kinetic energy (k) and turbulent viscous dissipation rate (ε) were defined as follows to reach equilibrium between turbulence dissipation and production (Leitl and Schatzmann, 1998):

$$k = \sqrt{C_1 \; ln(z + z_0) + C_2} \;, \tag{4.3}$$

$$\varepsilon = \frac{u^* \sqrt{C_\mu}}{K(z + z_0)} \sqrt{C_1 ln(z + z_0) + C_2} \tag{4.4}$$

The inlet boundary conditions defined on the boundaries of the computational domain are determined by the profiles of the mean wind speed (U), k, and ε, as indicated in Equations (4.2), (4.3), and (4.4), respectively. When incorporated into an appropriate near-wall treatment on the domain ground, this set of inlet boundary conditions allows one to obtain a homogeneous ABL (Ai and Mak, 2013; Gorlé et al., 2010). In Equations (4.3) and (4.4), z is 0.035m (equal to 0.28 H in the model scale used in the determination of inlet boundary conditions (Ai and Mak, 2013; Liu et al., 2019b; Yu and Thé, 2017)); z_0 is the roughness length (0.0004 m); u^* is the frictional velocity (0.35 $m \cdot s^{-1}$); C_1 and C_2 are constants equal to 0.025 and 0.41, respectively; C_μ is a constant equal to 0.09; and K is the Von Karman constant, equal to 0.4187 (Borrego et al., 2006) .

The downstream vertical boundary was modelled as an outflow, and the sky was treated as a mirror plane. An enhanced-wall function was adopted for the surfaces of the building block, where the computational domain was non-slip. The mesh near the building and ground surfaces was refined to replicate the physical characteristics of the flow. To accurately simulate the approaching ABL flow in the computational domain, horizontal homogeneity was required, i.e., the vertical flow profiles prescribed at the inlet needed to be preserved on the domain before reaching the buildings (Blocken et al., 2007).

The low-Reynolds number regions below the first grids and the effects on the entire wall-bounded flow could be ignored, as the standard wall functions directly link the walls and near-wall logarithmic layer with a series of semi-empirical formulae (Ai and

Mak, 2013). In the present study, an enhanced wall treatment integrated the flow variables down to the walls, and was adopted for near-wall modelling as it could resolve the viscous sublayer and compute the wall shear stress from a local velocity gradient normal to the wall. Moreover, it provided a more accurate prediction of the velocity distributions in the recirculation zones near the windward edges and building wakes (Lateb et al., 2013). In this study, a relatively fine mesh was imposed in the wall-normal direction (i.e., a small y^+ value between 2 and 5) to show the suitability of the selected grid for the enhanced wall treatment. In the equilibrium of the turbulent boundary layers, y* was approximately equal to y^+ ($y^+ = \rho u y_p / \mu_t$) in equilibrium of turbulent boundary layers (Ai and Mak, 2013). The CFD program, ANSYS Fluent, used in this study employs y* exclusively, as the calculation of y^+ requires an iteration for every boundary cell in the mesh, and is thus computationally expensive.

4.1.4 Computational domain and grid

To ensure that the wind flow was fully developed with minimum blockage effects, the upstream, downstream, lateral, and height components of the computational domain were set as 5H, 15H, 5H, and 5H, respectively (Figure 4.2), based on the requirements of the CFD practice guidelines (Franke et al., 2007). The blockage ratio was ~2.7% and in compliance with the European Cooperation in Science and Technology (COST)

Action 732 (Franke et al., 2007). The entire domain was constructed using structured hexahedral grids, with a grid expansion ratio < 1.2 in both the horizontal and vertical directions (Tominaga et al., 2008). The pressure and momentum equations were coupled using the Semi-Implicit Method for Pressure-Linked Equations (SIMPLE) algorithm, and a second-order upwind scheme was used for discretization. The scaled residuals in the simulation were all set to 10^{-5}, and convergence was obtained at this level.

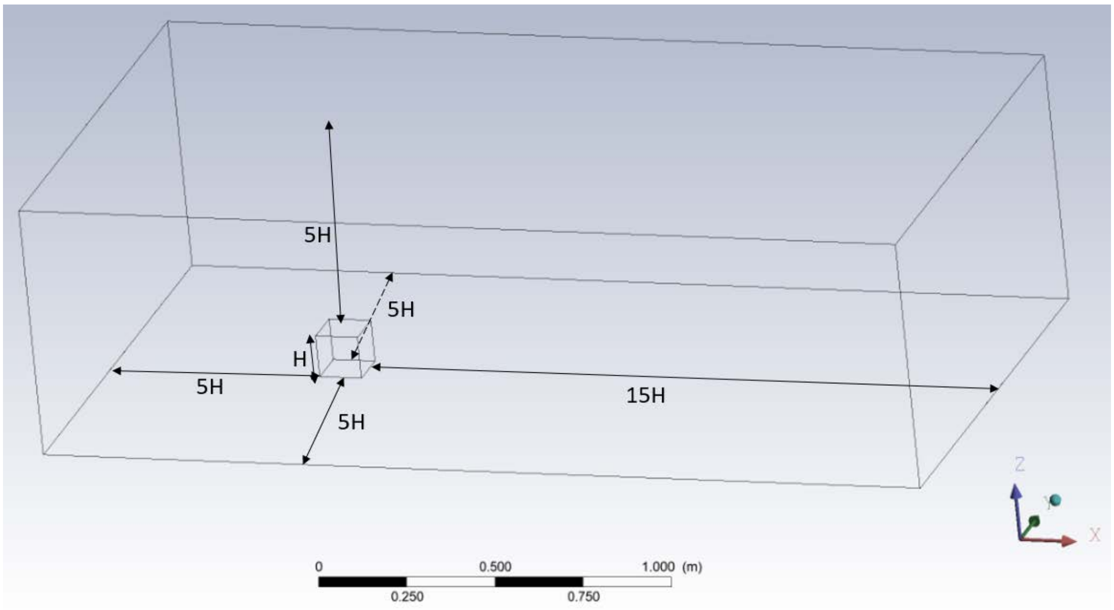

Figure 4.2 Computational domain.

It is important to perform a grid-sensitivity analysis to reduce the discretization errors and computational time (Montazeri and Blocken, 2013). In this study, this was performed based on three mesh systems with minimum grid sizes of 0.0005, 0.0002, and 0.00005 m, so mesh numbers of 1.443 million (coarse), 4.018 million (medium) and 6.079 million (fine), respectively, were constructed. The simulation results from the three systems were compared to examine the independence of the numerical solution as it correlates to grid size.

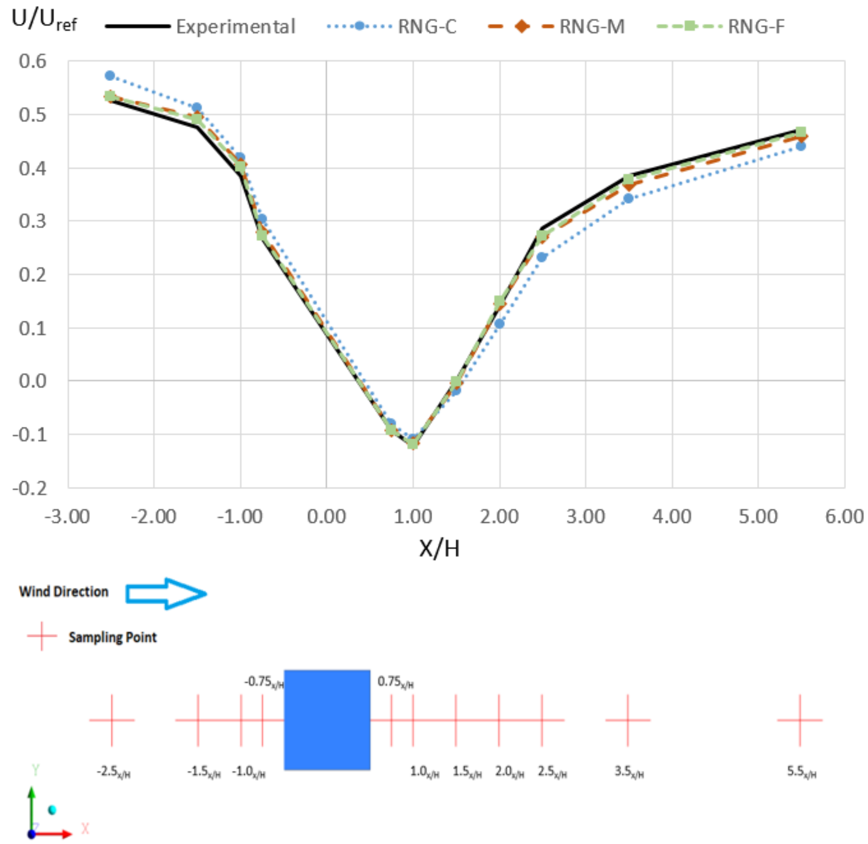

(a)

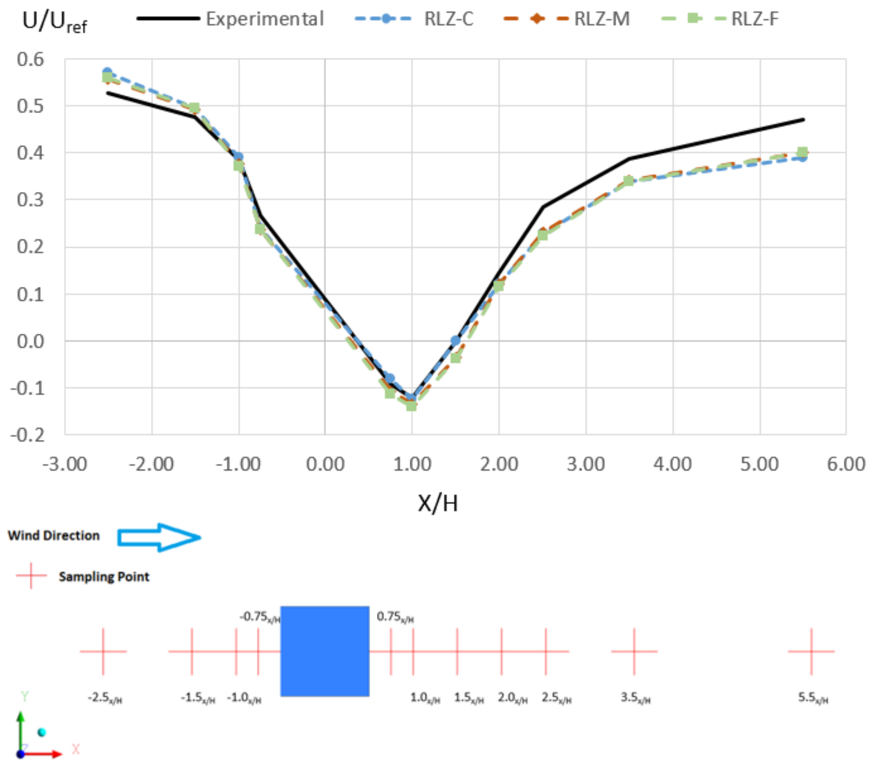

(b)

Figure 4.3 Comparisons of wind tunnel data with the simulated results from the (a) RNG and (b) RLZ k-ε models for three mesh systems: coarse (C), medium (M), and fine (F).

Comparisons of the dimensionless velocity ratio (U/U_{ref}) between the experimental wind tunnel data and the simulated results of the RNG *k-ε* (Figure 4.3a) and RLZ *k-ε* (Figure 4.3b) models along the horizontal plane at Z = 0.4H and the midline of the building model (Y = 0H) were made. The results generated from the medium (M) and fine (F) mesh systems used in both models were consistent; however, their differences from the coarse (C) mesh system were quite obvious, particularly in the far windward and leeward regions. Apart from grid sensitivity, Figure 4.3(b) presents that the RLZ *k-ε* model tends to overestimate the velocity ratio on the windward side, and underestimate it on the leeward side of the building. The simulation results of the RLZ *k-ε* model also show more significant deviations of the velocity ratio in the building wake, starting from X = 2.5H–5.5H. Table 4.2 shows that the RNG k-ε model, in general, produced a stronger statistical performance (correlation coefficients: 0.988–0.999) when compared with the RLZ k-ε model (0.988–0.992). Further, the geometric median biases (MGs) of the results from the RNG k-ε model were closer to 1. The similar results between medium and fine mesh systems, and their superior performance over the coarse mesh system, informed the decision to use medium mesh system with a minimum grid size of 0.0002 m for the CFD simulation.

Table 4.2 Statistical test results of (a) RNG and (b) RLZ k-ε models for the three mesh systems: coarse (C), medium (M), and fine (F).

(a)

Distance (X/H)	Experimental	U/Uref RNG-C	RNG-M	RNG-F
-2.50	0.526	0.573	0.533	0.533
-1.50	0.477	0.513	0.495	0.491
-1.00	0.385	0.419	0.407	0.401
-0.75	0.267	0.303	0.279	0.271
0.75	-0.092	-0.081	-0.092	-0.092
1.00	-0.122	-0.110	-0.117	-0.120
1.50	0.001	-0.019	-0.004	-0.001
2.00	0.144	0.108	0.146	0.149
2.50	0.285	0.231	0.270	0.273
3.50	0.386	0.341	0.368	0.379
5.50	0.471	0.440	0.459	0.468
	Correlation Coefficient	0.988	0.998	0.999
	Geometric mean biases (MG)	1.0	1.0	1.0

(b)

Distance (X/H)	Experimental	U/U_{ref} RLZ-C	RLZ-M	RLZ-F
-2.50	0.526	0.571	0.557	0.560
-1.50	0.477	0.495	0.491	0.494
-1.00	0.385	0.390	0.376	0.372
-0.75	0.267	0.239	0.238	0.236
0.75	-0.092	-0.081	-0.106	-0.113
1.00	-0.122	-0.123	-0.135	-0.140
1.50	0.001	0.000	-0.036	-0.037
2.00	0.144	0.121	0.122	0.114
2.50	0.285	0.229	0.231	0.222
3.50	0.386	0.339	0.340	0.338
5.50	0.471	0.390	0.399	0.401
	Correlation Coefficient	0.988	0.992	0.992
	Geometric mean biases (MG)	1.1	1.1	1.1

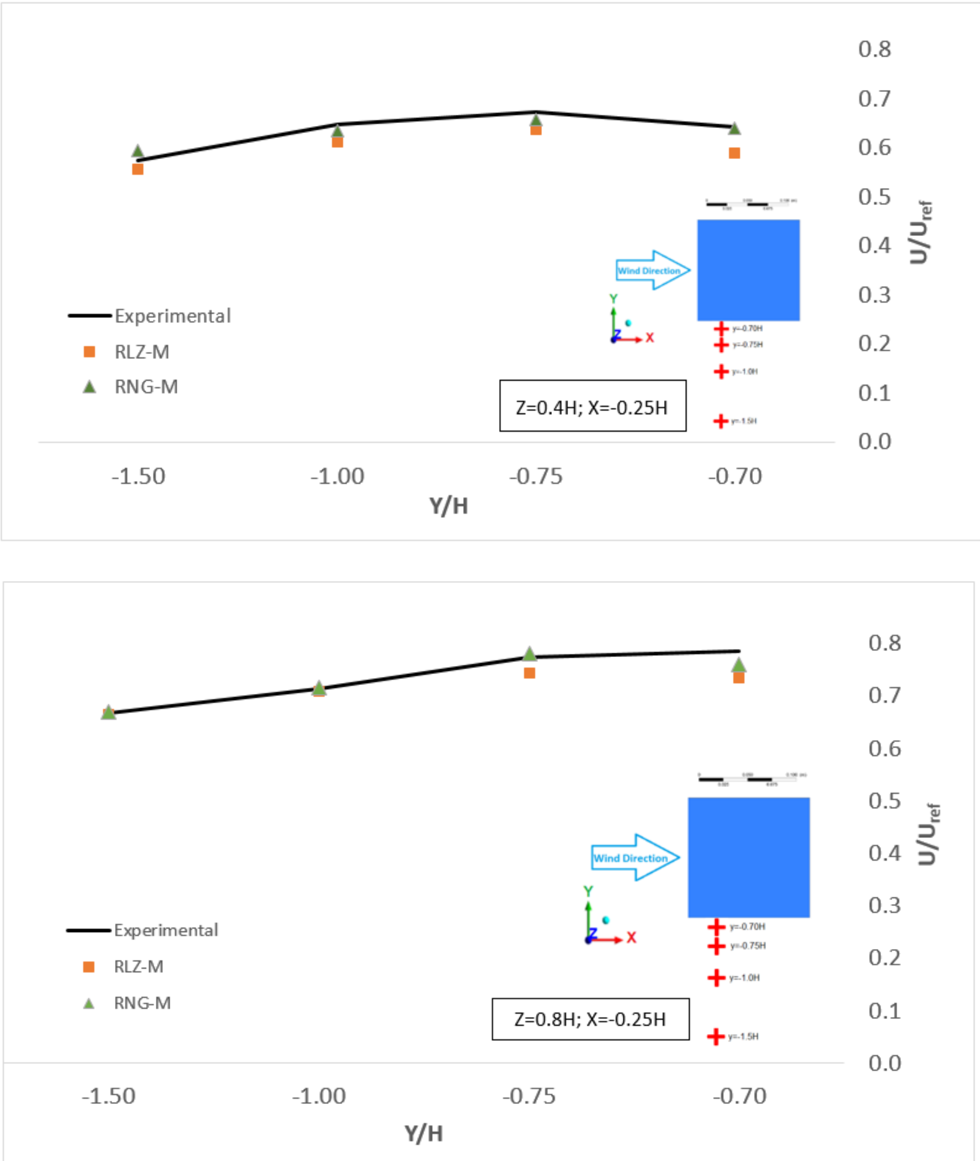

(a)

(b)

Figure 4.4 Comparison of the wind tunnel data with the simulated RNG and RLZ k-ε model results for the medium mesh system at two different horizontal levels: (a) Z = 0.4H, (b) Z = 0.8H. +'s in the insets indicate the measurement points along the y-axis direction.

Figure 4.4 illustrates the changes in velocity ratio at different locations along the y-axis direction of the model for two horizontal plains, $Z = 0.4H$ and $0.8H$. It was found that both RNG and RLZ k-ε models show good agreement with the wind tunnel data, save for the sampling location near the lateral wall (Y = -0.7H) for the RLZ k-ε model. Statistically, the RNG k-ε model performed better, with correlation coefficients ranging from 0.965 to 0.998, and MGs ranging from 1.003 to 1.005.

Comparisons of wind tunnel and simulation data at different vertical distances (expressed in Z/H) near the windward (Figure 4.5a), leeward (Figure 4.5b), and lateral (Figure 4.5c) walls of the building were also conducted. On the windward side, the MGs between the wind tunnel data and those from the RLZ and RNG k-ε models were 1.073 and 1.035, respectively (Figure 4.5a); whereas the course leeward side MGs were 1.145 and 1.098, respectively (Figure 4.5b). The simulated and experimental wind velocity ratios on the lateral wall were in good agreement (Figure 4.5c), and the corresponding MGs between the experimental data and those from RLZ and RNG k-ε models were 1.100 and 1.069, respectively; however, the RLZ k-ε model underestimated the horizontal wind velocities at higher vertical levels (i.e., Z/H = 0.6–1.0) compared to RNG.

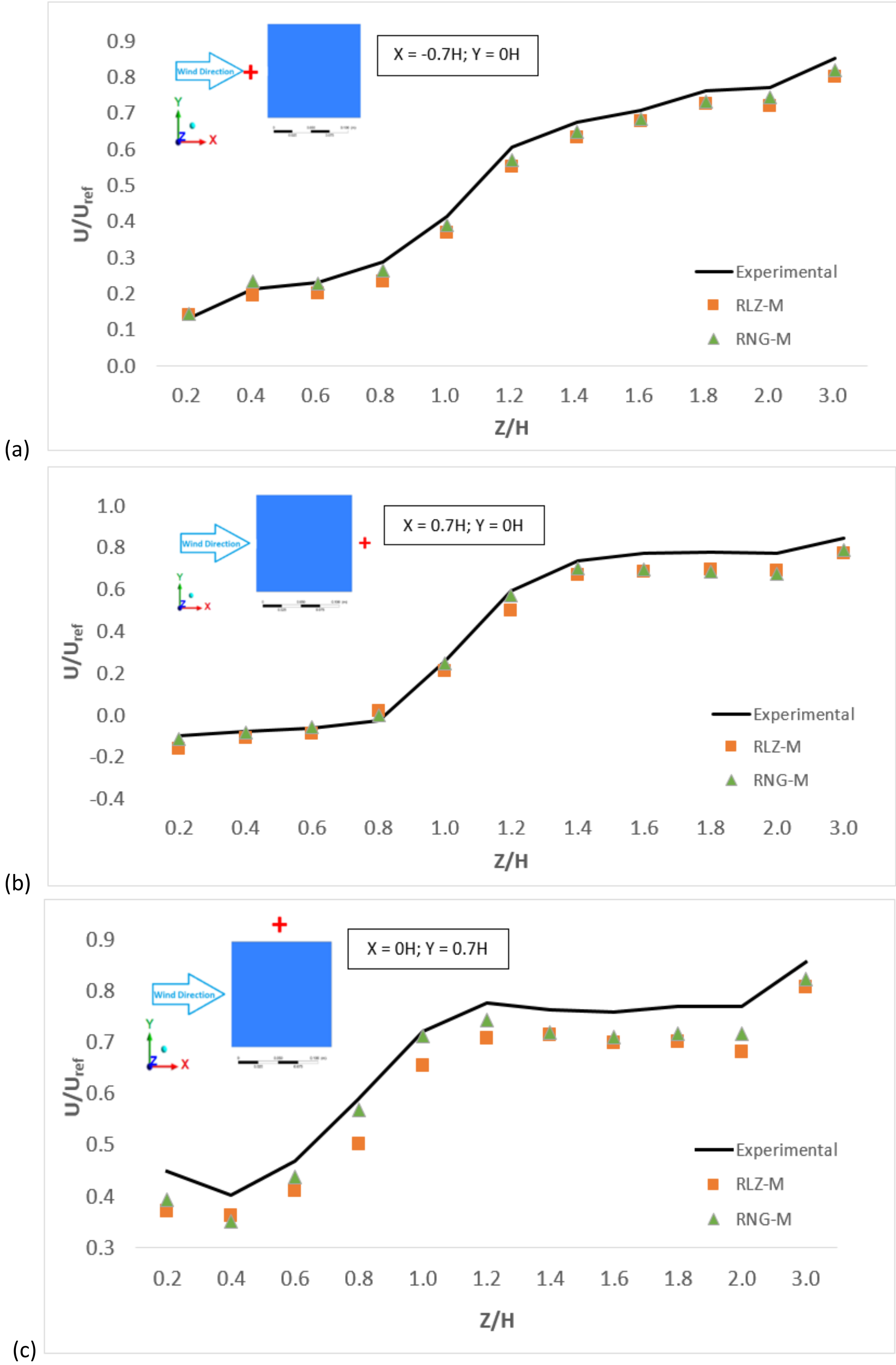

Figure 4.5 Comparison of the wind tunnel data with the simulated RLZ and RNG k-ε model results on

the (a) windward, (b) leeward, and (c) lateral walls of the building block (blue). + in the inset indicate the measurement point location. The building height fraction *H* is represented on the x-axis.

After considering the overall performance of the two k-ε models, the RNG k-ε model with a medium mesh system was adopted in the current study, as it can most efficiently provide sufficient accuracy for predicting the wind flow around an isolated building.

4.1.5 *Building configurations*

To study the effects of building configurations and incident wind angles on the airflow patterns around the building, a normal building configuration (i.e., “-”-shaped; Figure 4.6a) building, was constructed and used to compare with the two other generic building configurations, "T"-shaped (Figure 4.6b) and "+"-shaped (Figure 4.6c). The effects of directly approaching wind (θ = 0°), oblique (θ = 45°), oblique opposing (θ = 135°), lateral (θ = 90°), and opposing (θ = 180°) wind directions (Figure 4.6a–c) were investigated. The front and back sections of the buildings were also labelled for ease of reference and identification. The validated mesh, inflow wind profile, computational domain size, turbulence model, and numerical methods were used in this study for simulating the wind flow around these buildings.

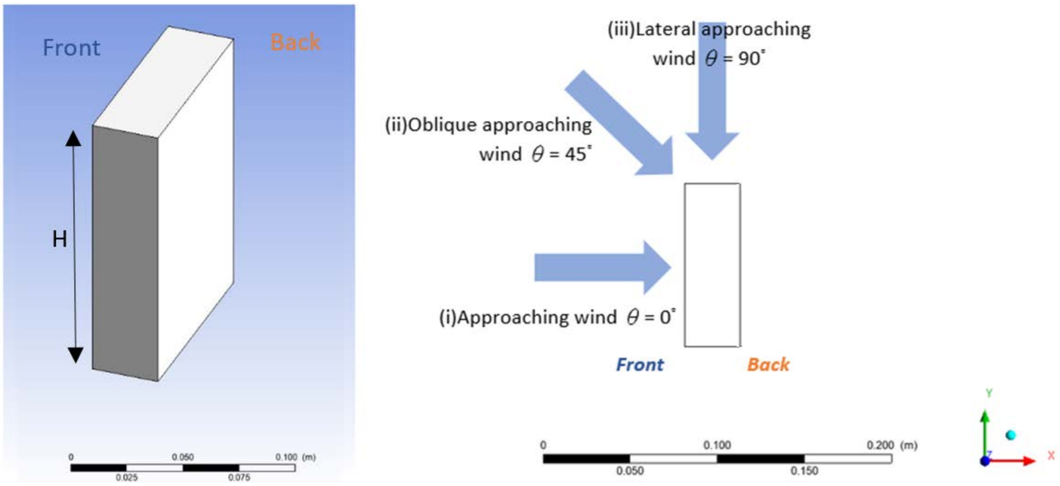
Front
Back
H
(iii)Lateral approaching wind θ = 90°
(ii)Oblique approaching wind θ = 45°
(i)Approaching wind θ = 0°
Front
Back

(a)

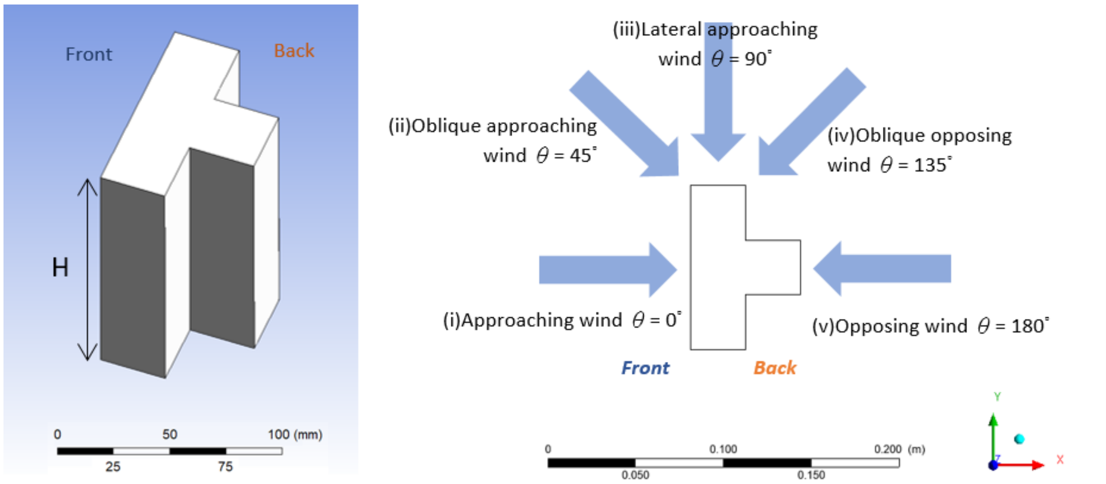
Front
Back
H
0
50
100 (mm)
25
75
(iii)Lateral approaching wind θ = 90°
(ii)Oblique approaching wind θ = 45°
(iv)Oblique opposing wind θ = 135°
(i)Approaching wind θ = 0°
(v)Opposing wind θ = 180°
Front
Back
0
0.100
0.200 (m)
0.050
0.150

(b)

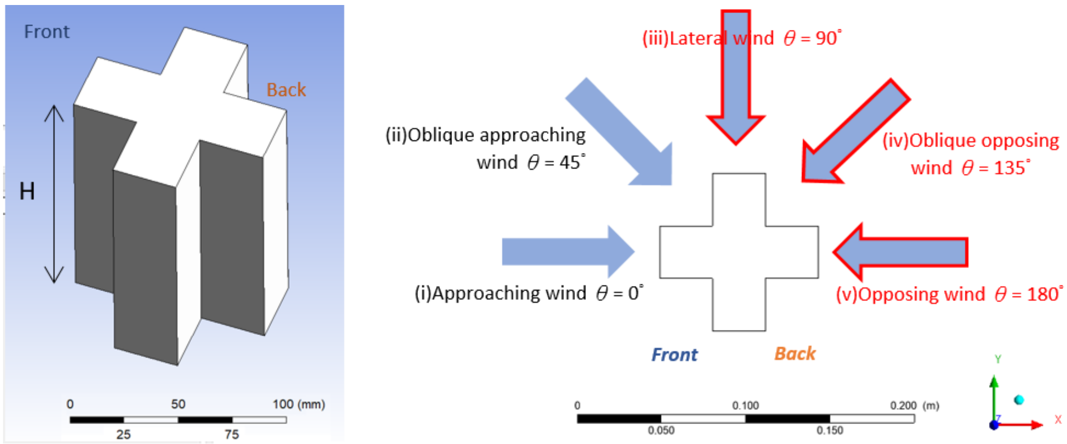
Front
Back
H
0
50
100 (mm)
25
75
(iii)Lateral wind θ = 90°
(ii)Oblique approaching wind θ = 45°
(iv)Oblique opposing wind θ = 135°
(i)Approaching wind θ = 0°
(v)Opposing wind θ = 180°
Front
Back

(c)

Figure 4.6 Building configurations and incident wind directions for: (a) normal "-"-shaped, (b) "T"-shaped, and (c) "+"-shaped buildings. H = 125 mm. (c) Wind angles for (iii) and (v) are equivalent to (i), as are the wind angles shown in (ii) and (iv).

Because the wind flow in zones where the mean wind velocity ratio was < 0.25 was deemed uncomfortable and unfavourable for pedestrian activity, the distributions of the mean wind velocity ratios at the pedestrian level (1.75 m at equivalent full scale) in the building wakes were calculated. Areas with a mean wind velocity ratio < 0.25 were regarded as low-wind velocity zones. Moreover, because units and windows along the leeward wall are considered less favourable for fresh air intake and natural ventilation, the distributions of the dimensionless pressure coefficients (C_p) on the leeward surfaces were calculated according to Equation (4.5)

$$C_P = (P - P_0)/(0.5\rho U_{\mathrm{ref}}^2) \tag{4.5}$$

where P is the static pressure, P_0 is the reference pressure, ρ is the density, and U_{ref} is the reference u-velocity.

4.2 Results and discussion

4.2.1 Wind direction and flow patterns around normal "-"-shaped building

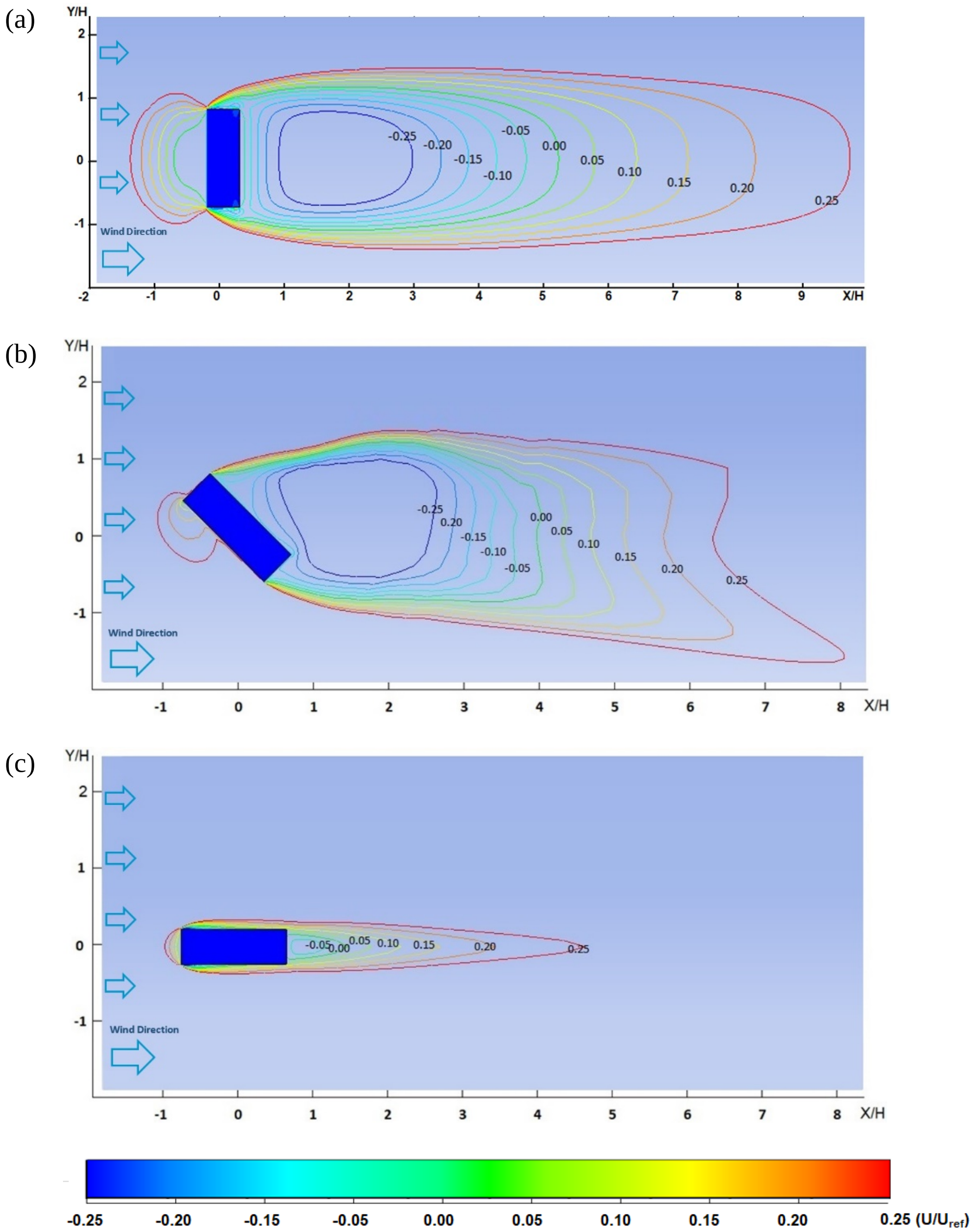

Figure 4.7 Distributions of U/U_{ref} in the horizontal plane at pedestrian height (1.75 m) of the "-"-shaped building, for: (a) direct (θ = 0°); (b) oblique (θ = 45°), and (c) lateral approaching winds (θ = 90°).

The general features of the wind velocity ratio (U/U_{ref}) distribution around the normal, "-"-shape building configuration at the pedestrian level (1.75 m) and under different incident wind directions are shown in Figure 4.7. The three different wind directions—direct (0°), oblique (45°), and lateral (90°)—displayed different velocity distribution patterns and low-wind velocity zone developments in the building wake.

The low-wind velocity zone ($U/U_{ref} < 0.25$ where $U_{ref} = 6\ m \cdot s^{-1}$) in the building wake of the lateral wind (90°) was the smallest (Figure 4.7c). This zone extended horizontally to 4.75*H* downwind (x-axis direction), and had a maximum bilateral width < 0.7*H* (y-axis). Accordingly, the wind velocities in the wake of lateral wind conditions would be the highest among all wind directions; however, when the approaching wind was direct (0°), the low-wind velocity zone reached the maximum distance compared to the other directions (9.75*H*, x-axis), and had a maximum bilateral width of 3*H* (y-axis) in the building wake. The downwind extension and maximum bilateral width of the low-wind velocity zone under the lateral wind condition (90°) were 329% and 105%, respectively, less than with the direct approaching wind (0°), which represented the worst-case scenario. Thus, the building wake airflow under a direct approaching wind (0°) was relatively stagnant, and the resulting wind environment in these areas may not be favourable for pedestrian activity.

In the oblique wind condition (45°), a smaller low-wind velocity zone was recorded, extending to 8*H* (x-axis), and a bilateral width of 4*H* (y-axis). The gross area of the resulting low-wind velocity zone in the building wake was larger than in the case of lateral wind (90°), and similar to the direct approaching wind (0°) scenario. As such, the wind environment in the building wake under the oblique wind direction remained less favourable for pedestrian activity.

4.2.2 Wind direction and flow patterns around "T"-shaped building

(a)

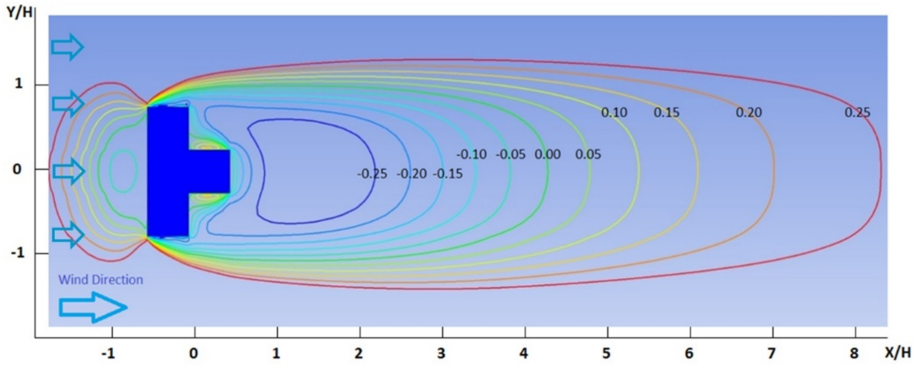

(b)

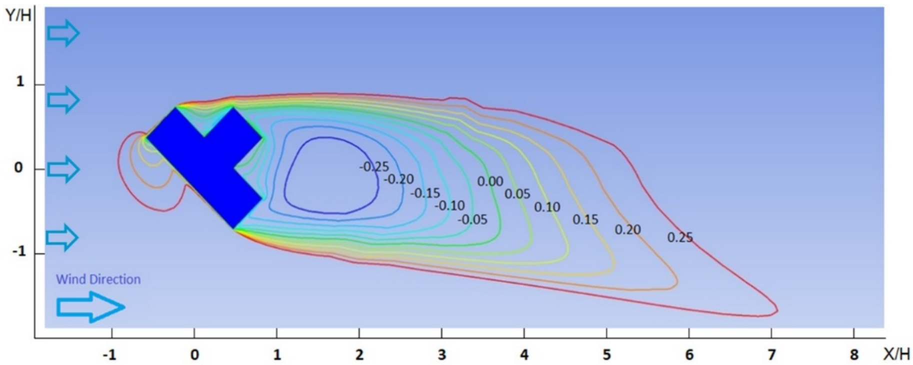

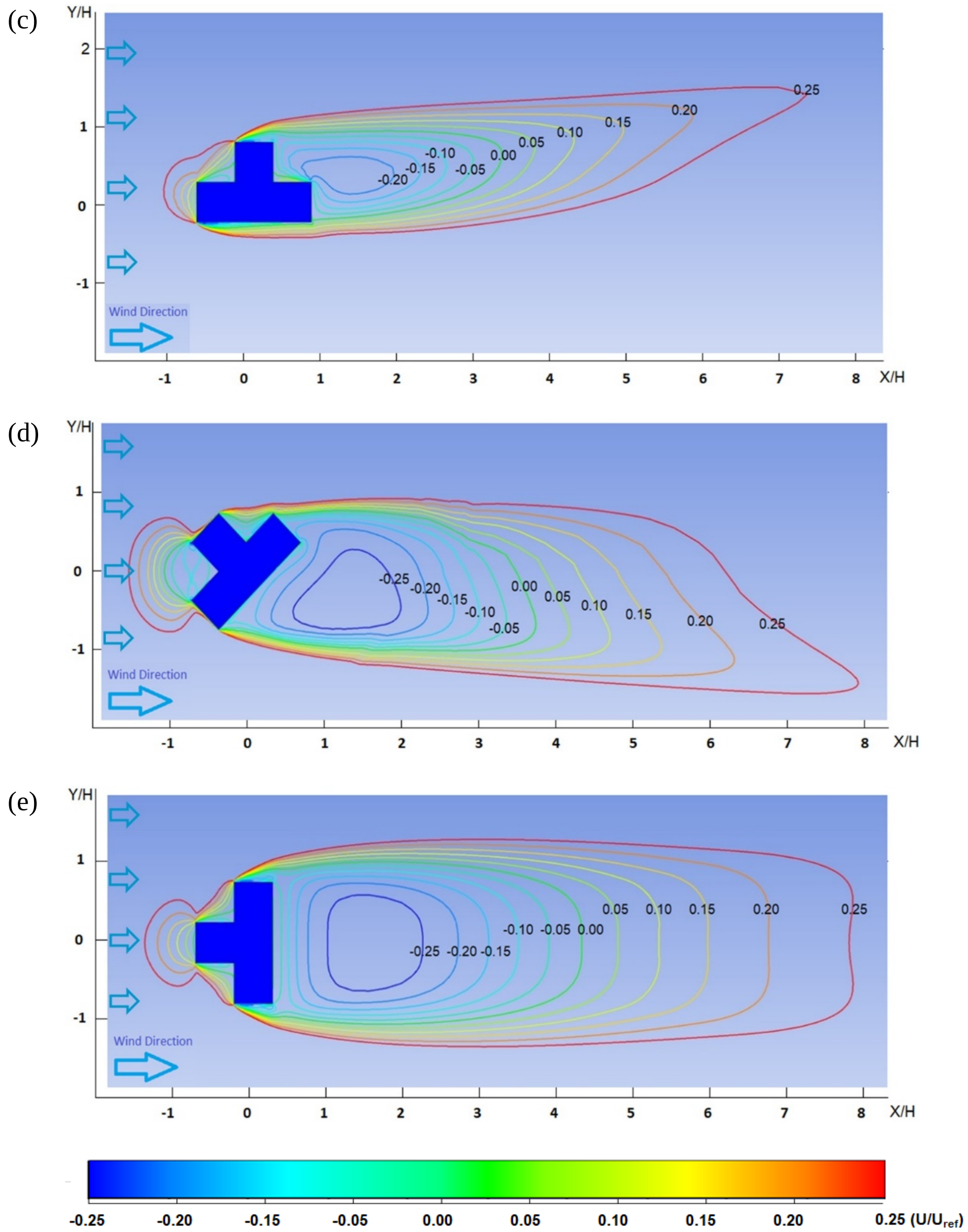

Figure 4.8 Distributions of U/U_{ref} in the horizontal plane at pedestrian height (1.75 m) of the "T"-shaped building, for: (a) direct (θ = 0°); (b) oblique (θ = 45°), and (c) lateral (θ = 90°), (d) oblique opposing (θ = 135°), and (e) opposing winds (θ = 180°).

Figure 4.8 shows the general features of the wind velocity ratio (U/U_{ref}) distribution around the "T"-shaped building at the pedestrian level, and under different incident wind directions. The five prescribed wind directions maintained different velocity distribution patterns and low-wind zone developments in the building wake.

The flow patterns and velocity distributions for direct approaching (0°) and oblique (45°) wind directions in both the "-"- and "T"-shaped building configurations were similar in shape, though the horizontal spread of the low-wind velocity zone "T"-shaped building wake was 18% shorter; whereas the bilateral spread of the low-wind velocity zone along the y-axis was 9.1% shorter than the "-"-shaped building. For the oblique wind scenario (45°), the horizontal spread of the low-wind velocity zone developed in the "T"-shaped building wake was 14.3% shorter than that of the "-"-shaped building, and the bilateral width of the low-wind velocity zone along with the y-axis was 13% narrower. For the oblique opposing (135°) wind, where the front section (without the protruding structure) of the "T"-shaped building appeared in the wake, the horizontal spread of the low-wind velocity zone was the same as the one developed in the "-"-shaped building (Figure 9d). As air turbulence occurred and the vortex was developed around the corners of the protruding structure in the back section of the "T"-shaped building, the low-wind velocity zone development was shortened in the wake, and the corresponding size of the air stagnation zone at pedestrian level of the building wake was reduced.

For the lateral (90°) wind direction, the low-wind velocity zone developed in the building wake of the “-”-shaped building was significantly smaller than the one developed in the “T”-shaped building; however, the low-wind velocity zone in the building wake of the lateral (90°) wind was the smallest among those formed by the five prescribed wind directions examined (Figure 4.8c). This zone extended horizontally to 7.3*H* downwind (x-axis), and had a maximum bilateral width of ~1.8*H* (y-axis). When the approaching wind was direct (0°), the low-wind velocity zone reached 8.25*H* (x-axis), and had a maximum bilateral width of 2.9*H* (y-axis) in the building wake. The corresponding downwind extension and maximum bilateral width under the lateral wind (90°) scenario were 11.5% and 37.9%, respectively, notably less than with the direct approaching wind (0°), which represented the worst-case scenario. The smallest zero-wind velocity zone was observed under the lateral wind, with a 3.4*H* downstream extension (x-axis), and a maximum bilateral width of 1.25*H* (y-axis). These dimensions are 20.9% and 37.5% lower than the maximum reach of the zero-wind velocity zone in the downstream and bilateral directions under a direct approaching wind (0°), respectively; thus, the airflow in the building wake under a direct approaching wind (0°) was relatively stagnant, creating a wind environment in this area that may not be favourable for pedestrian activity. When the incident wind direction was 180° (i.e., when the wind was perpendicular to the back of the “T”-shaped building, Figure 4.8e) was similar, and the low-wind velocity area in the building wake was much larger than with the lateral wind angle (90°) condition. The zero-wind velocity zone when the incident wind direction was 180° extended to ~4.3*H* (x-axis) downstream, and covered a broader bilateral region of ~2*H* (y-axis). The area of the low-wind velocity zone in the lateral wind case was similar to that of the zone formed by the direct wind, extending horizontally to ~8*H* (x-axis) downstream, and covering the bilateral region of 2.65*H* (y-axis) in the building wake.

The two oblique winds (45° and 135°) produced smaller low-wind velocity zones than the direct (0°) or opposing (180°) wind conditions. The low-wind velocity zones along the x-axis direction extended to 7*H* (x-axis) and 8*H* (x-axis) downstream in the oblique (45°) and oblique opposing (135°) wind cases, respectively. Similarly, when the protruding back section of the building appeared as the leeward wall in the oblique (45°) wind case, the development of the low-wind velocity zone was shortened, possibly due to the vortex formation around the corners of the protruding structure on the leeward wall. Although both oblique cases showed a shorter zero-wind velocity flow distance of 3.6*H* (x-axis), and a narrower bilateral reach of 1.65*H* and 1.7*H* (y-axis) when compared with horizontal and bilateral extensions in the direct approaching (0°) and opposing wind (180°) cases, the gross area of the low-wind velocity zone in the building wakes of the two oblique wind cases were still larger than in the lateral wind (90°) scenario; thus, the building wake wind environments were still less favourable for pedestrian activity.

4.2.3 Wind direction and flow patterns around “+”-shaped building

The "+"-shaped building is horizontally and bilaterally symmetrical; thus, only two wind directions were modelled and studied, as the direct approaching wind is analogous to the lateral and opposing wind directions, and the oblique approaching wind is analogous to the oblique opposing wind direction.

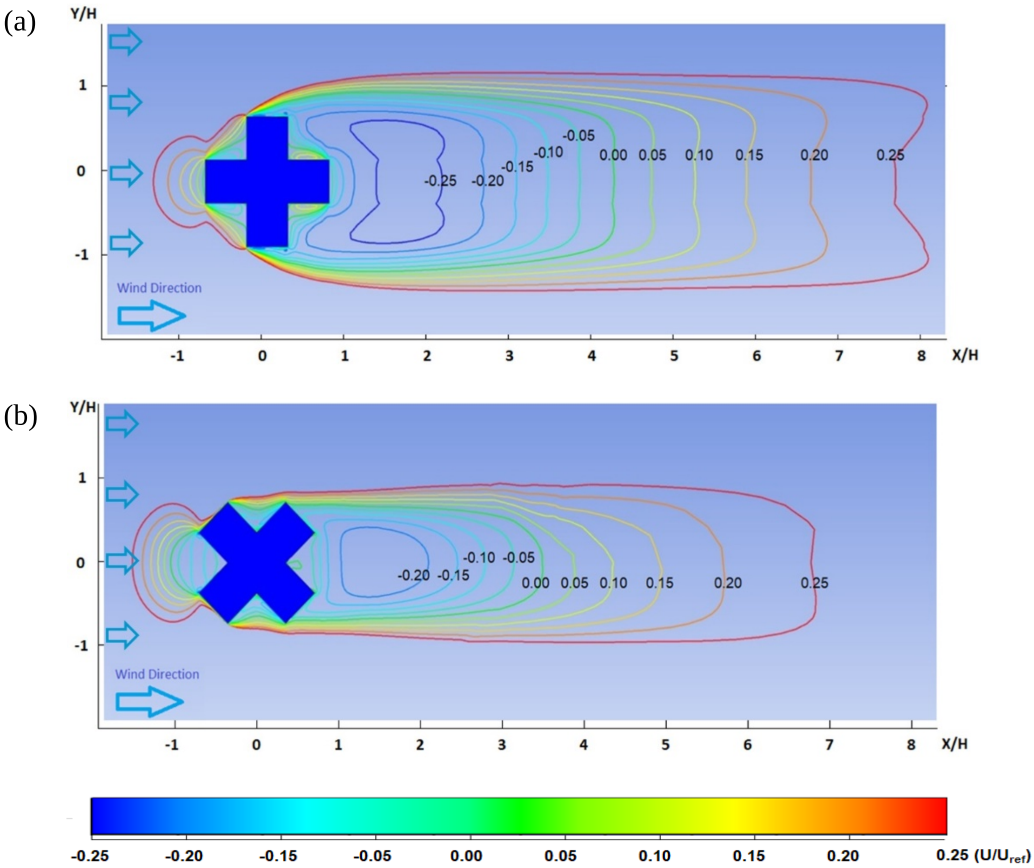

Figure 4.9 Distributions of U/U_{ref} in the horizontal plane at pedestrian height (1.75 m) of the "+"-shaped building, for: (a) direct (θ = 0°, 90°, 180°), and (b) oblique approaching wind angles (θ = 45°, 135°).

The area of the low-wind velocity zone developed in the building wake under oblique wind conditions (45°, 135°) was smaller than with direct approaching (0°), lateral (90°), and opposing (180°) wind conditions (Figure 4.9). When the incident wind was oblique (45° and 135°), the low-wind velocity zone extended horizontally to 6.8*H* (x-axis) downstream, and had a maximum bilateral reach of only 1.9*H* (y-axis). Its length and width were 15.0% and 30.9% smaller than those of the low-wind velocity zones in the direct, lateral, and opposing direction cases, respectively, where the downstream reach of the low-wind velocity zone was 8H (x-axis), and the maximum bilateral reach was 2.75H (y-axis). The zero-wind velocity zone in the oblique (45°, 135°) wind case extended to 3.5H (x-axis) downstream, and bilaterally to 1.3H (y-axis); however, under direct (0°), lateral (90°), and opposing (180°) wind conditions, the zero-wind velocity zone reached 4.3H (x-axis) downstream, and 1.75H along the y-axis. Accordingly, there was less airflow in the building wakes under these latter wind directions, and they created less comfortable environments for pedestrian activity. When simulating the "+"-shaped building, the protruding structure in the back section of the building appears on the leeward in both direct (0°, 90°, 180°) and oblique (45°, 135°) wind directions. As a result, the air turbulence developed near the protruding structure on the leeward wall shortened the distance and horizontal spread of the low-wind velocity zone in the building wake. It can further be observed that the low-wind velocity zone developed in the oblique wind (45°, 135°) scenario would be shorter than the one with a direct (0°, 90°, 180°) approaching wind (Figures 4.8 and 4.9). Hence, the airflow pattern in the "+"-shaped building wake would create a smaller air stagnation zone, and be provide more preferable outdoor conditions for pedestrian activity.

4.2.4 Wall pressure distribution of "-"-shaped building

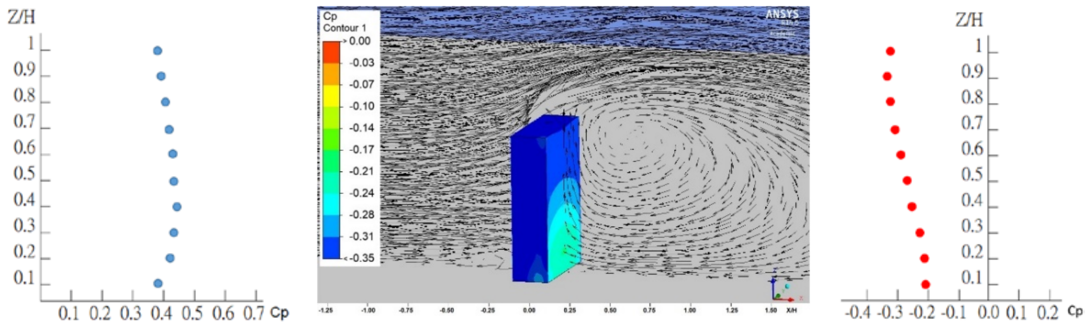

(a)

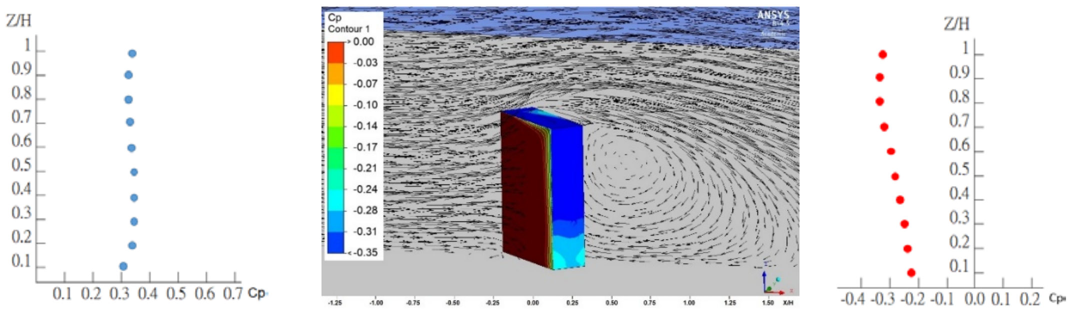

(b)

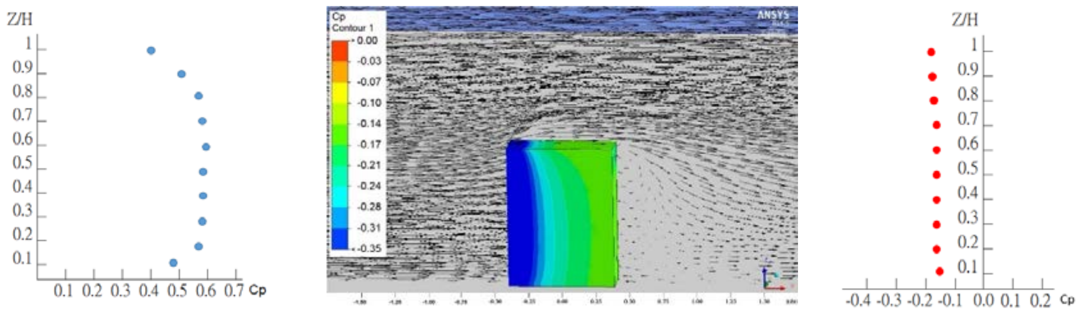

(c)

Figure 4.10 Pressure and airflow distribution patterns at different height fractions (H = 125 mm) on the surface wall of the "-"-shaped building under three different incident wind directions: (a) direct (θ = 0°), (b) oblique (θ = 45°), and (c) lateral winds (θ = 90°).

Figure 4.10 illustrates the airflow patterns on the median plane of the normal, "-"-shaped building configuration, and the air pressure (*Cp*) distributions on the windward and leeward walls under the prescribed incident wind angles. It was generally observed that the backflow of air occurred at the lower vertical levels or floors on the leeward wall of the building, and the flow separation created an underpressure zone that enhanced fresh air intake, thus driving the building's natural ventilation for windows along the leeward wall. This phenomenon became more noticeable in the direct approaching (0°) scenario, where horizontal air movement on the leeward wall only occurred at the lower building level. For the lateral (90°) wind direction, the vortex in the building wake was incomplete, and the underpressures developed along the leeward wall were relatively consistent across different vertical distances of the building. Further, the backflow of air took place equally across the leeward wall. When the air current flowed back onto the lower part of the leeward wall, it moved upward, causing an uplift from the mid-level of the building to the roof (Figure 4.10). Though the underpressure became more substantial at the upper level, the vertical movement of airflow was dominant over the horizontal, creating less favourable wind conditions for the mid-to-upper floors, where the wind velocity was significantly reduced.

Figure 4.11 shows the pressure coefficients along the leeward wall of the building under different incident wind directions. Generally, the air pressure on the lower levels of the building was greater than in the middle or upper floors across different wind directions. In both direct approaching (0°) and oblique (45°) wind cases, a relatively profound decrease of pressure coefficients on the leeward wall from Z/H = 0.1–0.8 was observed. The upward pulling forces in both the direct approaching (0°) and oblique (45°) wind cases were dominant, thus diminishing the fresh air intake along the upper floors, and likely weakening the benefit of natural ventilation through the leeward wall windows. In contrast, the pressure drops in the lateral (90°) wind scenario were relatively steady along the vertical height across the leeward walls, leading to relatively minor variations of wind flow on different vertical levels.

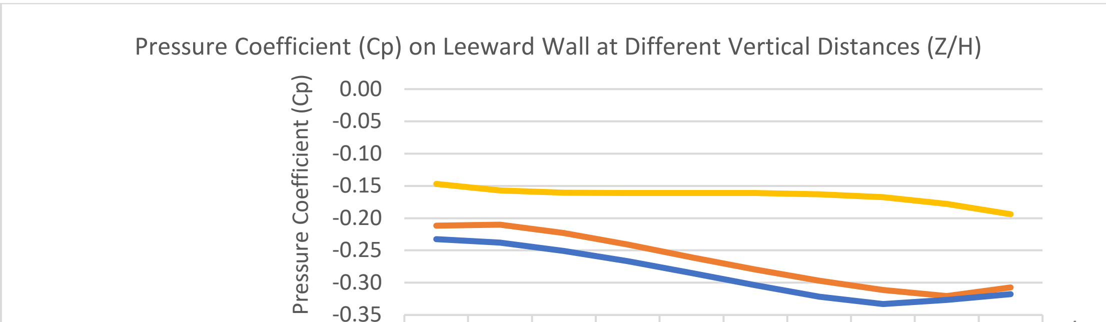

	0.1	0.2	0.3	0.4	0.5	0.6	0.7	0.8	0.9	1.0
Direct Approaching Wind (0°)	-0.21	-0.21	-0.22	-0.24	-0.26	-0.28	-0.30	-0.31	-0.32	-0.31
Oblique Approaching (45°)	-0.23	-0.24	-0.25	-0.27	-0.29	-0.30	-0.32	-0.33	-0.33	-0.32
Lateral Wind (90°)	-0.15	-0.16	-0.16	-0.16	-0.16	-0.16	-0.16	-0.17	-0.18	-0.19

Figure 4.11 Distribution of the pressure coefficient (C_p) at different height fractions (H = 125 mm) on the leeward wall of the "-"-shaped building under different incident wind angles.

4.2.5 Wall pressure distribution of "T"-shaped building

Figure 4.12 illustrates the airflow pattern on the median plane of the "T"-shaped building, and air pressure distributions on the windward and leeward walls under the prescribed incident wind angles. Again, the backflow of air took place at the lower vertical level or floors on the leeward wall of the building, and the flow separation created an underpressure zone that enhanced fresh air intake and droves natural ventilation of the leeward wall building windows. This phenomenon became more noticeable in the direct approaching (0°) and opposing (180°) wind directions, where horizontal air movement on the leeward wall only occurred at the lower level of the building. Similarly, when the air current flowed back onto the lower part of the leeward wall, it moved upward, causing an uplift from the mid-level to the roof of the building. Though the underpressure became more substantial at the upper level, the vertical movement of airflow was dominant, creating less favourable wind conditions for mid-to-upper floors where the wind velocity was considerably reduced.

The pressure coefficient (*Cp*) contours in Figure 4.12 also demonstrate the change of air pressure imposed on the leeward wall of the building under different wind directions, revealing that the decreasing trend of *Cp* on the leeward wall in the direct approaching wind case (0°; Figure 4.12a) is more drastic compared to the other wind scenarios. This is notably similar to the findings from the “-”-shaped building (Figure 4.10), implying a stronger upward pulling force of air on the leeward side, further reducing the horizontal air movement that allows air to naturally ventilate the under pressure upper floors.

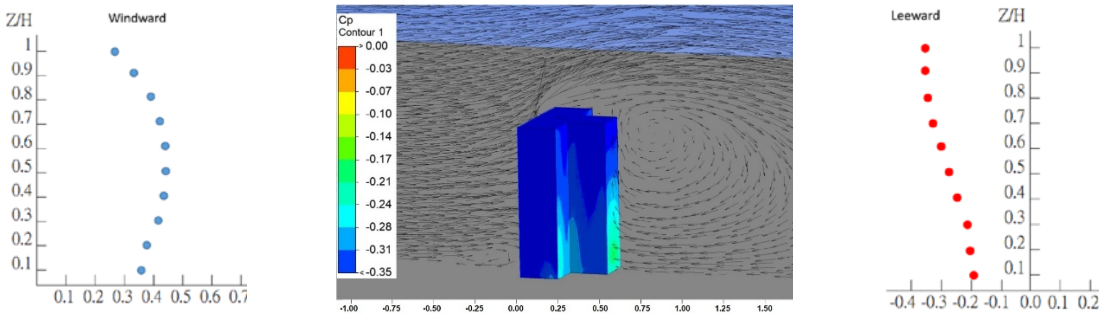

(a)

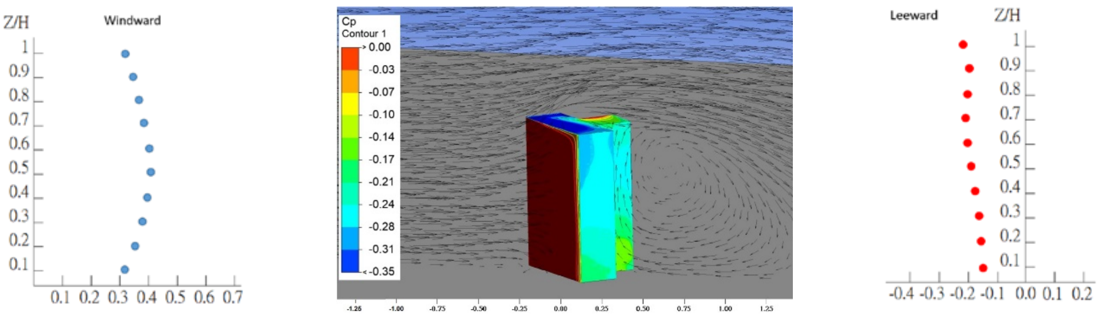

(b)

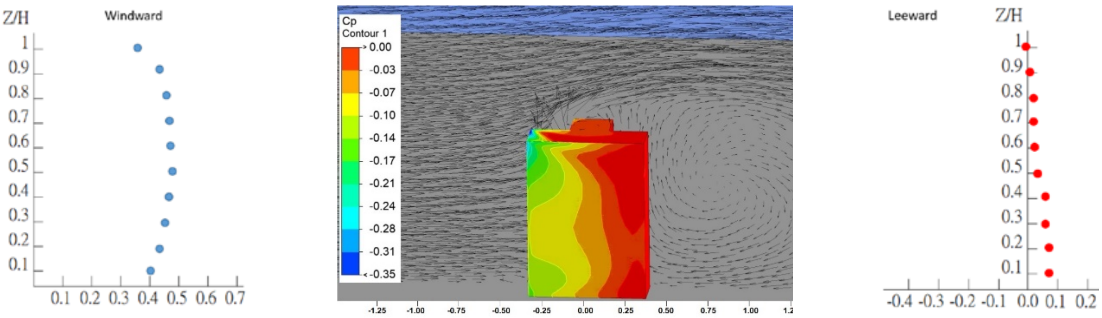

(c)

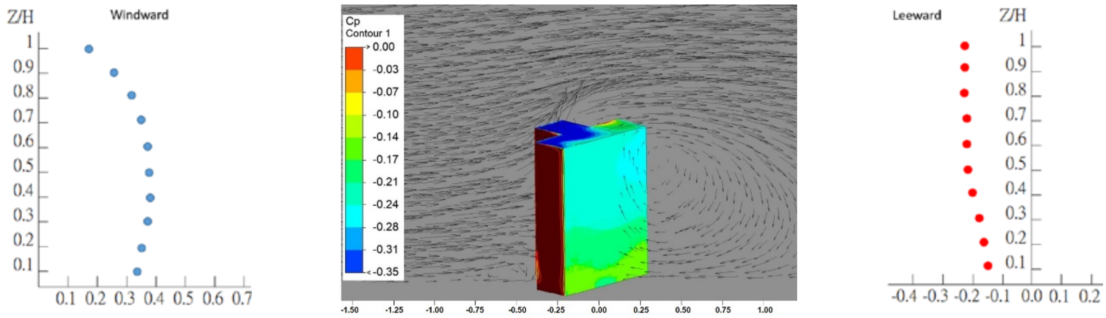

(d)

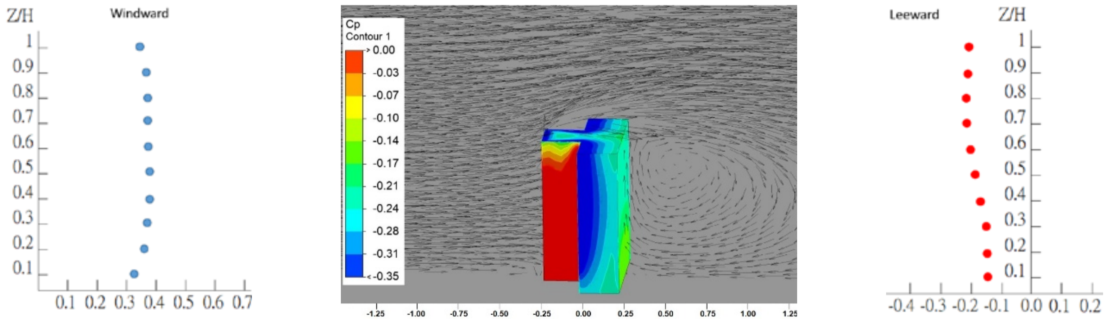

(e)

Figure 4.12 Pressure and airflow distribution patterns at different height fractions (H = 125 mm) on the surface wall of the "T"-shaped building under five different incident wind directions: (a) approaching (θ = 0°), (b) oblique approaching (θ = 45°), (c) lateral (θ = 90°), (d) oblique opposing (θ = 135°), and (e) opposing winds (θ = 180°).

Figure 4.13 shows the pressure coefficient along the building's leeward wall under different incident wind directions. The air pressure on the lower levels of the building was generally higher than on the middle and upper floors for all five prescribed wind directions. The direct approaching wind (0°) showed a relatively profound decrease of pressure coefficients on the leeward wall from Z/H = 0.2–0.8. Comparatively, the pressure drops in oblique (45°), lateral (90°), and opposing (180°)

wind angles were gradual along with the vertical height on the leeward walls. In the direct approaching (0°) wind scenario, the upward pulling force was dominant, diminishing the potential fresh air intake on the upper floors, and weakening the benefits of natural ventilation through the windows on the leeward wall.

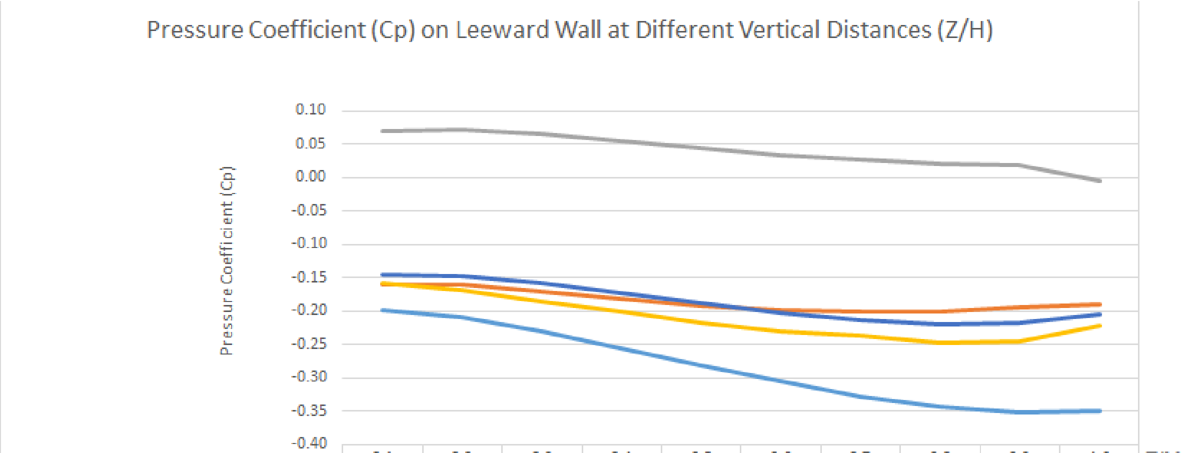

	0.1	0.2	0.3	0.4	0.5	0.6	0.7	0.8	0.9	1.0
Direct Approaching (0°)	-0.20	-0.21	-0.23	-0.26	-0.28	-0.31	-0.33	-0.34	-0.35	-0.35
Oblique Approaching (45°)	-0.16	-0.16	-0.17	-0.18	-0.19	-0.20	-0.20	-0.20	-0.19	-0.19
Lateral Wind (90°)	0.07	0.07	0.07	0.06	0.04	0.03	0.03	0.02	0.02	0.00
Oblique Opposing (135°)	-0.16	-0.17	-0.18	-0.20	-0.22	-0.23	-0.24	-0.25	-0.24	-0.22
Opposing Wind (180°)	-0.15	-0.15	-0.16	-0.17	-0.19	-0.20	-0.21	-0.22	-0.22	-0.20

Figure 4.13 Distribution of the pressure coefficient (*Cp*) at different height fractions (H = 125 mm) on the leeward wall of the "T"-shaped building under different incident wind angles.

4.2.6 Wall pressure distribution of "+"-shaped building

Figure 4.14 illustrates the airflow patterns along the median plane of the "+"-shaped building, and the distributions of air pressure on the leeward wall under different incident wind angle conditions. Identical to the "T"-shaped building, the backflow of air occurred outside the windows along the lower level of the leeward wall, facilitating fresh air intake and natural ventilation; however, this was the lone level of horizontal air movement along the leeward wall. An upward movement of air from the mid-level to the roof of the building created less favourable ventilation conditions for units in this range due to the reduced horizontal wind velocity. The pressure coefficient contours shown in Figure 4.14 also show the variations in air pressure imposed on the building's leeward wall under different incident wind angles. Like the "-" and "T"-shaped building configurations, the decrease in *Cp* along the vertical height of the leeward wall was more noticeable in the direct approaching (0°) wind scenario, resulting in the units on the upper floors of the leeward experiencing less natural ventilation.

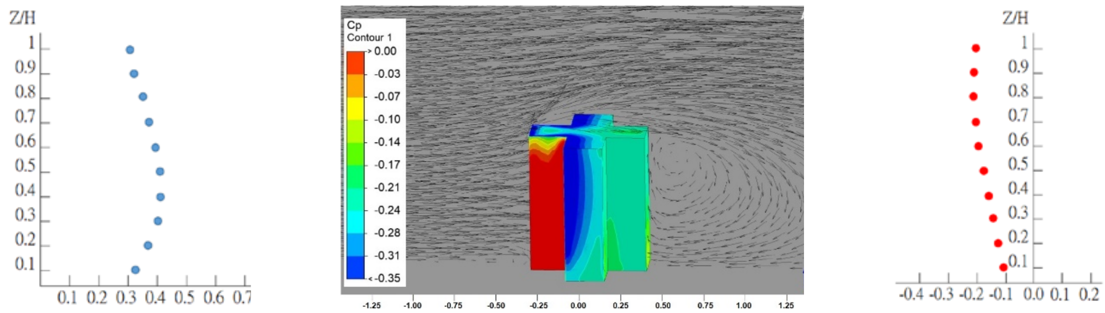

(a)

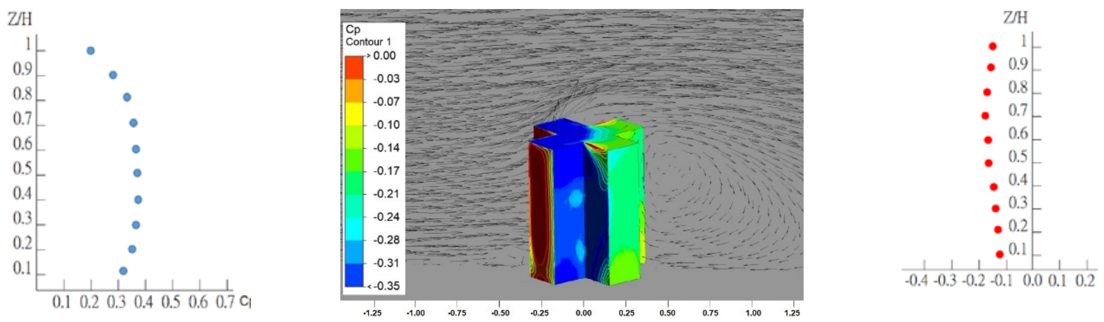

(b)

Figure 4.14 Pressure and airflow distribution patterns at different height fractions (H = 125 mm) on the surface wall of the "+"-shaped building under two different incident wind directions: (a) direct (θ = 0°, 90°, 180°), and (b) oblique approaching winds (θ = 45°, 135°).

In Figure 4.15, the C_p along the leeward wall of the building under different incident wind directions are plotted. The air pressures exerted on the leeward division of the building under the direct approaching (0°, 90°, 180°) wind angles were lower than for the oblique wind angle (45° and 135°). Accordingly, units with windows on the leeward wall experienced better natural ventilation when the wind was blowing from oblique angles. Additionally, the air pressure outside the lower-level windows was higher than outside the middle and upper-level windows under all prescribed wind conditions. The pressure dropped gradually with height, and increased again at 0.7*H* and 0.8*H* (the first upper-level floor). Thus, lower units with windows on the leeward wall (particularly under oblique wind conditions) experienced better air intake and natural ventilation than other unit locations in the "+"-shaped building; although, an upward vertical movement of air again diminished the benefit of natural ventilation through the upper-level windows along the leeward wall.

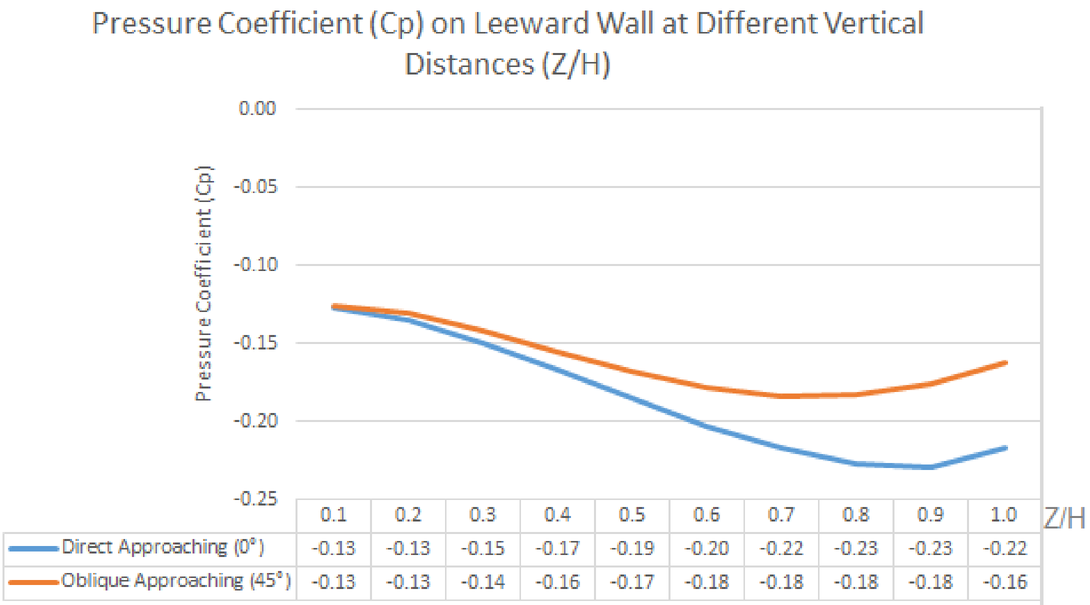

Figure 4.15 Distribution of the pressure coefficient (*Cp*) at different height fractions (*H* = 125 mm) on the leeward wall of the “+”-shaped building under different incident wind angles.

4.3 Summary

It was determined that the incident wind angle and building orientations of "T"- and "+"-shaped buildings, common configurations in Hong Kong, had a substantial effect on the low-wind velocity zone development in the wakes, and pressure distributions along the leeward building walls when compared to a normal, “-”-shaped building configuration. For the "T"-shaped building, five incident wind angles were considered: direct approaching (0°), oblique approaching (45°), lateral (90°), oblique opposing (135°), and opposing (180°); whereas two were considered for the "+"-shaped building direct (0° = 90° = 180°) and oblique (45° = 135°).

To conclude, incident wind directions and building configurations had significant effects on the ventilation of an urban setting, as well as the air qualities in outdoor and indoor environments. First, when the wind blows from an oblique (45°) or lateral (90°) angle of a “T”-shaped or “+”-shaped building, the horizontal distance between the building and low-wind velocity zone in its wake was the smallest, and corresponding air velocity in the building wake was the highest. Second, the vortex formed near the protruding structure in the back section on the leeward side of the building could help shorten the horizontal spread of the zero- and low-wind velocity zone in the building wake. The resulting high-velocity flow on the leeward side can penetrate more deeply into the street canyon, facilitate the dispersion of air pollutants in the building wake, and thus provide more favourable outdoor wind conditions for pedestrian activities within this region. Third, natural ventilation via windows due to pressure differences on the leeward wall of the building can also help improve indoor environment quality; however, the vertical air movement along the upper-level of the leeward wall is noticeable and dominating under all incident wind directions. This effect diminishes the benefit of natural ventilation for leeward windows on the upper floors. The ventilation force on the leeward wall was the highest when the lateral wind was dominating, while the *Cp* values of the leeward walls in all other wind directions were significantly lower. The direct approaching (0°) wind demonstrated the worst-case scenario in terms of the low wake airflow and poor air ventilation along the leeward wall, particularly in the upper-level. Based on the above observations, architects or building engineers must consider building shape and orientation to enhance natural ventilation and wind comfort for pedestrians inside of building wakes. Further, fresh air intake through windows installed on the leeward wall of buildings should be properly designed to optimize natural ventilation.

CHAPTER 5 Wind Direction and Building Array Arrangement on Airflow and Contaminant Distributions in the Central Space of Buildings

This chapter elucidates the effects of incident wind angles on wind velocity and pollutant distribution inside the central space of two building arrays (‘L’- and ‘U’-shaped) using computational fluid dynamics simulations. The ‘L’-shaped array performed better than the ‘U’-shaped array by forming a smaller low-wind-velocity (LWV) zone in the central space of the buildings (34.9–76.11% of total space), performing best at an incident wind angle of 225° (LWV zone coverage: 34.52% of the central space). A 90° incident angle produced the largest LWV zone (81.80%) for the ‘U’-shaped array. Overall, the ‘L’-shaped array generally distributed pollutants better than the ‘U’-shaped array; however, the ‘U’-shaped array with a 180° wind angle had a smaller high pollutant concentration area than the ‘L’-shaped array with a wind angle of 225° ($K_c > 218.5$ covering only 0.37%). The worst vertical dispersion corresponded to a 135° wind angle for the ‘L’-shaped array, which recorded the highest K_c at the mid-level of the building.

5.1 Methodology

5.1.1 Wind tunnel experiment

An experiment was conducted in the BLASIUS wind tunnel (Leitl and Schatzmann, 1998) at the Meteorological Institute of the University of Hamburg. The buildings were modelled and constructed at a scale of 1:200. Before the building models were mounted in the test section, the boundary layer flow was validated based on detailed measurements. The 3 × 7 array of buildings consisted of rectangular blocks. 2D flow measurements were performed in four vertical and one horizontal measurement plane. Emission data were acquired within one horizontal measurement plane, at a height of Z = 1.5 m (full scale). Four ground-level CO_2 emission sources were mounted close to the building, and both flow and CO_2 dispersion were measured within the street canyon, downwind of the source building (Figure 5.1). Dimensionless concentrations are shown using Equation 5.1:

$$K_c = \frac{C_{\ measured}}{C_{\ source}} \frac{U_{ref} H^2}{Q}, \tag{5.1}$$

where $C_{measured}$ is the measured tracer concentration (ppm; previously subtracted background concentration), C_{source} is the tracer concentration at the source (ppm), U_{ref} is the reference wind speed measured at H = 0.66 m (m·s^{-1}), H is the model building height (0.125 m), and Q is the total source strength ($m^3 \cdot s^{-1}$).

Wind tunnel tests from the CEDVAL project, developed by the Meteorological Institute at the University of Hamburg Environmental Wind Tunnel Laboratory (Leitl and Schatzmann, 1998) were employed for model validation (Figure 5.1). The constructed models at a 1:200 scale (unit volume with side H = 0.125 m) were employed for direct comparison with the CEDVAL wind tunnel project, and the test parameters can be found in Table 5.1. The similarity requirements between the wind tunnel and CFD models were strictly tested. The Reynolds (*Re*) number was > 3.7×10^4, thus satisfying the minimum requirement of 1.5×10^4 suggested by Meroney (2004) and confirming *Re* independence.

Table 5.1 Parameters for the scaled model (B1-1)

Parameter	Symbol	Value
Building height	H	0.125 m
Reynolds number	Re	37,252
Power law	$\acute{\alpha}$	0.21
Reference velocity	U_{ref}	6.3 $m \cdot s^{-1}$
Reference height	H_{ref}	0.66 m
Friction velocity	$u*$	0.37772 $m \cdot s^{-1}$
Roughness length	z_0	0.00075 m
Offset height	d	0.00 m
Turbulence length	L	0.32 m

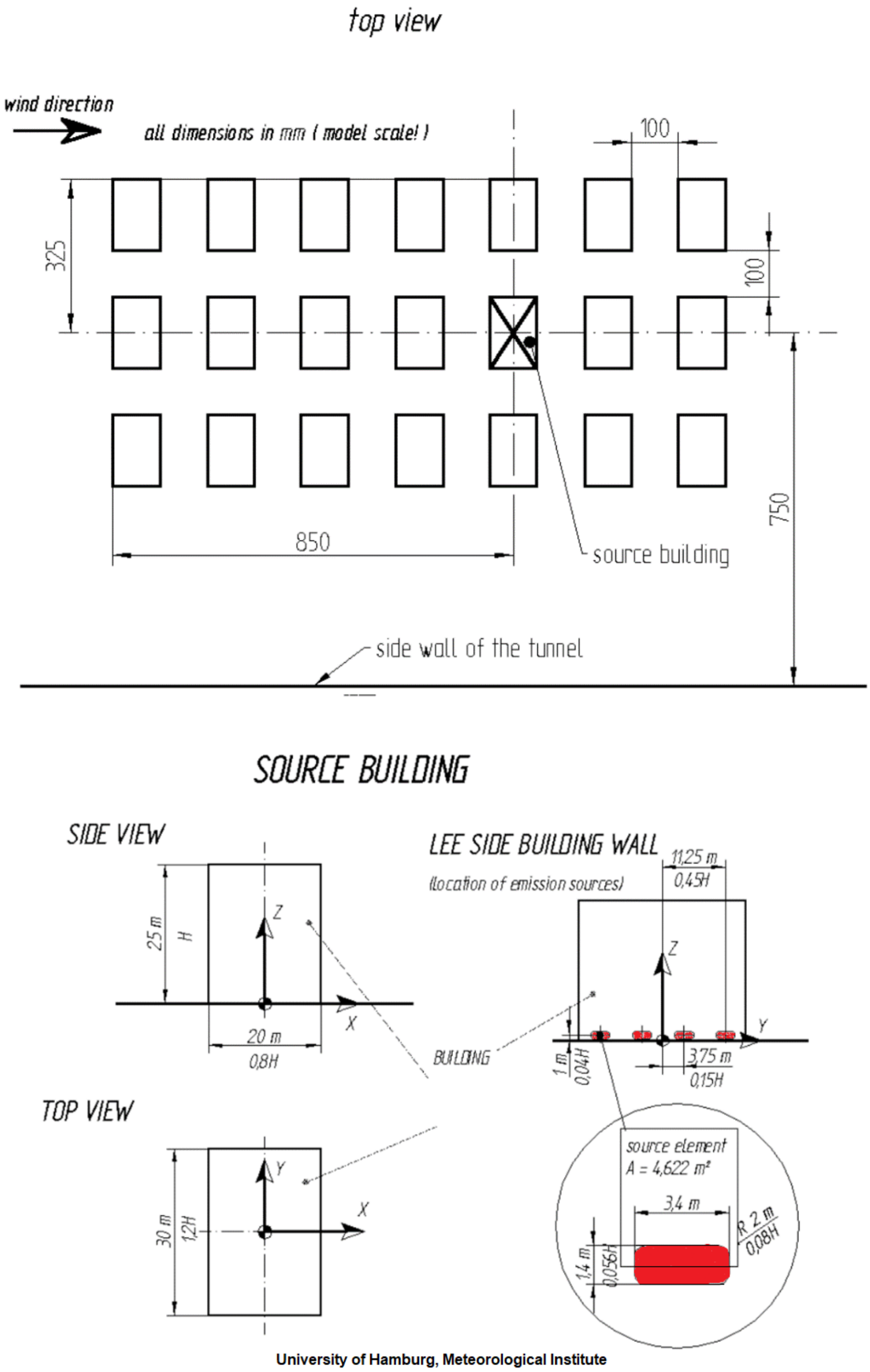

Figure 5.1 Sketch design of the wind tunnel experimental setup with measurement points

5.1.2 *CFD model boundary conditions*

A heterogeneous atmospheric boundary layer (ABL), and near-wall treatments significantly affect the atmospheric flow and pollutant dispersion simulation results (Ai and Mak, 2013); hence, an accurate simulation requires the development of a homogeneous ABL before conducting numerical studies.

To fully develop a horizontally homogeneous ABL flow and achieve equilibrium between the turbulence dissipation and production, the domain inlet boundary conditions were represented by the profile of mean wind velocity U_z, the turbulent kinetic energy k, and turbulent dissipation rate ε, as expressed in Equations 5.2, 5.3, and 5.4, respectively.

$$U_{(z)} = \frac{u^*}{K} ln\left(\frac{z + z_0}{z_0}\right) \quad , \tag{5.2}$$

$$k = \sqrt{C_1 \ ln(z + z_0) + C_2} \quad , \tag{5.3}$$

$$\varepsilon = \frac{u^* \sqrt{C_\mu}}{K(z + z_0)} \sqrt{C_1 ln(z + z_0) + C_2} \ . \tag{5.4}$$

where $U_{(z)}$ is the average wind speed at height z above the ground; z_0 is the roughness length (0.00075 m); u^* is the frictional velocity (0.37772 m·s^{-1}); C_1 and C_2 are constants equal to 0.025 and 0.41, respectively; C_μ is a constant equal to 0.09; and K is the von Karman constant, equal to 0.4187 according to Ai and Mak (2017). Collectively, this set of inlet boundary conditions, when incorporated into an appropriate near-wall treatment on the domain ground, permits a homogeneous ABL (Ai and Mak, 2013; Gorlé et al., 2010).

The downstream vertical boundary was modelled as the outflow, and the sky was treated as a mirror plane. An enhanced wall function was adopted for the building block surfaces, where the computational domain was non-slip. The mesh near the building and ground surfaces was refined to replicate the physical characteristics of the flow. Horizontal homogeneity was required to accurately simulate the approaching ABL flow in the computational domain; thus, the vertical flow profiles prescribed at the inlet had to be preserved in the domain before reaching the buildings (Blocken et al., 2007).

The low-*Re* regions below the first grids, and the effects on the entire wall-bounded flow can be ignored, as the standard wall functions directly linked the walls and near-wall logarithmic layer with a series of semi-empirical formulae (Ai and Mak, 2013). In the present study, an enhanced wall treatment integrated the flow variables down to the walls, adopted near-wall modelling, resolved the viscous sublayer, and computed the wall shear stress from a local velocity gradient normal to the wall. Further, the treatment more accurately predicted the velocity distributions in the recirculation zones near the windward edges and building wakes (Lateb et al., 2013). The computational domain was built using hexahedral elements, employing finer resolutions near the ground and in regions where the plume was evolving. In this study, a relatively fine mesh was imposed in the wall-normal direction (i.e., a small y^+ value of 2–5) to demonstrate the suitability of the selected grid for the enhanced wall treatment.

5.1.3 Computational domain and grid sensitivity

To ensure fully developed wind flow with minimum blockage effects, the upstream, downstream, lateral, and height components of the computational domain were set as 5*H*, 15*H*, 3.4*H*, and 3.4*H*, respectively (Figure 5.2), based on the CFD practice guideline requirements (Franke et al., 2007); however, the lateral distance was adjusted based on the wind tunnel width to ensure accurate reproduction. The blockage ratio was ~1.7%, conforming to the European Cooperation in Science and Technology (COST) Action 732 requirement (Franke et al., 2007). The entire domain was created using structured hexahedral grids with an expansion ratio of 1.2 in the horizontal and vertical directions (Tominaga et al. (2008). The pressure and momentum equations were coupled using the Semi-implicit Method for Pressure-linked Equations (SIMPLE) algorithm, and a second-order upwind scheme was used for discretization. The scaled residuals in the simulation were all set to 10^{-5}, and convergence was obtained at this level.

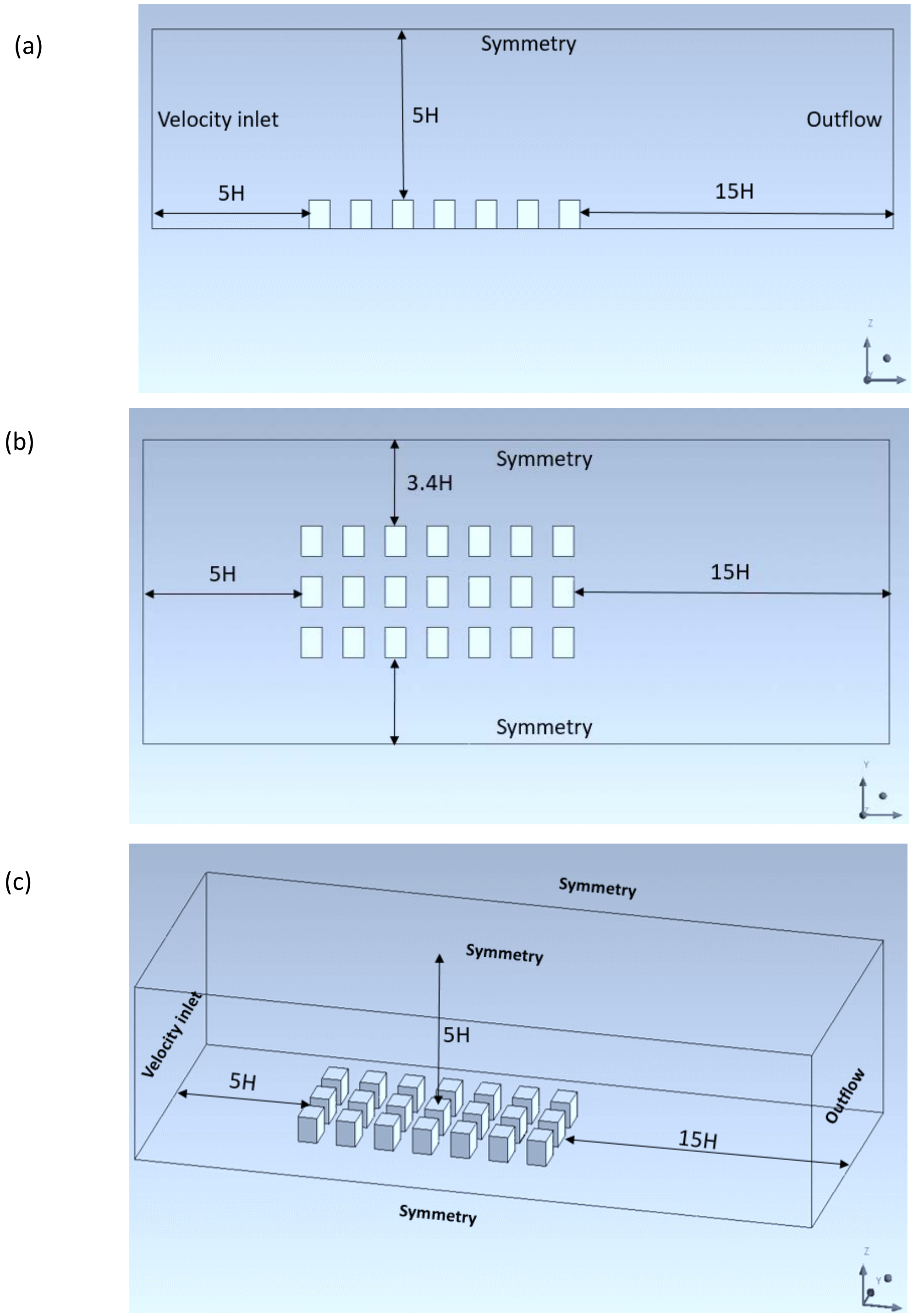

Figure 5.2 Computational domain

Grid-sensitivity analyses can be performed to reduce discretization errors and computational time (Montazeri and Blocken, 2013). In the present study, such an analysis was performed based on three constructed mesh systems, with minimum grid sizes of 0.0005, 0.0002, and 0.00005 m, corresponding to mesh numbers of 2.75 million (coarse), 5.86 million (moderate), and 8.35 million (fine), respectively (Figure 5.3). The simulation results from the three systems were compared to examine the independence of the numerical solution with respect to grid size. The $y+$ values of the first near-wall grids in the vicinity of the building surface and the ground were < 5 (i.e., $y+$ = 4.23) for a minimum grid size of 0.0002 m. For the mesh systems with the minimum grid sizes of 0.0005 m (coarse mesh) and 0.00005 m (fine mesh), the $y+$ values were 10.57 and 1.05, respectively. The correlation coefficient (R^2) and geometrical mean bias (MG) values closer to 1 indicate the improved predictive ability of the model (Du et al., 2019).

(a) 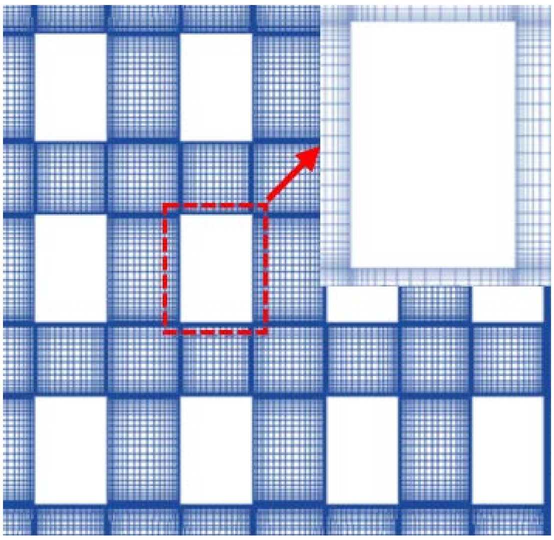

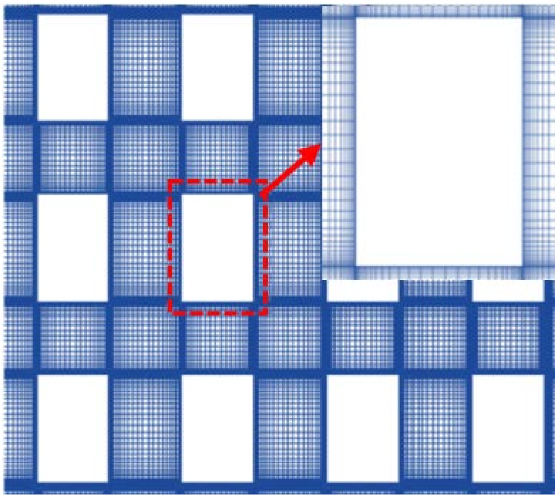
(b)

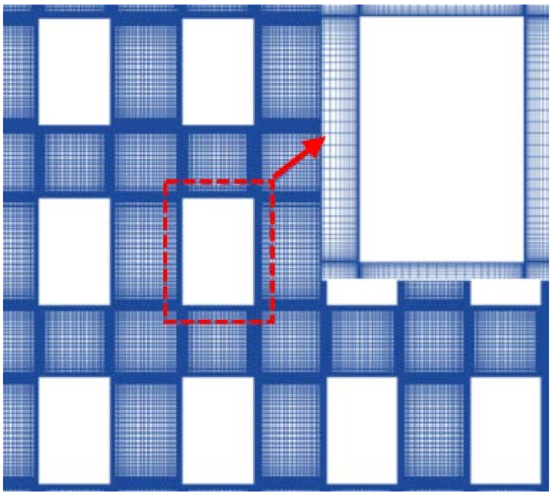
(c)

Figure 5.3 Mesh resolution of the three systems: (a) coarse mesh, minimum grid size of 0.0005 m; (b) moderate mesh, minimum grid size of 0.0002 m; and (c) fine mesh, minimum grid size of 0.00005 m

Figure 5.4 shows a comparison of the non-dimensional wind velocity ratio (U/U_{ref}, where U_{ref} = 6.3 m·s^{-1}) at the reference height (H_{ref}) of 660 mm from the wind tunnel experiment, along with the results of the simulated RNG model using different mesh systems arranged by coarse (C), moderate (M), and fine (F) grids. The coarse mesh generally underestimated wind velocity at all points along the y-axis; however, relatively accurate results were obtained using the moderate and fine meshes. Table 5.2 lists the correlation coefficients of the results generated, with all grids showing good correlation with the experimental data. Notably, fine mesh had the strongest result (R^2 = 0.999), followed by the moderate mesh (R^2 = 0.997); however, the moderate mesh (M) yielded better MG results closer to 1. Further considering the accuracy and expenditure of computational resources, a moderate mesh system with a minimal grid size of 0.0002 m was adopted for the remainder of the analyses.

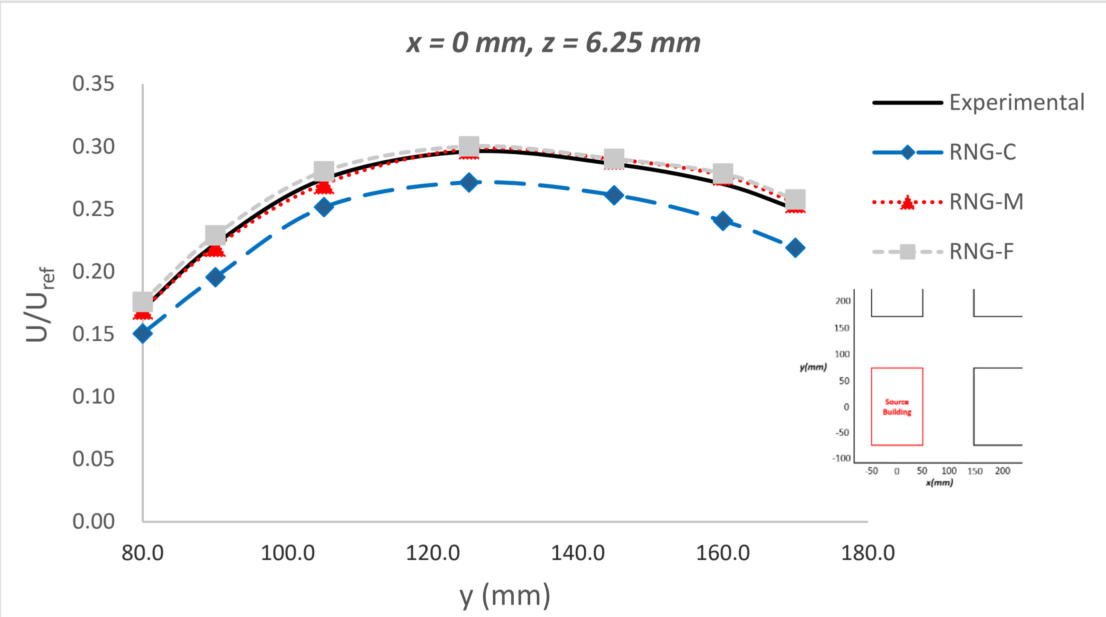

Figure 5.4 Comparison of the wind tunnel data with the simulated RNG k-ε models for coarse (RNG-C), moderate (RNG-M), and fine (RNG-F) mesh systems

Table 5.2 Statistical test results of the RNG k-ε models with three different mesh systems

Statistical Tests	**RNG-C**	**RNG-M**	**RNG-F**
Correlation Coefficient (R^2)	0.996	0.997	0.999
Geometric Mean Bias (MG)	1.112	0.994	0.976

Figure 5.5 compares the wind velocity ratio for the mid-level of the building model from the wind tunnel data sets, and the modelled results using the RNG k-ε model with a moderate mesh system. Figure 5.5(a) and (c) show that the RNG model with a moderate mesh system accurately predicted the wind velocity distribution in the building wake, despite slightly underestimating the wind velocity distribution towards the centre of the street canyon (Figure 5.5(b)).

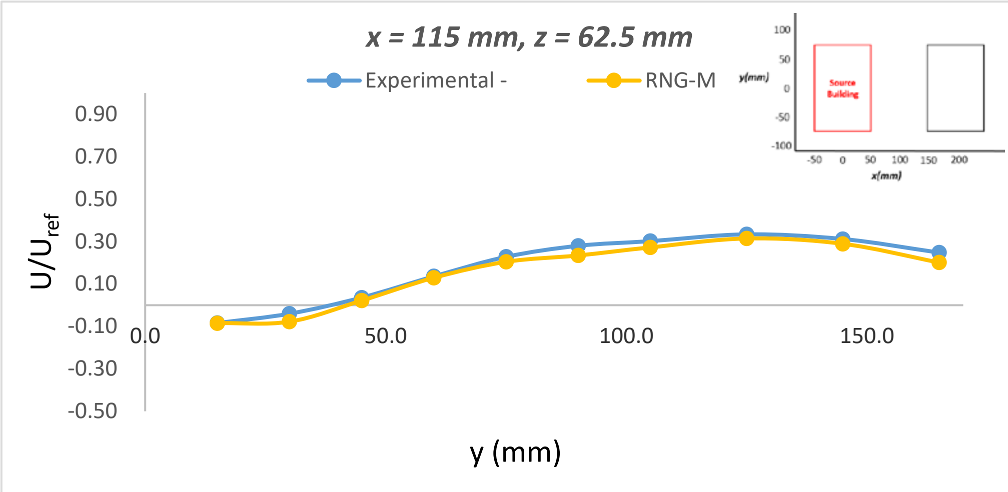

(a)

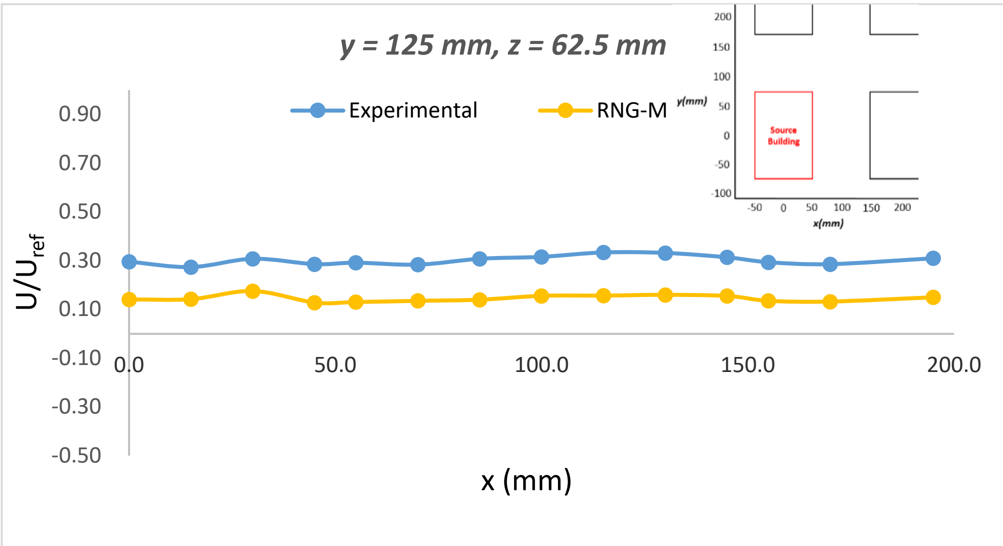

(b)

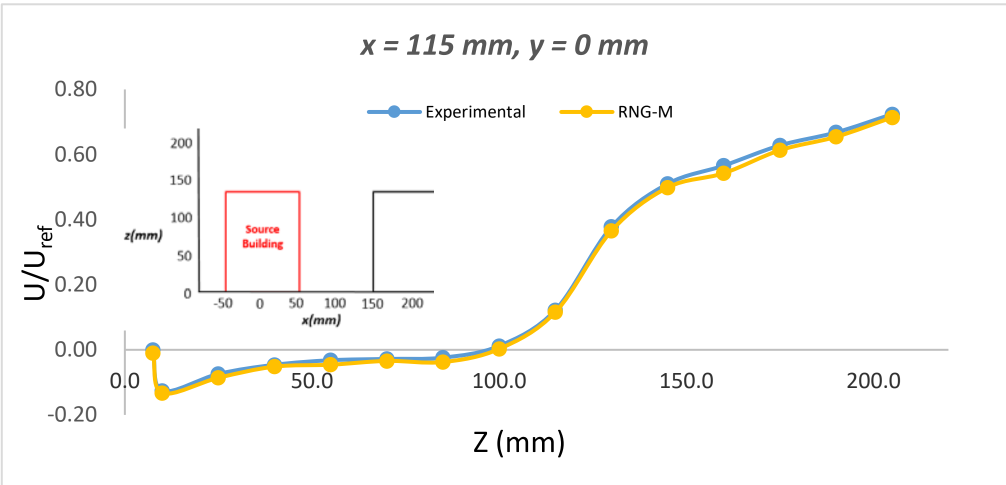

(c)

Figure 5.5 Mean wind velocity distribution for moderate mesh system by RNG as RNG-M

Figure 5.6 displays the tracer gas concentration distribution from the wind tunnel experiment, along with the CFD simulation from the RNG model using the medium mesh system. Measurements were conducted at the pedestrian level (i.e., 1.5 m in full scale), on the leeward wall near the emissions points. The simulated results near the emissions area (i.e., X = 50 mm) varied noticeably from the experimental wind tunnel and modelled data; however, the remaining model results deviated only subtly from the experimental results; therefore, this model was considered accurate and appropriate for the current study.

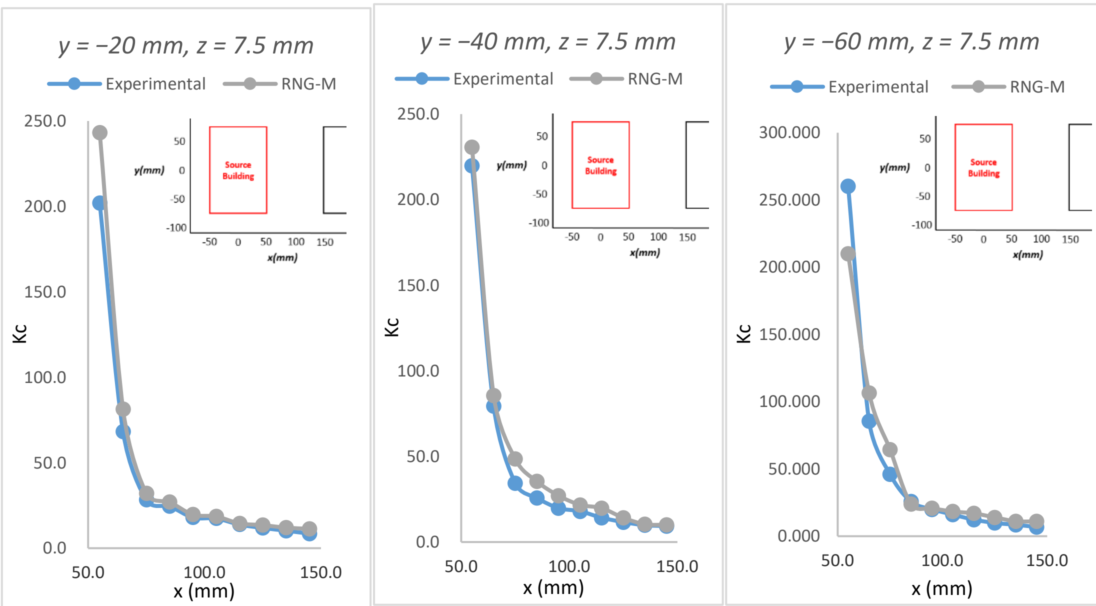

Figure 5.6 Tracer gas concentration distribution for moderate mesh system by RNG as RNG-M

5.1.4 Building configuration and arrays

Chapter 4 of this thesis examined a common "T"-shaped building configuration in Hong Kong during a pilot study under an isolated building setting, and found that the vortex formed near the protruding structure in the back section on the leeward side helped shorten the horizontal spread of the zero- and LWV zones in the building wake. The resulting high-velocity flow on the leeward side penetrated deeper into the street canyon, and facilitated the dispersion of air pollutants in the building wake. Two common building arrangements—‘L’ (Figure 5.7a) and ‘U’ (Figure 5.7b)—were selected to further study the effects of ‘T’-shaped building configurations and incident wind angles on the wind velocity distribution and pollutant dispersion in building wakes.

(a)

(b)

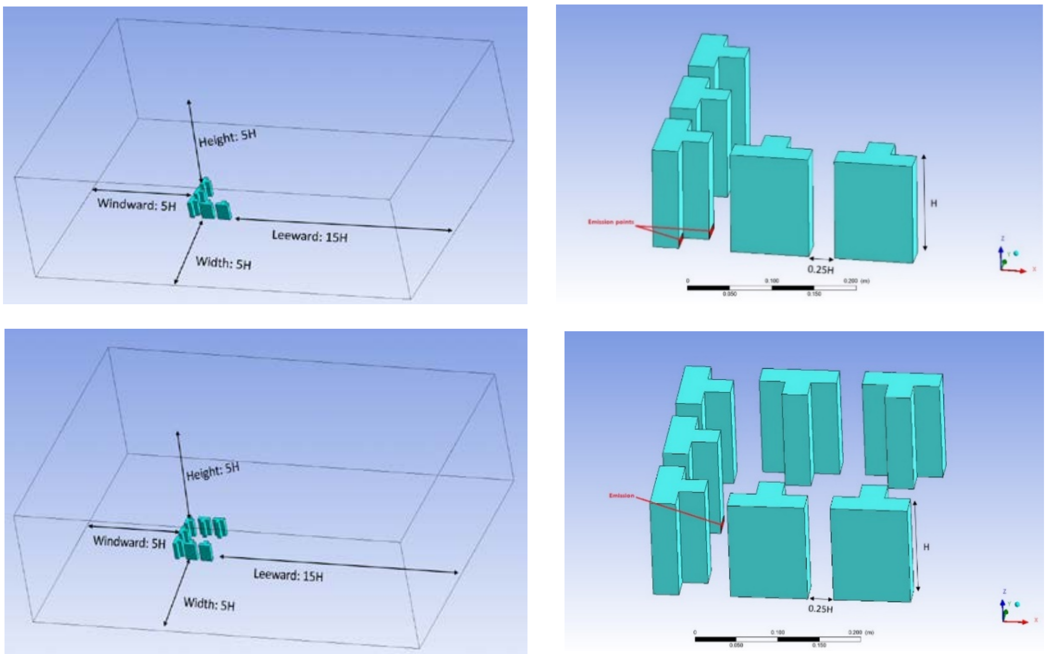

Figure 5.7 The computational domains for: (a) ‘L’-shaped, and (b) ‘U’-shaped arrays

The effects of different wind angles, including direct ($\theta = 0°$), oblique approaching ($\theta = 45°$), oblique opposing ($\theta = 135°$), lateral ($\theta = 90°$), and opposing winds ($\theta = 180°$) (Figure 5.7a and b) were investigated. An oblique opposing wind at θ = 225° was also studied in an ‘L’-shaped array (Figure 5.7a), and the validated mesh, inflow wind profile, computational domain size, turbulence model, and numerical methods discussed above were used for the wind flow simulations around the two building arrays. Mean wind velocity ratios < 0.25 at the pedestrian level (1.75 m at equivalent full scale) in the building wakes were used to identify areas of unfavourable conditions for pedestrian activity. The studied central space was an imaginary rectangular area that covered most of the middle region of the building arrays, and is bounded by the mid-lines of the farthest buildings. Colour summarizing software (http://mkweb.bcgsc.ca/color-summarizer/?analyze) was used to assess the areal percentage classified as the LWV zone in the central space inside the building arrays according to the colour distributions in Figure 5.8.

In addition to the airflow and ventilation distributions, this study modelled the release of a tracer gas (CO_2) from elements of the source building at a constant velocity of 0.025 $m \cdot s^{-1}$ in the X direction towards the central space of the building arrays to simulate pollutant dispersion. The total area of the emissions points was the same as that in the wind tunnel model (CEDVAL B1-1) to mimic the exact flow rate and volume of the released tracer gas. The distributions of the pollutant concentration expressed in a dimensionless concentration, K_c, were calculated according to Equation 5.1.

(a) (b)

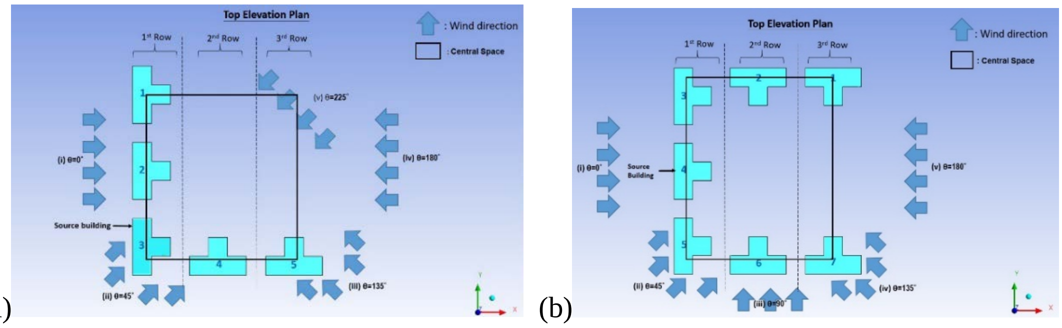

Figure 5.8. Building configurations, arrays, and incident wind directions, for: (a) ‘L’-shaped arrangement, and (b) ‘U’-shaped arrangement

5.2 Results and discussion

5.2.1 Airflow distribution inside the central space of building arrays

Figure 5.9 shows the general features of the wind velocity ratio (U/U_{ref}) distribution at pedestrian level, around ‘T’-shaped buildings, in an ‘L’-shaped array, and under different incident wind directions to assess pollution dispersion and pedestrian thermal comfort. The five prescribed wind directions had different velocity distribution patterns and resulting LWV zones in the building wake and central space of the building array.

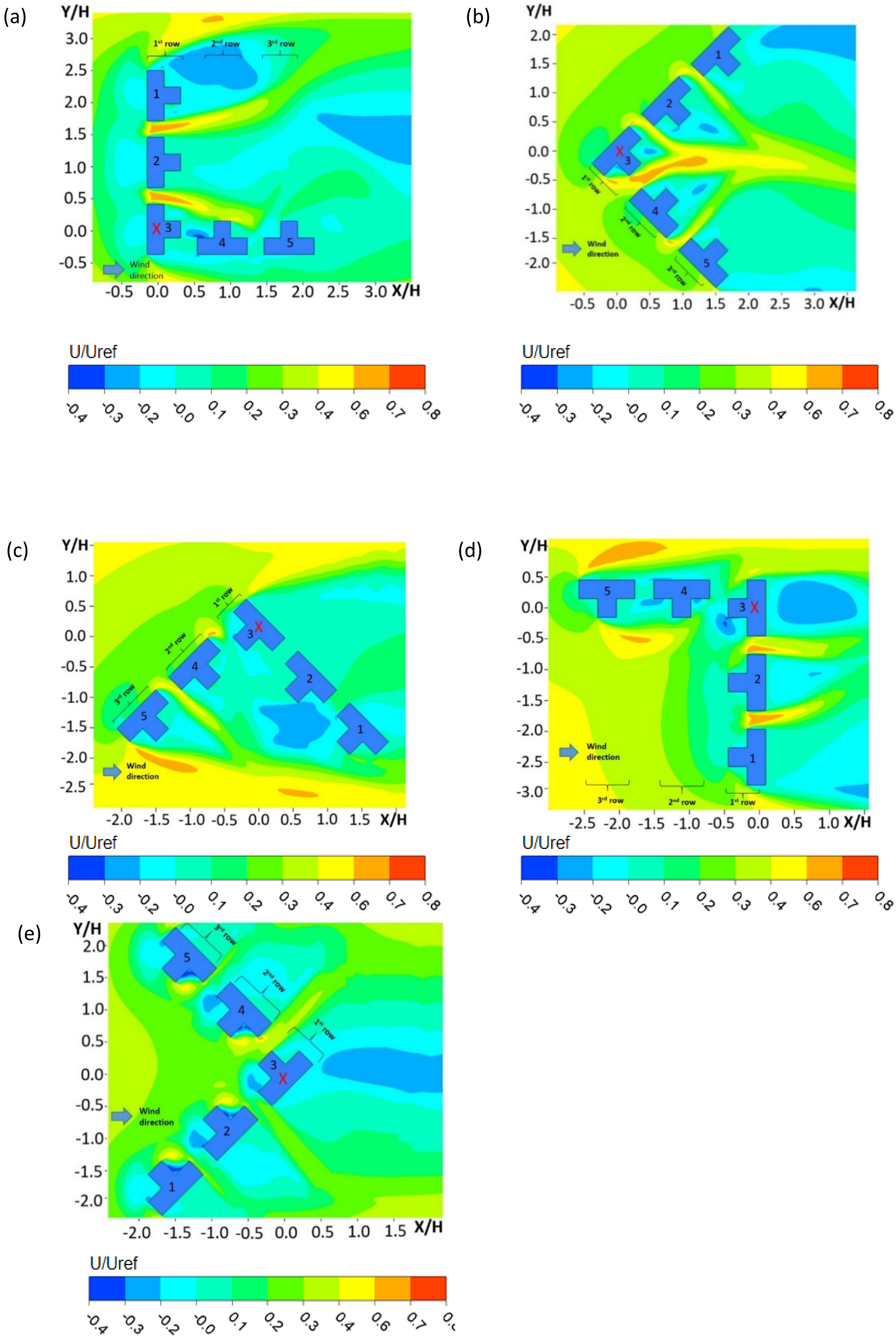

(a)
(b)
(c)
(d)
(e)
Y/H
X/H
1st row
2nd row
3rd row
Wind direction
U/Uref
-0.4 -0.3 -0.2 -0.0 0.1 0.2 0.3 0.4 0.6 0.7 0.8

Figure 5.9 Distributions of U/U_{ref} in the horizontal plane at pedestrian height (1.75 m at equivalent full scale) for the 'L- arrangement, with incident wind angles of: (a) 0°, (b) 45°, (c) 135°, (d) 180°, and (e) 225°

The LWV zone in the central space of the building array was generally the largest (76.11%) for wind hitting the surface of the 1st row of buildings (Figure 5.9a). Similarly, the LWV zone covered 71.42% of the area of the central space for a wind angle of 90° (Figure 5.9c). The oblique scenario portrayed in Figure 5.9b shows a slightly improved air velocity distribution, and an LWV zone covering < 65% of the central space, as the wind infiltrated through the slits in the buildings. In the oblique opposing case (Figure 5.9c), the air infiltrated the building gaps; although, airflow and vortex development were impacted by Blocks 1 and 2 in the 1st row, causing stagnation of the central space air. The opposing and oblique opposing cases depicted in Figure 5.9d and e, respectively, demonstrated improved ventilation inside the central space of the 'L'-shaped building array. The LWV zone in Figure 5.9d covered 51.78% of the central space; whereas the LWV zone Figure 5.9e covered 34.52%. Both cases maintained central spaces of the building array that were facing the wind direction; however, the 1st row of buildings in Figure 5.9d gradually reduced the air velocity passing through the central space by blocking the airflow. Figure 5.9e shows that the air velocity was drastically reduced when the wind approached the surface of the building from an oblique incident angle; therefore, this represented the most ideal wind velocity and outdoor ventilation for the central space in the ‘L’-shaped building array.

Figure 5.10 illustrates the airflow pattern and velocity distribution inside the central space of the ‘U’-shaped building arrays. The ‘U’-shaped array did not perform as well as the ‘L’-shaped array in terms of ventilation and air penetration. Depending on the incident wind angle, the LWV regions occupied 60.71–81.80% of the central space of the building array. Figure 5.10c shows the worst situation, where only 18.20% of the total area inside the central space demonstrated satisfactory airflow ($U/U_{ref} > 0.25$) during a lateral wind. Wind flow approaching the building array from 90° hit Blocks 5, 6, and 7, with the resulting airflow entering the central space. This decelerated air reached Blocks 1, 2, and 3 after passing through the first half of the central space, forming a vortex, which further slowed the air inside the central space. The two cases with oblique incident wind angles (45° and 135°) performed slightly better, and the resulting LWV zone occupied 74.97% (Figure 5.10b) and 73.07% (Figure 5.10d), respectively. The case shown in Figure 5.9b is slightly better than that in Figure 5.10d, since the wind passed through the slits of the buildings at a 45° rotation, and moved freely through the opening of the semi-enclosed arrangement of the ‘U’-shaped arrays.

The resulting air recirculation and vortex formed in front of Blocks 1, 2, 3, and 4 (Figure 5.10d) reduced the airflow velocity inside the central space of the building array. Lastly, the opposing wind (180° angle; Figure 5.10e) was expected to be the best since the opening of the semi-enclosed feature of the building array exposed the central space to the incoming wind, permitting more throughflow; however, the wind in Figure 5.10e directly and horizontally impacted Blocks 3, 4, and 5; thus, recirculation and vortex formation again slowed the incident winds. Further, the wind in this scenario approached the central space, hitting the building blocks at an oblique angle; thus, air velocity and turbulence dissipated very quickly near the windward walls of the buildings. The resulting vortex was not large enough to slow down the airflow reaching the central space of the building group.

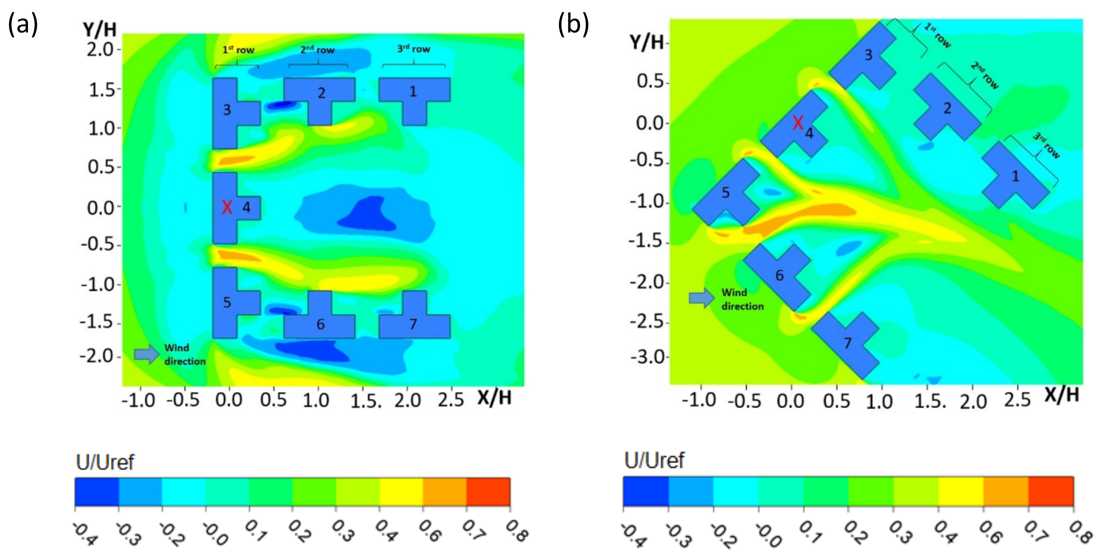

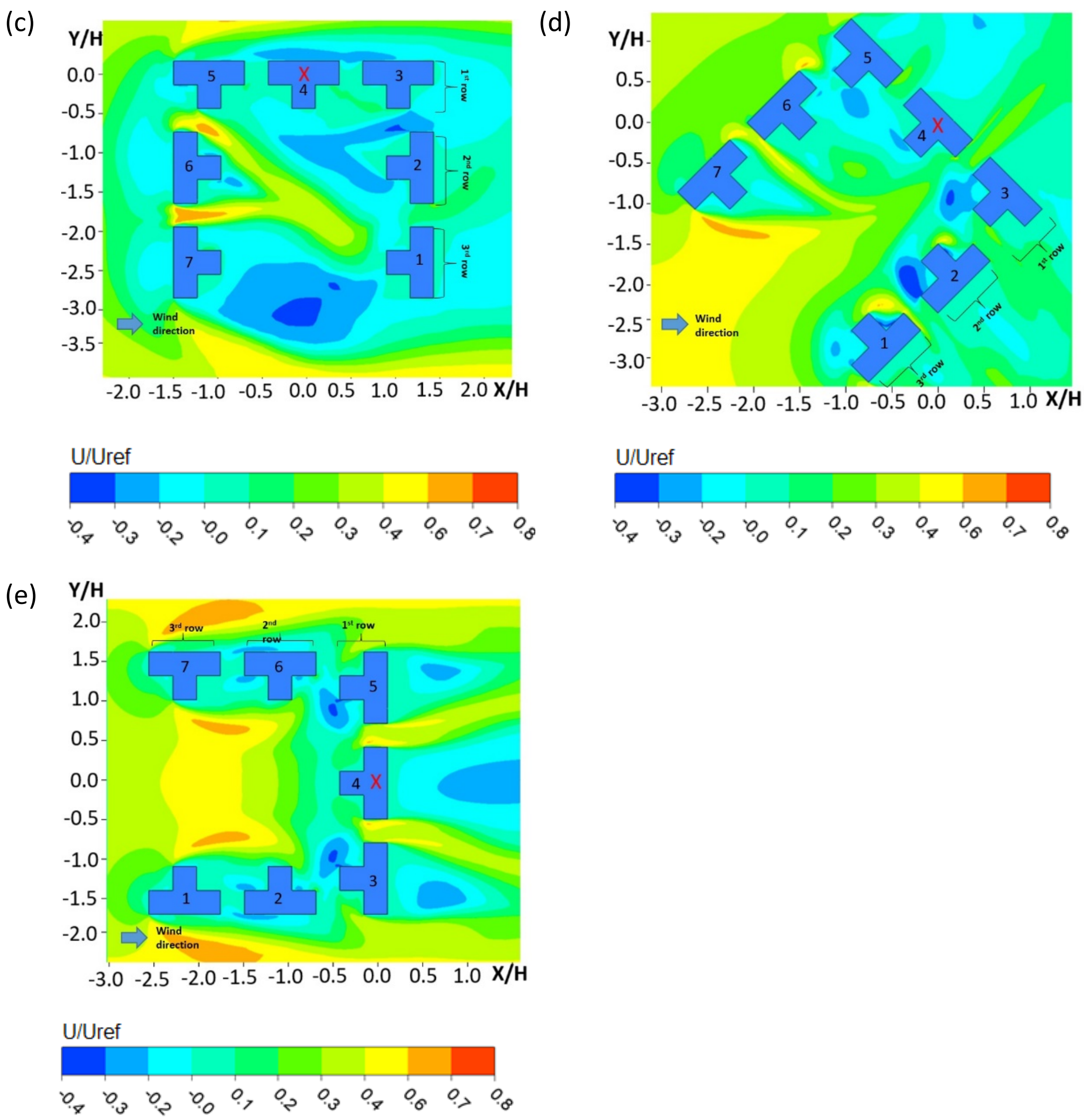

Figure 5.10 Distributions of U/U_{ref} in the horizontal planes at a pedestrian height (1.75 m at equivalent full scale) for the 'U' arrangement, with incident wind angles of: (a) 0°, (b) 45°, (c) 90°, (d) 135°, and (e) 180°

To summarize, the 'L'-shaped building array performed better than the 'U'-shaped array, and oblique wind angles effectively helped maintain airflow penetration and optimized ventilation within the central space of the building array. Additionally, openings in semi-enclosed features of the building arrays that were located downstream from the airflow created favourable ventilation conditions, and helped maintain sufficient wind velocities inside the central space; however, upwind openings in the building array enclosure stopped airflow from reaching building groups situated downstream and perpendicular to the wind direction; thus, the turbulence and recirculation of airflow created LWV zones within the central space of the building arrays, making them less favourable for pedestrian activity.

5.2.2 Central space air contaminant dispersion

To assess the dispersion of air pollutants inside the central space of the building arrays, a simulation of the tracer gas (CO_2) in the vents from the source building was conducted. Figure 5.11 shows the contours of the time-averaged, dimensionless gas concentrations inside the central space of the 'L'-shaped building array.

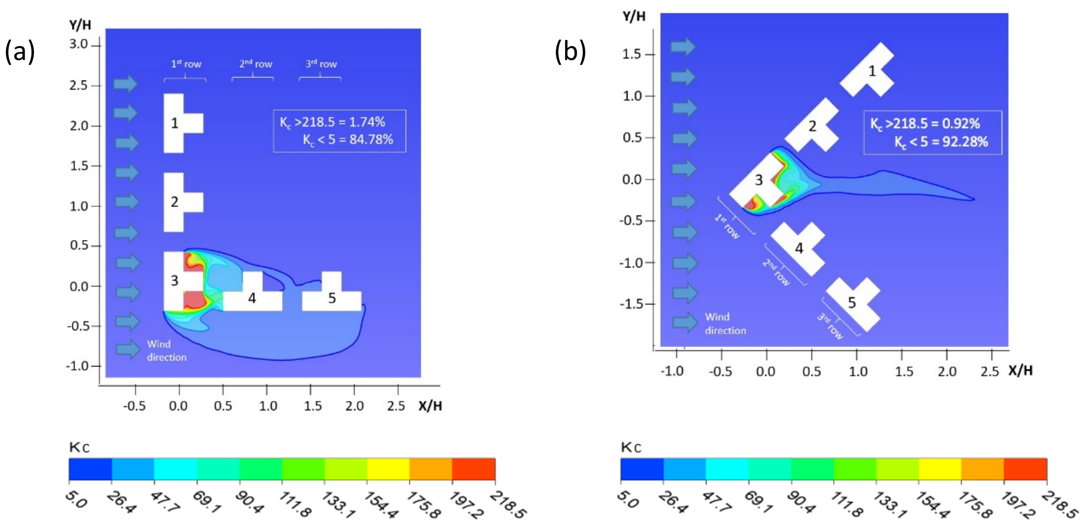

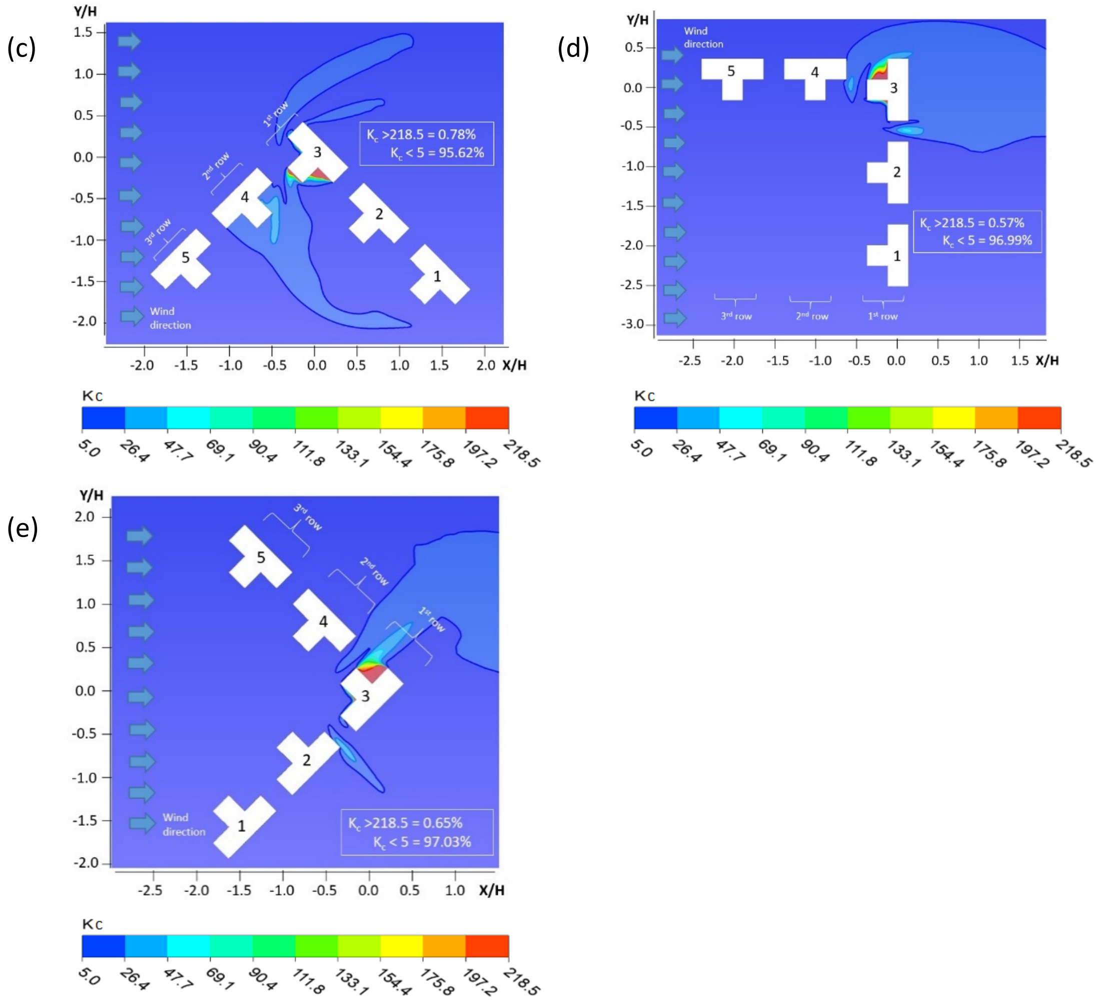

Figure 5.11 Concentration distribution of the 'L'-shaped arrangement at a pedestrian height (1.75 m at equivalent full scale), with incident wind angles of: (a) 0°, (b) 45°, (c) 135°, (d) 180°, and (e) 225°

A distinct high-concentration area ($K_c > 218.5$) appeared near the emission vents in the source building. The tracer gas emitted from the source building was then transported downstream by the air current, where decreased pollutant concentration were observed. As the tracer gas was transported by the airflow, the emissions did not affect upstream buildings or central spaces. The enclosure opening of the building array and the central space were facing the wind direction, thereby minimizing the effect of tracer gas emissions (i.e., air pollutants) on the central space of the building array (Figure 5.11d and e). Figure 5.11d shows that the ratios of the heaviest polluted (K_c > 218.5) and least polluted areas (K_c < 5) were 0.57% and 96.99%, respectively. These values were similar to those observed in Figure 5.11(e), where the ratios of heavily polluted and least polluted areas were 0.65% and 97.03%, respectively. Contaminants accumulated behind the protruding part of the 'T'-shaped building (hereafter referred to as the 'middle block') for oblique angle wind (Figure 5.11e); however, as the source building was located in the downwind position under this wind direction, air pollutants had the least impact on the central space of the building array, creating a more suitable environment for pedestrians. Figure 5.11d shows that the airflow and vortex development were impacted by Blocks 1 and 2 in the 1st row for an oblique wind angle of 135°, which created air stagnation in the central space; consequently, the accumulated pollutant was not efficiently dissipated.

For an oblique wind angle of 45°, the high wind velocity inside the central space facilitated the dispersion of air pollutants, creating steeper and denser pollutant concentration contours (Figure 5.11b); whereas the heavily polluted area occupied ~0.92% of the central space. For an approaching wind angle of 0°, the blockage effect of Block 3 created air turbulence in its wake, and the resulting LWV further hindered emissions dissipation. Consequently, the pollutant lingered near Blocks 4 and 5, heavily polluting 1.74% of the total area.

As the enclosure opening was narrower in the ‘U’-shaped arrays than with the ‘L’-shaped, greater levels of air pollutant accumulation were expected in the central space (Figure 5.12). Figure 5.12a shows the worst dissipation of air pollutants in the central space of the building array (and the largest high pollutant concentration area ratio of 1.63%) occurred under the direct wind scenario, attributed to air turbulence and vortices formed in the wakes of the 1st row of buildings. Building blocks in the 2nd and 3rd rows on both sides helped stabilize the atmosphere in the horseshoe-shaped central space, allowing slow, gradual, and symmetrical dissipation of the tracer gas throughout the central space (manifested by the wide and even contour lines). In Figure 5.12b, the source building was located on the left-hand side of the oblique wind flow; whereas the opening of the semi-enclosed array was located downstream of the emission source, allowing for the airstream to carry the pollutants through the opening of the semi-enclosed structure of the building array. Accordingly, pollutant emissions did not significantly affect the downstream buildings. In the lateral wind case shown in Figure 5.12c, however, Block 3 was located in the wake of the source building (Block 4), creating a blockage effect and air turbulence between the buildings, and inhibiting the dissipation of the air pollutant, which lingered between the spaces of the two buildings. The area ratio of high pollutant concentration was approximately 1.09%, and that of the least polluted area ($K_c < 5$) was the lowest among all ‘U’-shaped arrays (84.86%). Because the openings of the semi-enclosed structure of the building array in Figures 5.12d and 5.12e were facing the incident wind, the emissions points were located downstream of the central spaces; thus, these opposing and opposing oblique wind angles had less impact on the accumulation of air pollutants in the central space of the building arrays. The corresponding area ratios with high pollutant concentrations were 0.69% and 0.37%, respectively; and the low pollutant area ratios in both cases were > 93%. Thus, incident wind angles of 135° and 180° were the best for pollutant dissipation in ‘U’-shaped building arrays; however, the 180° and 225° scenarios in the ‘L’-shaped building arrays maintained larger least-polluted area ratios.

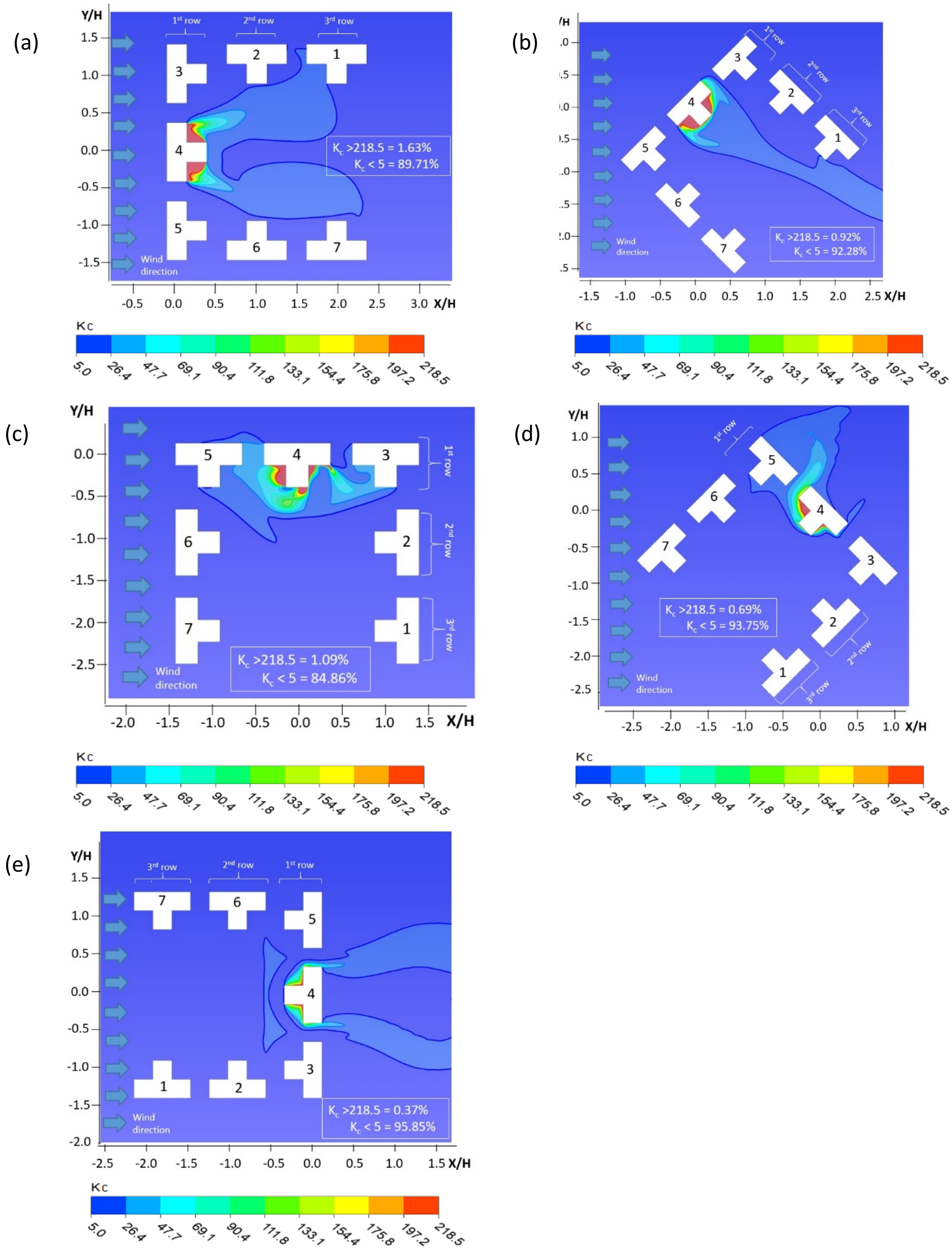

Figure 5.12 Concentration distribution for 'U'-shaped arrangement at pedestrian height (1.75 m at equivalent full scale), with incident wind angles of: (a) 0°, (b) 45°, (c) 90°, (d) 135°, and (e) 180°

5.2.3 Pollutant concentrations on building surfaces

Figures 5.13 and 5.14 display the impacts of air pollutants, and their distribution on the building surfaces under different incident wind angles and building array orientations.

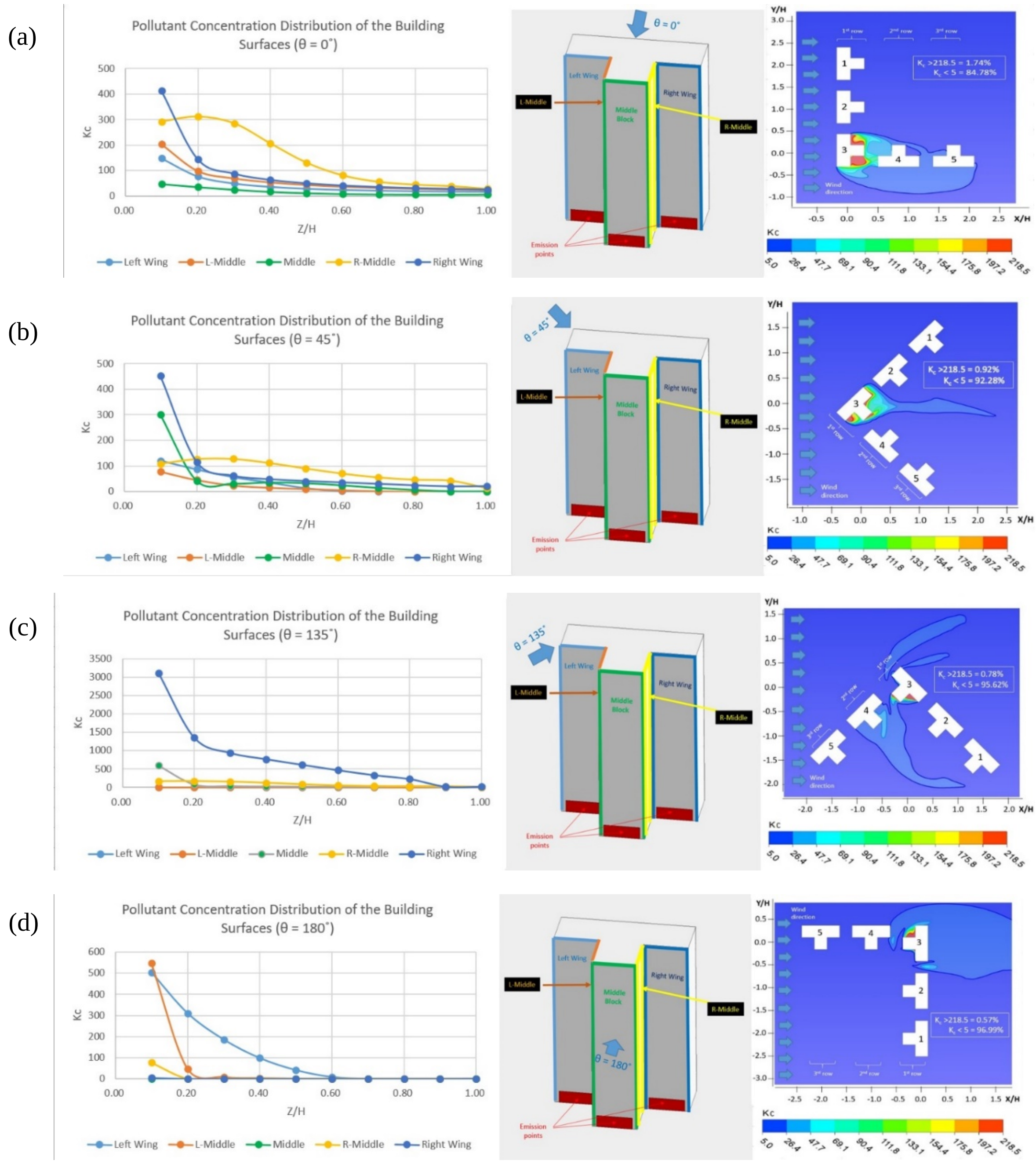

(e)

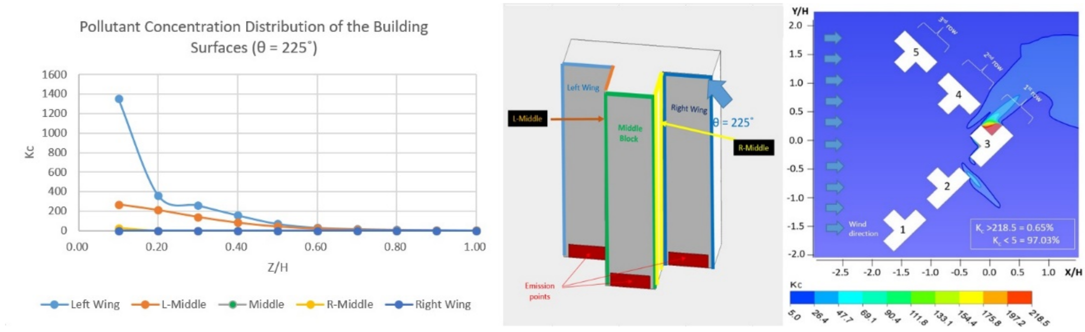

Figure 5.13 Distribution of pollutant concentration on the on the left wing, l-middle, middle, r-middle, and right wing building walls, under incident wind angles of: (a) 0°, (b) 45°, (c) 135°, (d) 180°, and (e) 225° for the ‘L’-shaped building array

The ‘L’-shaped building array showed higher pollutant concentrations at lower levels on the right wing and r-middle building surfaces under an incident wind angle of 0° (Figure 5.13a). A rapid decay in pollutant concentration, and increase in the vertical distance from the emissions points, significantly reduced the pollutant concentration. The contour lines show that the horizontal distributions of pollutants at the pedestrian level, in conjunction with the air pressure imposed by the airflow passing through the gap between Blocks 2 and 3, suppressed the accumulation and horizontal spread of pollutants emitted from the right wing. Figure 5.13b shows that the emissions dispersed relatively rapidly in the oblique windward region, including the left wing and middle walls of the building. The emissions concentration was relatively high at lower levels on the walls of the middle block and right wing, but rapidly decayed at upper levels. All building surfaces showed a rather low pollutant concentration at lower levels (z = 0.2*H*).

For incident winds approaching 90° (Figure 5.13c), the stagnation zone between the right wing and r-middle walls trapped air pollutants more efficiently than on other building surfaces. The front sections of Blocks 4 and 5 reduced the airflow, inhibiting ventilation along the right wing of the source building. Because the left wing is more susceptible to this blockage effect for incident winds approaching 180° (Figure 5.13d), the pollutant concentration at lower vertical levels was high. The rapid airflow caused by turbulence in the upper vertical levels developed between both buildings, and helped dissipate air pollutants; thus, pollutant concentrations on the L-middle wall decayed rapidly. The other building surfaces were unaffected by air pollutants emitted from the lower floors. For wind approaching from the opening of the building array (225°; Figure 5.13e) with a downstream emission source, neighbouring buildings and the central space of the array were the least affected. The middle block obstructed the airflow and created a small air stagnation zone between the left wing and l-middle walls, increasing the air pollution concentration relative to the other walls; however, as the vertical distance from the emissions source increased, the concentration of pollutants decreased to very low levels comparable to the surfaces of other buildings.

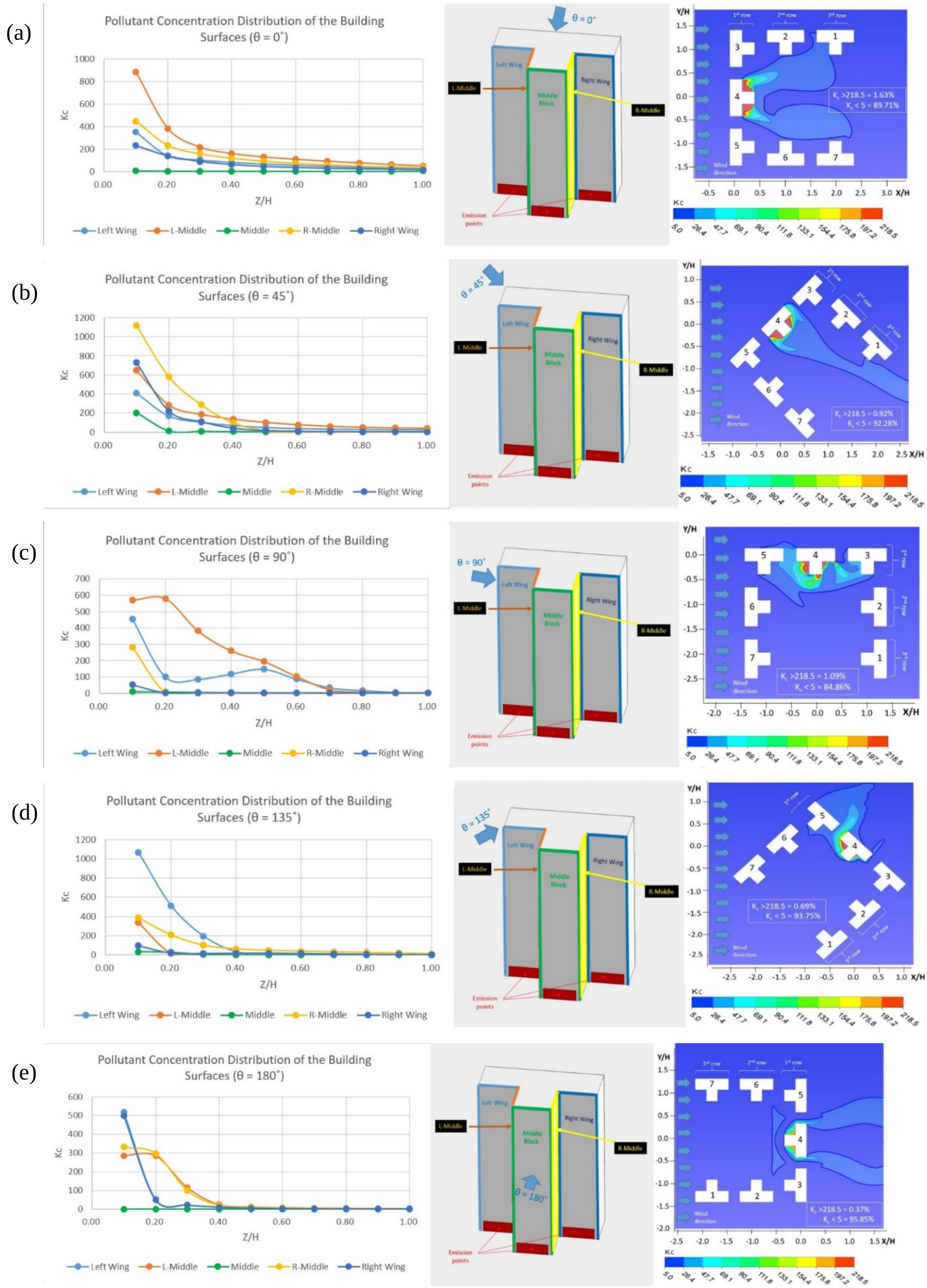

Figure 5.14 Distribution of pollutant concentrations on the left wing, l-middle, middle, r-middle, and

right wing building walls, under incident wind angles of: (a) 0°, (b) 45°, (c) 90°, (d) 135°, and (e) 180° for the ‘U’-shaped building array

For wind directly approaching the ‘U’-shaped building arrays (0°; Figure 5.14a), the central space experienced the worst-case scenario emission concentrations; however, owing to the even and symmetrical distribution of air circulation, the concentration of air pollutants gradually decreased with building height. Under the oblique wind (45°; Figure 5.14b), the perturbation of turbulence created on the leeward walls of the source building (i.e., Block 4) caused varying degrees of pollutant concentrations on all surfaces along the leeward direction. The corresponding rapid air movement inside the central space gradually decreased the pollutant concentration (similar to the case displayed when the incident wind angle was 0°; Figure 5.14a). For wind approaching from the side (90°; 5.14c), pollutant concentrations generally dropped to relatively low levels (i.e., $K_c < 200$) when moving away from the emission source, reaching z = 0.4H; however, in the ‘U’-shaped building array, pollutant concentration on the l-middle wall decayed slightly with building height due perhaps to the blockage effect imposed by the upstream building (i.e., Block 5). Air stagnation enhanced pollutant accumulation (i.e., decreased dispersion), and accounted for the subtle increase in pollutant concentrations on the mid-level, left wing wall. For an opposing oblique wind angle (135°; Figure

5.14d) under the shade of Block 6, initial pollutant concentrations on the left wing were comparatively high. Similar to all other wall surfaces, the concentration decayed rather quickly to a very low level at a vertical height of ~z = 0.4*H*. The opposite wind angle (180°; Figure 5.14e) provided the most favourable conditions for pollutant dispersal in the wind direction on the leeward side of the building group.

5.3 Summary

Incident wind angles and the orientations of building arrays arranged in 'U' and 'L' shapes (common in Hong Kong) strongly affected the LWV zone development in the central space of the array, as well as the pollutant distribution at the pedestrian level within this central space, commonly used for amenities, recreational facilities, or other activities. Incident wind angles of 0°, 45°, 135°, 180°, and 225°, and 0°, 45°, 90°, 135°, and 180° were considered for 'L'- and U'-shaped building arrays, respectively.

In general, 'L'-shaped building arrays maintained slightly better LWV zone area ratios, and smaller areas of high pollutant concentration than 'U'-shaped arrays. The wider opening of the array enclosure in the 'L'-shaped array, and the blockage effect posed by the buildings located downstream in the 'U'-shaped building arrangement were likely the key contributing factors. The worst-case scenario for the proportion and distribution of the LWV, and resulting high pollutant concentration zones in the 'L'-

shaped building arrays was observed at an incident wind of 0°, which similarly produced the least favourable conditions for the central space of the ‘U’-shaped arrays. Oblique wind directions favour the distribution of airflow and pollutants, but depend on the opening of the semi-enclosed building array structure, and the direction of the pollution source. Therefore, architects and building engineers should consider the benefit of ‘L’-shaped arrays instead of the ‘U’-shaped arrays, and avoid certain building orientations to enhance the natural wind comfort experienced by pedestrians enjoying recreational facilities in the central space of the buildings, ultimately achieving better ventilation and air quality.

CHAPTER 6 Conclusions and Future Recommendations

6.1 Conclusion and main contributions

This thesis studied the impacts of gaseous emissions from a research building on air quality in a small urban setting, and evaluated the effects of incident wind directions, individual building configurations, and array arrangements on wind flow and air contaminant-distribution in the building wakes and central space of these building groups. The key observations and findings from the thesis are highlighted below:

- Air monitoring and tracer gas studies are tedious, cost-intensive, and labour-intensive. From the experience of the emissions study in Chapter 3, it is not feasible to test all locations and cases year-round, and snapshot different wind conditions. Further, not all sampling locations are accessible for measurement.

- From the emissions study (Chapter 3), it was found that the air pollutant emitted from the source building has been heavily diluted in the atmosphere before reaching the recipient buildings. Due to the formation of air turbulence in the leeward and central space of the buildings, the accumulation of air contaminants within this central space and its corresponding concentration were even higher than the those observed for the windward sampling locations. CFD simulations in

Chapters 4 and 5 also displayed similar findings in terms of pollutant distribution along the leeward wall and central space of building groups. In Chapter 4, it was found that the air recirculation and current backflow occurred in the lower and mid-levels of the leeward wall, where the negative pressure in these areas would be higher than the upper floors. It would thus be beneficial for units adopting natural ventilation to place windows along the leeward wall and in the lower and middle floors of the building; however, in case of pollutant sources located upstream, fresh air would carry air pollutants, and cause of leak of air contaminants into the indoor areas.

- The CFD simulations mentioned in Chapter 5 resembled the actual situation of Residence W in the emissions study of Chapter 3, where buildings are arranged in 'U'- and 'L'-shaped arrays. It provided insight on the pollutant concentration distribution in the central space of these building groups under different incident wind angles.

- Owing to limitations of in situ air monitoring and tracer gas studies, the airflow patterns around the buildings revealed in Chapter 4 and 5, along with the conditions that are favourable for enhancing outdoor ventilation and dispersion of air contaminants, can inform the design of building engineers and architects within a small, urban setting, and guide how best to optimize the benefits of natural ventilation.

The main contributions of the thesis are summarized as follows:

(a) The RNG k-ε model is a suitable and economical choice for numerical simulations, and together with air monitoring and tracer gas assessment data, can constitute a comprehensive approach for assessing the impact of stack emissions in a small urban setting.

(b) It was revealed that when the wind approached a lateral (90°) direction, the downwind length and maximum bilateral width of the low-wind velocity zone in the wake of a “T”-shaped building decreased significantly. When the incident wind was oblique (45°), the low-wind-velocity LWV length and width in the wake of a “+”-shaped building also decreased remarkably.

(c) The air pressure on the leeward walls of the “T”- and “+”-shaped buildings gradually decreased with building height. The resulting low-wind conditions on the upper floors of the buildings reduced the fresh air intake via natural ventilation of the leeward units. This was particularly apparent in the case of direct approaching wind.

(d) The ‘L’-shaped array performed better than the ‘U’-shaped array by forming a smaller LWV zone in the central space of the buildings. The ‘L’-shaped array performed best at an incident wind angle of 225°. A 90° incident angle produced the largest LWV zone for the ‘U’-shaped array. Although the ‘L’-shaped array generally distributed pollutants better, the ‘U’-shaped array with a 180° wind angle had a smaller high pollutant concentration area than the ‘L’-shaped array with a wind angle of 225°. The worst vertical dispersion corresponded to a 135° wind angle for the ‘L’-shaped array, which recorded the highest contaminant concentrations at the mid-level of the building.

(e) The appropriate selection of configurations, building arrays, and their orientations allows for the most effective use of wind to enhance natural ventilation in indoor and urban environments.

6.2 Gaseous emissions in a small urban setting

The gaseous emission from stacks connected to the fume hoods of chemical laboratories may have detrimental health effects on people working or living nearby. In a densely populated city such as Hong Kong, exposure to various air pollutants of anthropogenic sources is inevitable and contribute to the overall pollution load, although their origins are difficult to identify. This thesis summarized the results of an emissions study in a comprehensive approach to identify the effects of gaseous emissions from a laboratory building situated within a short distance from a residential building group in Kowloon City, Hong Kong. Among the 15 selected chemicals for analysis, only NO_2, acetonitrile, and TVOC exceeded the pre-established exposure thresholds. Upon examination of the analysis results, wind direction, and baseline monitoring activities, it was concluded that pre-existing environmental sources, such as renovation work in close proximity to air sampling locations, may have contributed to the exceeding results observed; however, the stack emissions from the ZS Building may also be partially accountable, particularly for the elevated results recorded at IT and mid-level locations in Residence W. Both the tracer gas study and CFD modelling indicated that the gaseous emissions were heavily diluted above the roof of the ZS Building.

The flow simulation of the RNG k-ε model demonstrated that the recirculation vortices formed in the wake region or leeward side of the building further reduced airflow velocities, subsequently enhancing the accumulation of pollutants, and affecting the urban area air quality. Though IT is located upstream of the emissions source, these simulated results revealed that the concentration transport along the upwind direction by advection and recirculation flow could still impact its location. This can also explain the observed variability of TVOC and acetonitrile in IT, regardless of wind direction. Accordingly, the installation of fresh air intakes on the leeward wall of IT should be avoided due to the potential for higher pollutant concentrations caused by the reverse flow in the building-wake region.

The validation process, however, showed that the RNG k-ε model only achieved relatively accurate predictions of pollutant dispersion in an actual urban environment when compared with the RLZ k-ε model. Despite the RNG k-ε model yielding statistically acceptable results with respect to all tracer gas sampling data (FB, -0.13–0.4; FAC2, 0.7–1.1), when challenged by the MG, it showed a mild statistical deviation (MG = 1.5), and tended to over-estimate the extent of rooftop pollutant dilution.

Although the RANS simulation approaches are an economical choice for CFD, the results from the present study showed that they may not be sufficient for achieving statistically sound results with respect to the field measurement data collected across an actual urban environment. Careful interpretation of data generated by the RANS approaches is thus needed moving forward, and these analyses should be used and read in conjunction with air monitoring and tracer gas assessment data for a more comprehensive approach when assessing the impacts of stack emissions within an urban setting.

6.3 Wind direction and building configuration effects on airflow and pressure distribution within building wakes and along leeward walls

It was determined that the incident wind angle and building orientations of "T"- and "+"-shaped buildings, configurations common to Hong Kong, had a substantial effect on the LWV zone development within the wakes, in addition to the pressure distributions along the leeward walls of buildings, when compared to the normal, "-"-shaped building configuration. For "T"-shaped buildings, five incident angles were considered: direct approaching (0°), oblique approaching (45°), lateral (90°), oblique opposing (135°), and opposing (180°); whereas for "+"-shaped buildings, only two were necessary: direct (0°) and oblique (45°), as all other angles were equivalent to one of these two.

To recap, incident wind directions and building configurations significantly affected the ventilation of an urban setting, and resulting air qualities in both outdoor and indoor environments. First, when the wind was blowing from an oblique (45°) angle, or onto a lateral side (90°) of either the "T"- or "+"-shaped building, the resulting horizontal distance between the building and the LWV zone in its wake was the smallest, and the air velocity in the building wake the highest. Second, the vortex formed near the protruding structure in the back section on the leeward side of the building could help shorten the horizontal spread of the zero- and LWV zone in the building wake. The resulting high-velocity flow on the leeward side penetrated deeper into the street canyon, and facilitated the dispersion of air pollutants in the building wake, ultimately providing more favourable wind conditions for pedestrians to engage outdoor activities within the building wake region. Third, natural ventilation via windows due to pressure differences on the leeward wall of the building can also help improve the indoor environment; however, the vertical air movement in the upper part of the leeward wall was dominant under all incident wind directions, thus diminishing the benefits of natural, leeward window ventilation for the upper-level units. The ventilation force on the leeward wall peaked when the lateral wind was dominant, while the *Cp* values of the leeward walls for all other wind directions were noticeably lower. The direct approaching (0°) wind demonstrated the worst-case scenario in terms of low wake airflow, and poor air infiltration along the leeward wall, particularly on the upper floors.

6.4 Wind direction and building arrangement effects on flow and gaseous contaminant distribution within the central space of building arrays

Incident wind angles and the orientations of building arrays arranged in ‘U’ and ‘L’ shapes (common in Hong Kong) strongly affected the LWV zone development in the central space of the array, and thus the pollutant distribution at the pedestrian level in this location, commonly used for residential amenities or recreational facilities. Incident wind angles of 0°, 45°, 135°, 180°, and 225°, and 0°, 45°, 90°, 135°, and 180° were considered for ‘L’- and U’-shaped building arrays, respectively.

In summary, incident wind direction and different building arrays significantly affected ventilation and pollutant dispersion within the central space of building arrangements, and along building surfaces. In general, ‘L’-shaped building arrays had slightly better LWV zone area ratios, and smaller areas of high pollutant concentrations compared to ‘U’-shaped arrays. The wider enclosure opening in the ‘L’-shaped array, in addition to the blockage effects imposed by the buildings located downstream in the ‘U’-shaped arrangement, were likely important contributing factors. The worst-case scenario for the proportion and distribution of the LWV and high pollutant concentration zones in the ‘L’-shaped building arrays was recorded with an incident wind angle of 0°, which similarly produced the least favourable conditions for the central space of the ‘U’-shaped array as well. Oblique wind directions favoured the distribution of airflow and pollutants, but were dependent on the opening of the semi-enclosed building array structures, as well as the pollution source direction. Therefore, architects and building engineers should preferably consider the benefits of ‘L’-shaped arrays, and avoid certain building orientations to optimize the wind comfort of pedestrians enjoying recreational facilities in the central space of the buildings, resulting in better ventilation and air quality.

6.5 Future directions

Several limited or incomplete aspects are present the research of this thesis, each of which should be addressed in future research:

(a) With respect to the insufficiency of time-averaged simulation approaces (e.g., RANS used in the present study), other transient models, such as large eddy simulation (LES) and detached eddy simulation (DES), could be employed to yield more accurate results and control numerical error by using the mean flow over a sufficiently long sampling period (Liu et al., 2019c; Zahid Iqbal and Chan, 2016); however, much higher computational and financial costs would be incurred.

(b) Two common building configurations were assessed, and simulations of simple, isolated buildings can help clarify the role of the individual building configurations and wind directions on the distribution of airflow and ventilation conditions. Such analyses are commonly used to test model accuracy along with experimental wind tunnel test results, and can help provide inlet boundary conditions under a homogenous atmospheric boundary layer; however, only changes to the flow fields within the building wakes and on the leeward sides of the buildings were studied. Other buildings or structures in close proximity will also significantly impact the ventilation flowing through the building. As such, the impacts of surrounding buildings or other structures that are a part of the urban environment on building ventilation and outside pollutant dispersion should be assessed in future research. Simulations should be performed to more completely resolve the effects of different building arrays and configurations on the flow fields, as well as the interference effects of surrounding environments on the pressure distributions along building walls.

(c) Two of the primary goals of the present study were to evaluate the impacts of different incident wind directions and building orientations on wind velocity and air pollutant accumulation at the pedestrian level within the central space of "L"- and "U"-shaped building arrays. Accordingly, only two, albeit common, building arrays were assessed; thus, the distribution of airflow and dispersion of pollutants in other less common or irregular building arrangements, or within complex urban settings containing multiple building shapes and arrays, requires further study.

(d) To meet the objectives of the present study, isothermal conditions were assumed and investigated as a reference to evaluate the differences of wind environments at the pedestrian level within the central space, and dispersion of air contaminants around buildings. The buoyancy effect was not adequately considered in this study, but is an essential driving force for natural ventilation, especially at low wind speeds inside the building arrays and within the street canyon. Niu and Tung (2008) suggested that the influence of thermal forces are only overwhelmed by turbulence at wind speeds < 0.9 $m \cdot s^{-1}$. When considering the temperature gradient between indoor and outdoor air, the driving forces could be further complicated, leading to different ventilation and pollutant dispersion results. Accordingly, some authors have suggested considering the wall thermal boundary conditions under relatively low wind speeds to achieve the correct airflow patterns, especially when examining pollutant and heat removal (Chen et al., 2020). A further important criterion for simulating isothermal flow and dispersion fields is the Reynolds number (Re) independence. According to Re-independence theory, when the Re exceeds a critical value, the flow field enters an Re-independent regime where flow characteristics no longer change with further increasing Re (Snyder, 1981). Therefore, the characteristics of the ventilation performance and pollutant dispersion in the urban environment under low wind conditions with buoyancy effects and convective heat transfer likely requires further study. In addition, the use of other techniques such as reduced wind tunnel smoke flow visualizations and particle image velocimetry experiments to study the building configurations and arrays in low Reynolds numbers range could be considered in further studies.

(e) Apart from air quality issues, many other environmental conditions, such as daylight direction and environmental noise source could be considered for further study, as well as in the planning and design of the building and urban layouts.

REFERENCES

Abbott, S.M., Elder, J.B., Španěl, P., Smith, D., 2003. Quantification of acetonitrile in exhaled breath and urinary headspace using selected ion flow tube mass spectrometry. International Journal of Mass Spectrometry 228, 655–665.

Aflaki, A., Mahyuddin, N., Al-Cheikh Mahmoud, Z., Baharum, M.R., 2015. A review on natural ventilation applications through building façade components and ventilation openings in tropical climates. Energy and Buildings 101, 153–162.

Ai, Z.T., Mak, C.M., 2013. CFD simulation of flow and dispersion around an isolated building: Effect of inhomogeneous ABL and near-wall treatment. Atmospheric Environment 77, 568–578.

Ai, Z.T., Mak, C.M., 2014a. Modeling of coupled urban wind flow and indoor air flow on a high-density near-wall mesh: Sensitivity analyses and case study for single-sided ventilation. Environmental Modelling and Software 60, 57–68.

Ai, Z.T., Mak, C.M., 2014b. A study of interunit dispersion around multistory buildings with single-sided ventilation under different wind directions. Atmospheric Environment 88, 1–13.

Ai, Z.T., Mak, C.M., 2015. Large-eddy simulation of flow and dispersion around an isolated building: Analysis of influencing factors. Computers & Fluids 118, 89–100.

Ai, Z.T., Mak, C.M., 2016. Large eddy simulation of wind-induced interunit dispersion around multistory buildings. Indoor Air 26, 259–273.

Ai, Z.T., Mak, C.M., 2017. CFD simulation of flow in a long street canyon under a perpendicular wind direction: Evaluation of three computational settings. Building and Environment 114, 293–306.

Ai, Z.T., Mak, C.M., Lee, H.C., 2016. Roadside air quality and implications for control measures: A case study of Hong Kong. Atmospheric Environment 137, 6–16.

An, K., Fung, J.C.H., Yim, S.H.L., 2013. Sensitivity of inflow boundary conditions on downstream wind and turbulence profiles through building obstacles using a CFD approach. Journal of Wind Engineering and Industrial Aerodynamics 115, 137–149.

Ansys Fluent *v.*14.5, 2012. Ansys, Inc., Canonsburg, PA, USA.

ATSDR—Agency for Toxic Substances and Diseases Registry, 1994. Toxicological Profile for Acetone.

ATSDR—Agency for Toxic Substances and Diseases Registry, 1997. Toxicological Profile for Chloroform.

ATSDR—Agency for Toxic Substances and Diseases Registry, 2006. Toxicological Profile for 1,1,1-Trichloroethane, in: Service, U.S.D.o.H.a.H.S.P.H. (Ed.), Atlanta, GA.

ATSDR—Agency for Toxic Substances and Diseases Registry, 2017. Toxicological Profile for Toluene.

Bady, M., Kato, S., Huang, H., 2008. Towards the application of indoor ventilation efficiency indices to evaluate the air quality of urban areas. Building and Environment 43, 1991–2004.

Ballinger, M.Y., Larson, T.V., 2014. Source apportionment of stack emissions from research and development facilities using positive matrix factorization. Atmospheric Environment 98, 59–65.

Blocken, B., 2015. Computational fluid dynamics for urban physics: Importance, scales, possibilities, limitations and ten tips and tricks towards accurate and reliable simulations. Building and Environment 91, 219–245.

Blocken, B., Janssen, W.D., van Hooff, T., 2012. CFD simulation for pedestrian wind comfort and wind safety in urban areas: General decision framework and case study for the Eindhoven University campus. Environmental Modelling & Software 30, 15–34.

Blocken, B., Stathopoulos, T., Carmeliet, J., 2007. CFD simulation of the atmospheric boundary layer: Wall function problems. Atmospheric Environment 41, 238–252.

Blocken, B., Stathopoulos, T., Saathoff, P., Wang, X., 2008. Numerical evaluation of pollutant dispersion in the built environment: Comparisons between models and experiments. Journal of Wind Engineering & Industrial Aerodynamics 96, 1817–1831.

Borrego, C., Martins, H., Tchepel, O., Salmim, L., Monteiro, A., Miranda, A.I., 2006. How urban structure can affect city sustainability from an air quality perspective. Environmental Modelling and Software 21, 461–467.

Bradshaw, P., 1969. The analogy between streamline curvature and buoyancy in turbulent shear flow. Journal of Fluid Mechanics 36, 177–191.

Burman, J., Jonsson, L., 2015. Issues when linking computational fluid dynamics for urban modeling to toxic load models: The need for further research. Atmospheric Environment 104, 112–124.

Canepa, E., 2004. An overview about the study of downwash effects on dispersion of airborne pollutants. Environmental Modelling and Software 19, 1077–1087.

Cao, S.-J., Yu, C.W., Luo, X., 2020. Heating, ventilating and air conditioning system and environmental control for wellbeing. Indoor and Built Environment 29, 1

191–1194.

Celik, I., Ghia, U., Roache, P., Christopher, 2008. Procedure for estimation and reporting of uncertainty due to discretization in CFD applications. Journal of Fluids Engineering-Transactions of the ASME 130.

Census and Statistics Department of Hong Kong, 2018. Hong Kong Statistics. Population.

Chan, T.L., Dong, G., Leung, C.W., Cheung, C.S., Hung, W.T., 2002. Validation of a two-dimensional pollutant dispersion model in an isolated street canyon. Atmospheric Environment 36, 861–872.

Chang, J.C., Hanna, S.R., 2004. Air quality model performance evaluation. Meteorology and Atmospheric Physics 87, 167–196.

Chen, G.X., Rong, L., Zhang, G.Q., 2020. Comparison of urban airflow between solar-induced thermal wall and uniform wall temperature boundary conditions by coupling CitySim and CFD. Building and Environment 172, 106732.

Chen, K.W., Norford, L., 2017. Evaluating urban forms for comparison studies in the massing design stage. Sustainability 9, 987.

Cheng, J., Qi, D., Katal, A., Wang, L., Stathopoulos, T., 2018. Evaluating wind-driven natural ventilation potential for early building design. Journal of Wind Engineering and Industrial Aerodynamics 182, 160–169.

Cheng, V., Ng, E., 2006. Thermal comfort in urban open spaces for Hong Kong. Architectural Science Review 49, 236–242.

Chew, L.W., Norford, L.K., 2018. Pedestrian-level wind speed enhancement in urban street canyons with void decks. Building and Environment 146, 64–76.

Chowdhury, M.G., Goossens, D., Goverde, H., Catthoor, F., 2018. Experimentally validated CFD simulations predicting wind effects on photovoltaic modules mounted on inclined surfaces. Sustainable Energy Technologies and Assessments 30, 201–208.

Cremades, L., 2000. Estimating the background air concentration excluding the contribution of an individual source. Environmental Modeling & Assessment 5, 119–124.

Dadioti, R., Rees, S., 2017. Performance of detached eddy simulation applied to analysis of a university campus wind environment. Energy Procedia 134, 366–375.

Dai, Y., Mak, C.M., Ai, Z., Hang, J., 2018a. Evaluation of computational and physical parameters influencing CFD simulations of pollutant dispersion in building arrays. Building and Environment 137, 90–107.

Dai, Y., Mak, C.M., Ai, Z.T., Hang, J., 2018b. Evaluation of computational and physical parameters influencing CFD simulations of pollutant dispersion in building arrays. Building and Environment 137, 90–107.

Dai, Y.W., Mak, C.M., Ai, Z.T., 2017. Computational fluid dynamics simulation of wind-driven inter-unit dispersion around multi-storey buildings: Upstream building effect. Indoor and Built Environment 28, 217–234.

Deng, X., Tan, Z., 2019. Numerical analysis of local thermal comfort in a plan office under natural ventilation. Indoor and Built Environment 29, 972–986.

Dervos, C.T., Vassiliou, P., 2000. Sulfur hexafluoride (SF6): Global environmental effects and toxic byproduct formation. Journal of the Air & Waste Management Association 50, 137.

Du, Y., Mak, C.M., 2018. Improving pedestrian level low wind velocity environment in high-density cities: A general framework and case study. Sustainable Cities and Society 42, 314–324.

Du, Y., Mak, C.M., Liu, J., Xia, Q., Niu, J., Kwok, K.C.S., 2017a. Effects of lift-up design on pedestrian level wind comfort in different building configurations under three wind directions. Building and Environment 117, 84–99.

Du, Y.X., Mak, C.M., Kwok, K., Tse, K.-T., Lee, T.-C., Ai, Z.T., Liu, J.L., Niu, J.L., 2017b. New criteria for assessing low wind environment at pedestrian level in Hong Kong. Building and Environment 123, 23–36.

Du, Y.X., Mak, C.M., Li, Y.T., 2019. A multi-stage optimization of pedestrian level wind environment and thermal comfort with lift-up design in ideal urban canyons. Sustainable Cities and Society 46, 101424.

Efthimiou, G.C., Andronopoulos, S., Bartzis, J.G., 2018. Prediction of dosage-based parameters from the puff dispersion of airborne materials in urban environments using the CFD-RANS methodology. Meteorology and Atmospheric Physics 130, 107–124.

Etheridge, D., 2015. A perspective on fifty years of natural ventilation research. Building and Environment 91, 51–60.

Fang, Z.S., Feng, X.W., Liu, J.L., Lin, Z., Mak, C.M., Niu, J.L., Tse, K.T., Xu, X.N., 2019. Investigation into the differences among several outdoor thermal comfort indices against field survey in subtropics. Sustainable Cities and Society 44, 676–690.

Franke, J., Hellsten, A., Schlünzen, H., Carissimo, B., 2007. Cost Action 732: Best Practice Guideline for the CFD Simulation of Flow in the Urban Environment, in: Quality Assurance and Impovement of Microscale Meteorological Models, Meteorological

Institute, Brussels.

Gao, C.F., Lee, W.L., 2011. Evaluating the influence of openings configuration on natural ventilation performance of residential units in Hong Kong. Building and Environment 46, 961–969.

Gao, N.P., Niu, J.L., Perino, M., Heiselberg, P., 2008. The airborne transmission of infection between flats in high-rise residential buildings: Tracer gas simulation. Building and Environment 43, 1805–1817.

Garbrecht, O., 2017. Large Eddy Simulation of Three-dimensional Mixed Convection on a Vertical Plate, Faculty of Mechanical Engineering. RWTH Aachen University.

Gorlé, C., van Beeck, J., Rambaud, P., 2010. Dispersion in the wake of a rectangular building: Validation of two Reynolds-averaged Navier–Stokes modelling approaches. Boundary-Layer Meteorology 137, 115–133.

Gousseau, P., Blocken, B., Stathopoulos, T., van Heijst, G.J.F., 2011. CFD simulation of near-field pollutant dispersion on a high-resolution grid: A case study by LES and RANS for a building group in downtown Montreal. Atmospheric Environment 45, 428–438.

Hang, J., Li, Y., Sandberg, M., 2011. Experimental and numerical studies of flows through and within high-rise building arrays and their link to ventilation strategy. Journal of Wind

Engineering and Industrial Aerodynamics 99, 1036–1055.

Hang, J., Sandberg, M., Li, Y., 2009. Age of air and air exchange efficiency in idealized city models. Building and Environment 44, 1714–1723.

HKEPD—Hong Kong Environmental Protection Department, 2015. Air Quality Objectives.

HKEPD—Hong Kong Environmental Protection Department, n.d. Annual AQI Trend.

Hong Kong Observatory, 2017. Summary of Meteorological and Tidal Observations in Hong Kong 2016.

Huang, Y.D., Hu, X.N., Zeng, N.B., 2009. Impact of wedge-shaped roofs on airflow and pollutant dispersion inside urban street canyons. Building and Environment 44, 2335–2347.

Indoor Air Quality Management Group, 2003. A Guide on Indoor Air Quality Certification Scheme for Offices and Public Places, in: Department, H.K.E.P. (Ed.). The Government of Hong Kong Special Administrative Region, Hong Kong.

Jiang, Y., Alexander, D., Jenkins, H., Arthur, R., Chen, Q.Y., 2003. Natural ventilation in buildings: Measurement in a wind tunnel and numerical simulation with large-eddy simulation. Journal of Wind Engineering and Industrial Aerodynamics 91, 331–353.

Jordan, A., Hansel, A., Holzinger, R., Lindinger, W., 1995. Acetonitrile and benzene in the breath of smokers and non-smokers investigated by proton transfer reaction mass spectrometry (PTR-MS). International Journal of Mass Spectrometry and Ion Processes 148, L1–L3.

King, M.-F., Khan, A., Delbosc, N., Gough, H.L., Halios, C., Barlow, J.F., Noakes, C.J., 2017. Modelling urban airflow and natural ventilation using a GPU-based lattice-Boltzmann method. Building and Environment 125, 273–284.

Kobza, J., Geremek, M., Dul, L., 2018. Characteristics of air quality and sources affecting high levels of PM_{10} and $PM_{2.5}$ in Poland, Upper Silesia urban area. Environmental Monitoring and Assessment 190, 515.

Koutsourakis, N., Bartzis, J.G., Markatos, N.C., 2012. Evaluation of Reynolds stress, k-ε and RNG k-ε turbulence models in street canyon flows using various experimental datasets. Environmental Fluid Mechanics 12, 379–403.

Kumar, A., Luo, J., Bennett, G.F., 1993. Statistical evaluation of lower flammability distance (LFD) using four hazardous release models. Process Safety Progress 12, 1–11.

Lateb, M., Masson, C., Stathopoulos, T., Bedard, C., 2013. Comparison of various types of k-epsilon models for pollutant emissions around a two-building configuration. Journal of Wind Engineering and Industrial Aerodynamics 115, 9–21.

Lateb, M., Masson, C., Stathopoulos, T., Bédard, C., 2011. Effect of stack height and exhaust velocity on pollutant dispersion in the wake of a building. Atmospheric Environment 45.

Lee, K.Y., Mak, C.M., 2019. A comprehensive approach to study stack emissions from a research building in a small urban setting. Sustainable Cities and Society 51, 101710.

Leitl, B., Schatzmann, M., 1998. Compilation of Experimental Data for Validation Purposes. Meteorology Institute, Hamburg University, Hamburg.

Li, X.-X., Liu, C.-H., Leung, D.Y.C., Lam, K.M., 2006. Recent progress in CFD modelling of wind field and pollutant transport in street canyons. Atmospheric Environment 40, 5640–5658.

Li, Y., Stathopoulos, T., 1997. Numerical evaluation of wind-induced dispersion of pollutants around a building. Journal of Wind Engineering and Industrial Aerodynamics 67–68, 757–766.

Liu, J., Heidarinejad, M., Pitchurov, G., Zhang, L., Srebric, J., 2018. An extensive comparison of modified zero-equation, standard k-ε, and LES models in predicting urban airflow. Sustainable Cities and Society 40, 28–43.

Liu, J., Niu, J., Du, Y., Mak, C.M., Zhang, Y., 2019a. LES for pedestrian level wind around an idealized building array—Assessment of sensitivity to influencing parameters. Sustainable Cities and Society 44, 406–415.

Liu, J., Zhang, X., Niu, J., Tse, K.T., 2019b. Pedestrian-level wind and gust around buildings with a ‘lift-up’ design: Assessment of influence from surrounding buildings by adopting LES. Building Simulation 12, 1107–1118.

Liu, J.L., Niu, J.L., 2016. CFD simulation of the wind environment around an isolated high-rise building: An evaluation of SRANS, LES and DES models. Building and Environment 96, 91–106.

Liu, J.L., Niu, J.L., Du, Y.X., Mak, C.M., Zhang, Y.F., 2019c. LES for pedestrian level wind around an idealized building array—Assessment of sensitivity to influencing parameters. Sustainable Cities and Society 44, 406–415.

Lübcke, H., Schmidt, S., Rung, T., Thiele, F., 2001. Comparison of LES and RANS in bluff-body flows. Journal of Wind Engineering & Industrial Aerodynamics 89, 1471–1485.

Man, X., Lu, Y., Li, G., Wang, Y., Liu, J., 2019. A study on the stack effect of a super high-rise residential building in a severe cold region in China. Indoor and Built Environment 29, 255–269.

Meroney, R., 2004. Wind tunnel and numerical simulation of pollution dispersion: A hybrid approach. Paper for Invited Lecture at the Croucher Advanced Study Institute, Hong Kong University of Science and Technology, 6–10.

Mirzaei, P.A., Rad, M., 2013. Toward design and fabrication of wind-driven vehicles: Procedure to optimize the threshold of driving forces. Applied Mathematical Modelling 37, 50–61.

Mittal, H., Sharma, A., Gairola, A., 2019. Numerical simulation of pedestrian level wind flow around buildings: Effect of corner modification and orientation. Journal of Building Engineering 22, 314–326.

Mochida, A., Lun, I.Y.F., 2008. Prediction of wind environment and thermal comfort at pedestrian level in urban area. Journal of Wind Engineering & Industrial Aerodynamics 96, 1498–1527.

Montazeri, H., Blocken, B., 2013. CFD simulation of wind-induced pressure coefficients on buildings with and without balconies: Validation and sensitivity analysis. Building and Environment 60, 137–149.

Mu, D., Gao, N., Zhu, T., 2016. Wind tunnel tests of inter-flat pollutant transmission characteristics in a rectangular multi-story residential building, part A: Effect of wind direction. Building and Environment 108, 159–170.

Nathanson, T., 1995. Indoor Air Quality in Office Buildings: A Technical Guide, in: Canada, H. (Ed.). Health Canada, Minister of Supply and Services, Canada.

Ng, E., 2009. Policies and technical guidelines for urban planning of high-density cities – air ventilation assessment (AVA) of Hong Kong. Building and Environment 44, 1478–1488.

Ng, E., Tam, I., Ng, A., Givoni, B., Katzschner, L., Kwok, K., Cheng, V., 2005. Feasibility study for establishment of air ventilation assessment system–final report. Hong Kong: Department of Architecture, Chinese University of Hong Kong 16.

Niu, J., Liu, J., Lee, T.-C., Lin, Z., Mak, C., Tse, K.-T., Tang, B.-S., Kwok, K.C.S., 2015. A new method to assess spatial variations of outdoor thermal comfort: Onsite monitoring results and implications for precinct planning. Building and Environment 91, 263–270.

Niu, J.L., Tung, T.C.W., 2008. On-site quantification of re-entry ratio of ventilation exhausts in multi-family residential buildings and implications. Indoor Air 18, 12–26.

OEHHA—California Office of Environmental Health Hazard Assessment, 2016. OEHHA Acute, 8-hour and Chronic Reference Exposure Level (REL) Summary.

Omrani, S., Garcia-Hansen, V., Capra, B., Drogemuller, R., 2017. Natural ventilation in multi-storey buildings: Design process and review of evaluation tools. Building and Environment 116, 182–194.

Padilla-Marcos, M.Á., Meiss, A., Feijó-Muñoz, J., 2017. Proposal for a simplified CFD procedure for obtaining patterns of the age of air in outdoor spaces for the natural ventilation of buildings. Energies 10, 1252.

Park, J., Lee, L., Byun, H., Ham, S., Lee, I., Park, J., Rhie, K., Lee, Y., Yeom, J., Tsai, P., Yoon, C., 2014. A study of the volatile organic compound emissions at the stacks of laboratory fume hoods in a university campus. Journal of Cleaner Production 66, 10–18.

Peng, Y., Buccolieri, R., Gao, Z., Ding, W., 2020. Indices employed for the assessment of “urban outdoor ventilation” - A review. Atmospheric Environment 223, 117211.

Puliafito, E., Guevara, M., Puliafito, C., 2003. Characterization of urban air quality using GIS as a management system. Environmental Pollution 122, 105–117.

Richards, P.J., Hoxey, R.P., 1993. Appropriate boundary conditions for computational wind engineering models using the k-ϵ turbulence model. Journal of Wind Engineering and Industrial Aerodynamics 46–47, 145–153.

Sakiyama, N.R.M., Mazzaferro, L., Carlo, J.C., Bejat, T., Garrecht, H., 2021. Natural ventilation potential from weather analyses and building simulation. Energy and Buildings 231, 110596.

Shirzadi, M., Mirzaei, P.A., Tominaga, Y., 2020. RANS model calibration using stochastic optimization for accuracy improvement of urban airflow CFD modeling. Journal of Building Engineering 32, 101756.

Shirzadi, M., Naghashzadegan, M., A. Mirzaei, P., 2018. Improving the CFD modelling of cross-ventilation in highly-packed urban areas. Sustainable Cities and Society 37, 451–465.

Snyder, W.H., 1981. Guideline for fluid modeling of atmospheric diffusion. Fluid modeling report no. 10, in: US EPA. (Ed.), Research Triangle Park, NC (USA). Office of Air Quality Standards, Environmental Sciences Research Lab.

Tewari, M., Kusaka, H., Chen, F., Coirier, W.J., Kim, S., Wyszogrodzki, A.A., Warner, T.T., 2010. Impact of coupling a microscale computational fluid dynamics model with a mesoscale model on urban scale contaminant transport and dispersion. Atmospheric Research 96, 656–664.

Tien, P.W., Calautit, J.K., 2019. Numerical analysis of the wind and thermal comfort in courtyards "skycourts" in high rise buildings. Journal of Building Engineering 24, 100735.

Tominaga, Y., Mochida, A., Yoshie, R., Kataoka, H., Nozu, T., Yoshikawa, M., Shirasawa, T., 2008. AIJ guidelines for practical applications of CFD to pedestrian wind environment around buildings. Journal of Wind Engineering and Industrial Aerodynamics 96, 1749–1761.

Tominaga, Y., Stathopoulos, T., 2007. Turbulent Schmidt numbers for CFD analysis with various types of flowfield. Atmospheric Environment 41, 8091–8099.

Tominaga, Y., Stathopoulos, T., 2009. Numerical simulation of dispersion around an isolated cubic building: Comparison of various types of k–ε models. Atmospheric Environment 43, 3200–3210.

Tominaga, Y., Stathopoulos, T., 2013. CFD simulation of near-field pollutant dispersion in the urban environment: A review of current modeling techniques. Atmospheric Environment 79, 716–730.

Tsai, M.Y., Chen, K.S., 2004. Measurements and three-dimensional modeling of air pollutant dispersion in an Urban Street Canyon. Atmospheric Environment 38, 5911–5924.

US EPA—Environmental Protection Agency- Integrated Risk Information System (IRIS), 2013. Chemical Assessment Summary. Methanol; CASRN 67-56-1.

US EPA—Environmental Protection Agency- Integrated Risk Information System (IRIS), 1995. Chemical Assessment Summary. Hydrogen chloride; CASRN 7647-01-0.

US EPA—Environmental Protection Agency- Integrated Risk Information System (IRIS), 2005. Chemical Assessment Summary. n-Hexane; CASRN 110-54-3.

US EPA—Environmental Protection Agency- Integrated Risk Information System (IRIS), 2012. Chemical Assessment Summary. Tetrahydrofuran; CASRN 109-99-9.

US EPA—Environmental Protection Agency- Integrated Risk Information System (IRIS), 1999. Chemical Assessment Summary. Acetonitrile. CASRN 75-05-8. U

US EPA—Environmental Protection Agency- Integrated Risk Information System (IRIS), 2005. Chemical Assessment Summary. Toluene; CASRN 108-88-3.

US EPA—Environmental Protection Agency- Integrated Risk Information System (IRIS), 2011. Chemical Assessment Summary. Dichloromethane. CASRN 75-09-2.

US EPA—Environmental Protection Agency, 2014. Acute Exposure Guideline Levels (AGEL) for Selected Airborne Chemicals Vol.16

van Hooff, T., Blocken, B., Tominaga, Y., 2017. On the accuracy of CFD simulations of cross-ventilation flows for a generic isolated building: Comparison of RANS, LES and experiments. Building and Environment 114, 148–165.

Wang, B., Malkawi, A., 2019. Design-based natural ventilation evaluation in early stage for high performance buildings. Sustainable Cities and Society 45, 25–37.

Wang, J.S., Chan, T.L., Cheung, C.S., Leung, C.W., Hung, W.T., 2006. Three-dimensional pollutant concentration dispersion of a vehicular exhaust plume in the real atmosphere. Atmospheric Environment 40, 484–497.

Wang, X., Sun, X., Yu, C.W.F., 2018. Building envelope with variable thermal performance: Opportunities and challenges. Indoor and Built Environment 27, 729–733.

Wieringa, J., 1992. Updating the Davenport roughness classification. Journal of Wind Engineering and Industrial Aerodynamics 41, 357–368.

WHO—World Health Organization, 2000. Air Quality Guidelines for Europe, 2 ed. World Health Organization Regional Office for Europe, Copenhagen.

Xia, Q., Niu, J.L., Liu, X.P., 2014. Dispersion of air pollutants around buildings: A review of past studies and their methodologies, London, England. Indoor and Built Environment 23, 201–224.

Yassin, M.F., 2013. A wind tunnel study on the effect of thermal stability on flow and dispersion of rooftop stack emissions in the near wake of a building. Atmospheric Environment 65, 89–100.

Yim, S.H.L., Fung, J.C.H., Lau, A.K.H., Kot, S.C., 2009. Air ventilation impacts of the "wall effect" resulting from the alignment of high-rise buildings. Atmospheric Environment 43, 4982–4994.

Yin, H., Liu, C., Zhang, L., Li, A., Ma, Z., 2019. Measurement and evaluation of indoor air quality in naturally ventilated residential buildings. Indoor and Built Environment 28, 1307–1323.

Yola, L., Siong, H.C., Djaja, K.K., 2021. Impact of Urban Configurations on Airflow: Tropical Context Study, in: Emamian, S.S., Adekunle, T.O., Nangkula, U., Awang, M. (Eds.), ICSDEMS 2019. Springer, Singapore, pp. 281–288.

Yu, H., Thé, J., 2017. Simulation of gaseous pollutant dispersion around an isolated building using the k–ω SST (shear stress transport) turbulence model. Journal of the Air and Waste Management Association 67, 517–536.

Yuan, C., Ng, E., Norford, L.K., 2014. Improving air quality in high-density cities by understanding the relationship between air pollutant dispersion and urban morphologies. Building and Environment 71, 245–258.

Zahid Iqbal, Q.M., Chan, A.L.S., 2016. Pedestrian level wind environment assessment around group of high-rise cross-shaped buildings: Effect of building shape, separation and orientation. Building and Environment 101, 45–63.

Zhao, D.-X., He, B.-J., 2017. Effects of architectural shapes on surface wind pressure distribution: Case studies of oval-shaped tall buildings. Journal of Building Engineering 12, 219–228.